Decoding, Modulating, and Imaging Sensorimotor Pathways in the Brain

by

Matthew S. Willsey

A dissertation submitted in partial fulfillment
of the requirements for the degree of
Doctor of Philosophy
(Biomedical Engineering)
in the University of Michigan
2020

Doctoral Committee:

Associate Professor Cynthia A. Chestek, Co-Chair
Associate Professor Parag G. Patil, Co-Chair
Assistant Professor Scott F. Lempka
Associate Professor William C. Stacey

Matthew S. Willsey

mwillsey@umich.edu

ORCID iD: 0000-0003-2093-7733

Dedication

This dissertation is dedicated to my wife, Kylene, and two daughters.

Acknowledgements

I am forever grateful to my research mentors, Parag Patil and Cynthia Chestek. They have both gone above and beyond in the time and effort they have invested in my learning and my career. With their help, I have become a better scientist and researcher. I have also been very fortunate to learn from other extremely talented researchers at the University of Michigan, and I want to personally thank George Mashour, Scott Lempka, William Stacey, and Oren Sagher. As a neurosurgery resident, I have been very fortunate to receive mentorship from the faculty in the neurosurgery department at the University of Michigan. I would like to give a special thanks to Emily Levin for her mentorship. I would also like to thank Cormac Maher, Aditya Pandey, Karin Muraszko, and Greg Thompson for their mentorship and support. I have also had many other mentors in my lifetime and, while not possible to list them all here, I deeply appreciate their guidance.

There are many in the Biomedical Engineering department that were so unbelievably helpful in supporting my graduate studies. Maria Steele, Zhen Xu, and Tim Bruns were especially helpful. In the neurosurgery department, I would like to thank our program director, Cormac Maher, for being supportive of my graduate studies in engineering, and without him, this would not have been possible. Susie Hines has also been extremely helpful in her support of my training and education. I appreciate the support from my co-residents, specifically: David Altshuler, Amy Bruzek, Siri Khalsa, and Yamaan Saadeh.

Any research effort is collaborative and would not be possible without the other student collaborators. I appreciate the help from the entire Patil and Chestek labs including: Sam Nason, Charles Lu, Matt Mender, Scott Ensel, Paras Patel, Jim Mossner, Karlo Malaga, and Chrono Nu.

My wife, Kylene, has been more supportive than I could have ever imagined. I am a better person with her in my life and am eternally thankful. My two daughters have been an infinite source of joy and helped me get through some of the toughest times. I appreciate my parents for their love and support and for shaping me into the person I am today. I have been very fortunate to have relationships with my grandparents who have also helped mold me. Finally, I appreciate all my friends for their companionship and support through the years.

Table of Contents

Dedication ..... **ii**

Acknowledgements ..... **iii**

List of Figures ..... **ix**

List of Equations ..... **x**

Abstract ..... **xi**

Chapter 1. Introduction **1**

1.1 Motor Paralysis 1

1.2 Cortical Interfaces to Restore Motor Movement 2

1.1.1 Linear Regression Decoders 3

1.1.2 Kalman Filter Decoders 4

1.1.3 ReFIT Kalman Filter 5

1.1.4 Neural Network Decoders 7

1.1.5 Motor Decoders in Clinical Trials 8

1.2 Sensory Prosthesis using Somatosensory Thalamus 8

1.3 Somatosensory Outflow from Somatosensory Cortex 11

1.4 Assessment of Somatosensory Roots with Non-Invasive Imaging 12

1.5 Thesis Summary 13

Chapter 2. Artificial Neural Networks Decoding Motor Cortex Neurons Improve High-Velocity Motor Movements in Brain Machine Interfaces **16**

2.1 Abstract 16

2.2 Main 16

2.3 Materials and Methods 26

2.3.1 Implantation Procedure 26

2.3.2 Experimental Setup and Finger Task 26

2.3.3 Front-end Processing 27

2.3.4 Software Architecture 27

2.3.5 ReFIT Kalman Filter 28

2.3.6 Neural Network Velocity Decoder 29

2.3.7 Online Training/Testing Protocol 32
2.3.8 Performance Assessment 33
2.3.9 Statistical Analysis 34
Chapter 3. Distinct Perceptive Pathways Selected with Tonic and Bursting Patterns of Thalamic Stimulation 35
3.1 Abstract 35
3.2 Introduction 36
3.3 Materials and Methods 38
3.3.1 Study design 38
3.3.2 Stimulation apparatus 38
3.3.3 Stimulation parameters 39
3.3.4 Thalamic localization 40
3.3.5 Testing protocol 42
3.3.6 Statistical analysis 43
3.4 Results 44
3.4.1 Stimulation pattern controls percept location 44
3.4.2 Percept locations affected by the temporal distribution of pulses 47
3.4.3 Differences in amplitude, charge, and site location 49
3.4.4 Less tingling from bursting stimulation 50
3.5 Discussion 53
3.5.1 Activation of distinct thalamocortical networks through patterned stimulation 53
3.5.2 Anatomical location of stimulation sites 55
3.5.3 Potential for clinical application 56
3.6 Conclusions 57
Chapter 4. Neural Dynamics in Primate Cortex During Exposure to Subanesthetic Concentrations of Nitrous Oxide 58
4.1 Abstract 58
4.2 Introduction 59
4.3 Materials and Methods 60
4.3.1 Surgical procedure 60
4.3.2 Experimental setup and N2O administration 60
4.3.3 Front-end processing—analog to cleaned multi-units 62
4.3.4 Data analysis—spike time dynamics 63
4.3.5 Spectral analysis 65

4.3.6 Finger classification 65
4.3.7 Tuning curves and normalized modulation depth 67
4.3.8 Experimental design and statistical analysis 68
4.4 Results 68
4.4.1 Increased spiking rate with administration of N_2O 68
4.4.2 N_2O modulation of beta and gamma band frequencies 71
4.4.3 N_2O degrades but does not eliminate classification of finger brushings 72
4.5 Discussion 80
4.5.1 Time-frequency dynamics 80
4.5.2 N_2O Degrades M1 Somatosensory Representation 82
4.5.3 Limitations 83
4.6 Conclusions 84
Chapter 5. Classifier Using Pontine Radial Diffusivity and Symptom Duration Accurately Predicts Recurrence of Trigeminal Neuralgia after Microvascular Decompression: A Pilot Study and Algorithm Description 85
5.1 Abstract 85
5.2 Introduction 86
5.3 Materials and Methods 88
5.3.1 Subject Selection and Classification 88
5.3.2 Measuring Normalized Pontine Trigeminal Radial Diffusivity 89
5.3.3 Validation of P_{RD} Metric against Previously Published Results 91
5.3.4 Machine Learning Classification and Cross-Validation 91
5.3.5 Statistical Analysis 93
5.4 Results 94
5.4.1 Surgical Outcomes for TN1 Patients 94
5.4.2 Updated P_{RD} Calculation Differentiates TN1 from TN2 and Pain-Free Controls 96
5.4.3 Radial Diffusivity and Symptom Duration Predict Surgical Outcome 97
5.4.4 Radial Diffusivity Predicts Response to Intervention 98
5.5 Discussion 99
5.5.1 DTI Abnormalities in the Pontine Segment of the Trigeminal Tract 100
5.5.2 Predicting Response to Intervention with Preoperative DTI Measurements 101
5.5.3 Limitations 102
5.6 Conclusions 102
Chapter 6. Discussion 103

6.1 Conclusions 103
6.2 The Future for BMIs 105
Bibliography 107

List of Figures

Figure 2-1. Neural Network Velocity Decoder. 18

Figure 2-2. NN Decoder Outperforms RFKF during Real-time Tests 21

Figure 2-3. NN Better Models High Velocities 25

Figure 2-4. Preferred Training Parameters 32

Figure 3-1. System and experimental setup. 42

Figure 3-2. Stimulation pattern controls percept location. 46

Figure 3-3. Controlled experiment of percept location using tonic and burst stimuli in five subjects. 48

Figure 3-4. Differences in amplitude and charge at the perception threshold. 50

Figure 3-5. Tonic and burst stimuli affect percept quality. 52

Figure 4-1. Influence of nitrous oxide on spiking rate. 70

Figure 4-2. Increased high-frequency power during nitrous oxide. 72

Figure 4-3. Transient degradation of somatosensory information in motor cortex. 75

Figure 4-4. Discriminated single-unit tuning curves. 79

Figure 5-1. Workflow for calculating P_{RD} and predicting response. 90

Figure 5-2. Comparing P_{RD} in TN1 to TN2 plus controls. 97

Figure 5-3. P_{RD} correlated with symptom duration. 98

Figure 5-4. P_{RD} and symptom duration predict outcome. 99

List of Equations

Equation 1-1 3

Equation 1-2 4

Equation 1-3 10

Equation 2-1 33

Equation 4-1 67

Equation 4-2 67

Equation 5-1 92

Equation 5-2 92

Abstract

Many diseases and injuries irreparably harm the brain or spinal cord and result in motor paralysis, widespread sensory deficits, and pain. Often, there are no treatments for these injuries, and therapies revolve around rehabilitation and adapting to the acquired deficits. In this work, we investigate brain machine interfaces (BMIs) as a future therapy to restore sensorimotor function, use BMIs to understand sensorimotor circuits, and use novel imaging algorithms to assess structural damage of somatosensory inputs into the brain.

Brain-controlled robotic arms have progressed rapidly from the first prototype devices in animals; however, these arms are often slow-moving compared to normal hand and arm function. In the first study, we attempt to restore higher-velocity movements during real-time control of virtual fingers using a novel feedforward neural network algorithm to decode the intended motor movement from the brain. In a non-human primate, the neural network decoder was compared with a linear decoder, the ReFIT Kalman filter (RFKF), that we believe represents the state-of-the-art in real-time finger decoding. The neural network decoder outperformed RFKF by acquiring more targets at faster velocities. This neural network architecture may also provide a blueprint for additional advances.

Somatosensory feedback from robotic arms is important to achieve realistic function. The use of somatosensory thalamus was investigated as a site of implantation for a sensory prosthesis in subjects undergoing awake deep brain stimulation surgery (DBS). In this study, electrical stimulation of the thalamus was performed using different stimulation patterns and the evoked sensations were compared. We found that the sensations evoked by bursting (a burst of pulses

followed by a rest period) and tonic (regularly repeating pulses) stimulation were often in different anatomic regions and often evoked differing sensory qualities. These techniques for controlling percept location and quality may be useful in not only in BMI applications but also in DBS therapies to better relieve symptoms and avoid unwanted side effects.

Given the importance of sensory integration in motor functioning, the third study investigated the impact of a pharmacological perturbation on somatosensory content in primary motor cortex measured with Utah arrays implanted in two NHPs. Specifically, during continuous administration of nitrous oxide (N_2O), somatosensory content was assessed by using the neural activity in primary motor cortex to classify finger brushings with a cotton-tip applicator. N_2O degraded but did not eliminate somatosensory content in motor cortex. These findings provide insight into N_2O mechanisms and may lead to further study of somatosensory afferents to motor cortex.

A debilitating facial pain syndrome, called trigeminal neuralgia (TN), is thought to be caused by vascular compression of the sensory root that provides somatosensory feedback from the face. In this final study, magnetic resonance diffusion tensor imaging was used to assess the structural damage of this sensory root. In a retrospective manner, we developed and tested an algorithm that predicted the likelihood of pain relief after surgical treatment of TN. This algorithm could help select patients for surgery with the best chance for pain relief.

Together, these studies advance BMI technologies that attempt to restore realistic function to those with irreparable damage to sensorimotor pathways. Furthermore, using BMIs and novel imaging, this work provides a better understanding of sensorimotor circuits and how sensory pathways can be damaged in disease states.

Chapter 1. Introduction

Injuries and illnesses that disrupt sensorimotor function can devastate lifestyle and take away independence. Perhaps the most severe disorder of movement is complete paralysis. Severe sensory dysfunction can include widespread numbness and a variety of pain syndromes. Brain-machine interfaces (BMIs) may be capable of restoring lost sensorimotor function in the future. The objective of this work is to explore techniques that may enable more realistic functioning of sensorimotor prostheses. Furthermore, we use BMI technology and novel imaging to investigate important sensorimotor circuits and how sensory pathways can be assessed with non-invasive imaging.

1.1 Motor Paralysis

In the United states alone roughly 1.7% of Americans are living with motor paralysis (Armour et al., 2016). Many of these patients also experience a co-occurring numbness from loss of sensory feedback to the brain. The most common etiologies for motor paralysis are stroke, spinal cord injury, amputation, and multiple sclerosis (Ma et al., 2014; Armour et al., 2016). The impact of motor paralysis is profound with more severe disability leading to larger decreases in quality of life (Tate et al., 2002). In particular, the loss of hand function was the most troubling deficit in a survey of quadriplegic patients with spinal cord injury (Anderson, 2004). Unfortunately, current treatments for motor paralysis are largely unsatisfying and focus on rehabilitation and adapting to the new deficits with a variety of adaptive techniques and assistive technologies.

Given the lack of treatment options for those with motor paralysis, many future therapies are being investigated and largely fall into two groups: cellular therapies and brain-machine interfaces (n.d.). Stem cell transplantation is a promising cellular therapy. However, there currently remain a paucity of phase III trials investigating stem cell transplantation (Jin et al., 2019), and widespread clinical therapies could be far into the future.

1.2 Cortical Interfaces to Restore Motor Movement

A brain-machine interface (BMI) decodes the intended motor movement from the brain and uses the signal to control a prosthetic device (Hochberg et al., 2012; Collinger et al., 2013) or reanimate the paralyzed limb (Moritz et al., 2008). However, a neural control signal can be accessed at other locations in the nervous system besides the brain. For example, in patients with amputations, intact peripheral nerves can provide a control signal for a robotic arm (Vu et al., 2020). However, in cases with proximal injuries to the nervous system, e.g. spinal cord injury or brainstem infarction, the cortex can be used as a control signal since the cortical ensembles are known to correlate with motor movements (Georgopoulos et al., 1984).

Many recording electrodes exist with the potential to measure brain signals and include electroencephalogram (EEG) leads placed on the scalp, epidural electrodes placed on the dura, subdural electrodes placed on the brain, and intracortical electrodes that penetrate the surface of the brain (Szostak et al., 2017). Although electrodes that penetrate the surface of the brain are more invasive, they offer the most reliable interface for single unit recordings (Schwartz et al., 2006). Single units are thought to be the neural feature most specific for individual neuronal activity. The intracortical array used in this work to record neural activity is the commonly used Utah microelectrode array (Nordhausen et al., 1996).

A very common site of implantation for intracortical arrays is the primary motor cortex as this area is known to be highly correlated with motor movements (Carmena et al., 2003). Unfortunately, implantation of these intracortical arrays requires a brain surgery. Patients with spinal cord injury were surveyed on whether they would undergo brain surgery and reported more willingness to accept the risk of brain surgery if the implanted BMI device restores function similar to their native arm (Blabe et al., 2015). However, there currently remains a clear performance gap between native arm function and brain-controlled robotic arms, which can be slow and imprecise (Hochberg et al., 2012; Collinger et al., 2013; Aflalo et al., 2015).

In BMI research labs, a prosthetic device can be controlled in one of two modes. In hand-control mode, the device is controlled by the native hand (i.e. with the manipulandum); while in brain-control mode, brain signals are converted to updates for a virtual finger. The algorithm that converts the neural signals to a control signal for the robot arm is called a motor decoder. The performance of motor decoders has rapidly progressed over the last two decades, and there are a variety of decoders that will be discussed in the following sections. For reference, brain-control mode is commonly denoted as either real-time, closed-loop, or online. Offline analyses denote analyses that use data collected during hand-control mode and compare predicted and actual kinematic variables.

1.1.1 Linear Regression Decoders

The first generation of motor decoding algorithms were developed to control a computer cursor and converted neural firing rates to cursor position through simple matrix multiplication:

$$\hat{x}_t = Ay_t$$

Equation 1-1

where $\hat{x}_t$ the horizontal and vertical positions of the cursor, and y_t is a column vector of the firing rates from each of the recorded channels. To calculate A, the subject controls the computer cursor with a joystick while neural firing rates and cursor position are recorded. The matrix A is then calculated to minimize the mean-squared error (MSE) between $\hat{x}_t$ and the true cursor position.

The first three studies to use a linear relationship between spiking rate and cursor position were experiments in non-human primates (Serruya et al., 2002; Taylor et al., 2002; Carmena et al., 2003). The decoder used in Taylor et al. (2002) was based on a concept called "population vectors." It is conceptually similar and provides similar performance to the linear relationship in Eq. 1-2 but uses normalized firing rates and a different matrix to convert firing rate to cursor position depending on whether the firing rate increases or decreases.

1.1.2 Kalman Filter Decoders

To decode smoother trajectories, the Kalman filter was investigated as a motor decoder. The Kalman filter, named after Rudolf E. Kalman, was developed in the 1950-60s (Swerling, 1959; Kalman, 1960; Kalman and Bucy, 1961). The objective of Kalman filter is to estimate the position/velocity of an object being tracked (i.e. computer cursor) from noisy measurements (i.e. neural firing rates). The equation that describes the Kalman filter is given below in Eq. 2:

$$\hat{x}_t = A\,\hat{x}_{t-1} + K_t(y_t - C\,\hat{x}_{t-1})$$

Equation 1-2

where $\hat{x}_t$ is column vector of cursor position/velocity estimates, $\hat{x}_{t-1}$ is column vector of cursor position/velocity estimates from the previous time step, y_t is a column vector of neural firing rates, and A, K_t, and C are learned parameters based on training data. The Markovian assumption of the Kalman filter assumes that the current estimate of position/velocity is independent of all past information except position/velocity estimates of the previous time step ($\hat{x}_{t-1}$). Thus, Eq. 2 states that the estimate of position/velocity is linear combination of the previous time step's position/velocity ($\hat{x}_{t-1}$) and the neural firing rates y_t. The values of A, K, and C are chosen to optimize this trade off as described by Wu et al. (Wu et al., 2004).

Applying the Kalman filter to motor decoders was first suggested by Wu et al. (Wu et al., 2004), and a rigorous comparison of the Kalman filter and linear regression was described by Kim et al. (Kim et al., 2008). In this study, human participants with motor paralysis were implanted with intracortical arrays in primary motor cortex. After recovering from surgery, participants performed a center-out cursor task with a 500 ms hold time. The differences in performance between the linear filter and Kalman filter were not substantial in terms of acquisition time or percent of missed trials. However, the target trajectories were much smoother with the Kalman filter and several additional numerical metrics were introduced to quantify non-smooth trajectories.

1.1.3 ReFIT Kalman Filter

To improve the Kalman filter further, new training methods were investigated. The Kalman filter was designed to optimally estimate position and velocity of targets when the true target position is not known. However, in a BMI application, the target position is known because the subject can directly visualize the cursor that is being moved. Thus, the Kalman filter can be

improved when the estimated velocity direction is not directed toward the target. In 2012, Gilja et al. introduced the recalibrated feedback intention–trained Kalman filter (RFKF) (Gilja et al., 2012). The process for training this filter involves first calculating a classic Kalman filter. The NHP then controls the cursor using the classic Kalman filter. From this data, an error is assigned whenever the estimated velocity direction is not directed toward the target. The Kalman filter parameters are then adjusted to minimize this error in the same manner that the original Kalman filter was trained. The re-trained filter is the RFKF.

RFKF substantially improved cursor control when compared to the classic Kalman filter. The cursor task described in Gilja et al. required a 500 ms hold time to be considered successful (Gilja et al., 2012). The calculation of the acquisition time did not include the mandatory 500 ms hold time. The acquisition time was around 1.6s for the Kalman filter, 0.6s for RFKF, and 0.5s when controlling the cursor in hand-control mode. Furthermore, the path to target was more direct with the RFKF than the classic Kalman filter.

The RFKF was extended by Kao et al. by adding a hidden Markov model (Kao et al., 2016). From the neural signals, not only is the position/velocity of the cursor calculated but the probability that the cursor is in certain movement or stationary states. To move the cursor, the cursor must be in a movement state. In this work, the cursor was moved over a grid of N boxes representing choices (like a keyboard). The correct choice was selected by hovering over the box for 200 ms. Thus, each trial conveyed $log_2(N-1)$ bits of information. By dividing the total bits of information by the acquisition time, a bit rate can be calculated. Through the addition of the Markov model, the bit rate increased by an average of 9% over the RFKF alone to around 5 bps.

While many groups use motor decoders based on RFKF, other decoding options are also in use. In human trials, Collinger et al. use ridge regression with an intention-based re-training

step (Collinger et al., 2013). Shanechi et al. trained a Poisson process model with an instantaneous firing rate that maps to kinematic variables that is also parameterized with latent states corresponding to possible targets (Shanechi et al., 2013). However, these methods are not known to outperform RFKF.

1.1.4 Neural Network Decoders

With the revolutionary use of deep learning in other fields (Krizhevsky et al., 2012), many believed that neural networks could be the future of motor decoding. In 2012, Sussillo et al. introduced a recurrent neural network decoder (RNN) that outperformed the classic Kalman filter (Sussillo et al., 2012). The RNN improved the time required for a brain-controlled cursor to acquire a target from ~ 1.5s with the Kalman filter to around ~0.9s with the RNN. However, as mentioned above, this improvement fell short of RFKF (with acquisition times around ~0.6 ms for a similar task conducted by the same research group in a follow up paper (Gilja et al., 2012)). Algorithm complexity has since been extended by combining RNNs with hidden states and auto-encoders (Pandarinath et al., 2018; Hosman et al., 2019), although these implementations have not been demonstrated online. Two neural networks have been demonstrated during online testing. Schwemmer et al. decode Utah array output using a neural network architecture with long short-term memory, convolutional, and fully connected layer to classify movement types (e.g. index extension/flexion), which is then used to animate the native arm via functional electrical stimulation (Schwemmer et al., 2018). George et al. decode a peripheral nerve interface with a convolutional neural network to control a prosthetic hand and found performance similar to that of a Kalman filter based approach (George et al., 2018).

1.1.5 Motor Decoders in Clinical Trials

Many of the aforementioned motor decoders have found their way into human clinical trials (Hochberg et al., 2012; Collinger et al., 2013; Aflalo et al., 2015). Hochberg and colleagues (2012) use a Kalman filter (Eq. 2) while Collinger and colleagues (2013) and Aflalo and colleagues use regularized variants of linear regression. Training the filter is accomplished by automatically moving the robot arm and instructing the subject to imagine he/she is controlling the movements. Just as the Kalman filter can be retrained to provide the RFKF, linear regression can also be retrained with an intention-based training step by controlling the robot arms in brain-control mode and penalizing the algorithm when it causes the arm to move away from the target (Collinger et al., 2013).

1.2 Sensory Prosthesis using Somatosensory Thalamus

Realistic motor prostheses should not only allow for accurate motor movements but should also provide somatosensory feedback. A variety of loci exist for placement of sensory prosthetic devices including peripheral nerve sites and central sites such as the cortex, thalamus, and spinal cord (Lebedev and Nicolelis, 2017). Wilder Penfield conducted some of the first experiments in human subjects by electrically stimulating somatosensory cortex during awake brain-surgery cases (Penfield, 1960). The well-organized and well-understood somatotopy of the somatosensory cortex allows the location of evoked sensation, called percepts, by stimulation of a specific region of cortex. Experiments using intracortical microelectrode arrays implanted in somatosensory cortex demonstrate the feasibility of focal hand percepts with electrical stimulation (Flesher et al., 2016). Most percepts in this study were described as “possibly naturalistic.” There have also been non-tingling percepts reported in small intraoperative studies

using electrical stimulation through cortical grids, and the percepts are described with terms such as “wind running down the hand” (Johnson et al., 2013). Peripheral nerve interfaces have also been employed for somatosensory restoration (Tan et al., 2014; Wendelken et al., 2017). In one patient, patterned stimulation through a peripheral interface produce naturalistic percepts (Tan et al., 2014).

Somatosensory percepts from electrical stimulation of somatosensory thalamus (ventral caudal nucleus Vc) have also been studied in detail during awake deep-brain stimulation surgeries (DBS) (Tasker et al., 1982; Lenz et al., 1988; Lenz et al., 1993; Davis et al., 1995; Lenz et al., 2000; Ohara et al., 2004; Chien et al., 2017). Stimulation of somatosensory thalamus was often required to localize the site of final lead implantation. Studies have revealed that modalities (i.e. pressure, touch, and vibration) can be clustered spatially (Ohara et al., 2004; Chien et al., 2017). Another advantage for using somatosensory thalamus as a locus of stimulation is its compact structure, which allows access to all facial and body somatotopy in a small volume. Furthermore, DBS implantation procedures are routinely performed in a large number of surgical centers.

Many of the initial studies reported that thalamic percepts were primarily described as “tingling” or “pins and needles” (Lenz et al., 1988; Dostrovsky et al., 1993; Davis et al., 1996). However, Ohara et al. reported that naturalistic percepts are more frequently encountered posterior ($p < 0.05$) or inferior ($p = 0.07$) to the core region when compared to unnatural percepts (Ohara et al., 2004). Additionally, out of 122 percepts described as mechanical or movement, percepts were more frequently naturalistic at sites with overlapping projected and receptive fields. Projected field refers to the location of the sensation evoked with electrical stimulation while receptive field refers to the location where tactile stimulation evokes or modulates a single-

unit response at the recording electrode. More recently, by reducing stimulation amplitude to around the threshold of perception, Swan et al. found that a majority of percepts (55%) were perceived as "natural" to patients during intraoperative testing with a microwire bundle implanted in somatosensory thalamus (Swan et al., 2017). Furthermore, they found that stimulation patterns using increasing frequency ramps were "slightly more" naturalistic than constant frequency, tonic stimulation. Heming et al. similarly found naturalistic (possibly to totally) percepts in 23% of the microstimulation sites. However, 333 Hz tonic patterns were found to be more often naturalistic than a variety of unconventional patterns that included thalamic spike trains recorded from previous patients (Heming et al., 2010).

As described above, percept quality is likely affected by both stimulation site and stimulation patterns; however, stimulation site, pattern, and waveform are coupled in their effect on somatosensory quality. As described in detail by Plonsey and Barr (Plonsey and Barr, 2007), the activating function approximates the likelihood of initiating a neuronal action potential at a given distance from the electrode for a given stimulation waveform. The activating function describes an infinite neural axon along the *z*-axis and an idealized point source on the *x*-axis and is given in Eq. 1.3.

$$A(z) = {\partial^2 \phi_e}/{\partial z^2}$$

Equation 1-3

According to this expression for the activating function, the segment of the axon closest to the electrode is most likely to initiate an action potential with a cathodic stimulation (negative polarity, monophasic waveforms), and computational models support this conclusion (McIntyre and Grill, 1999). However, anodic stimulation (positive polarity, monophasic waveforms) has been shown in computational models to be more selective in activating local cells than cathodic

stimulation (McIntyre and Grill, 1999; Miocinovic and Grill, 2004). Furthermore, high-frequency patterns more efficiently activate axons of passage while low-frequency stimulation better activates local cells when the soma is closer to the electrode than the axon (McIntyre and Grill, 2002; Yi and Grill, 2018). Thus, a coupling exists between the location of activated neural elements, stimulation waveform, and stimulation pattern and must be considered when trying to achieve naturalistic somatosensory percepts.

1.3 Somatosensory Outflow from Somatosensory Cortex

Somatosensory pathways do not terminate in somatosensory cortex but project to many other cortical areas (e.g. secondary somatosensory cortex, area 5 of parietal cortex, supplementary motor area, motor cortex) and subcortical areas that include somatosensory thalamus (Jones and Peters, 2012). Previous animal studies suggest that somatosensory afferents to M1 are largely mediated via corticocortical connections from S1 (Andersson, 1995; Farkas et al., 1999; Mao et al., 2011). Furthermore, connections from somatosensory cortex to primary motor cortex are hypothesized to be important in sensorimotor integration and blocking these pathways can lead to a variety of sensorimotor deficits and difficulties learning new motor tasks (Hoffer et al., 2005; Petrof et al., 2015). In a gripping and lifting task, Brochier et al. showed that injecting a $GABA_A$ agonist into somatosensory cortex of a NHP led to an abnormal increase in gripping strength followed by abnormal application of gripping and lifting forces (Brochier et al., 1999). Pavlides et al. demonstrated that a lesion in the somatosensory cortex of a NHP lead to difficulty learning novel motor tasks involved with catching food pellets, although some previously learned motor tasks, such as picking up food pellets, were preserved (Pavlides et al., 1993).

The connections from somatosensory to motor cortex present an opportunity to evaluate whether outflow from somatosensory cortex can be modulated, in our case, with the pharmacologic agent, nitrous oxide (N_2O). N_2O is in a class of medications, like ketamine, that is thought to antagonize glutamatergic NMDA receptors (Jevtovic-Todorovic et al., 1998) and known to have anti-depressant (Tadler and Mickey, 2018), psychedelic (Icaza and Mashour, 2013), and analgesic effects (Parkhouse et al., 1960) at subanesthetic concentrations. While ketamine was found to disrupt somatosensory content in M1 at anesthetic doses, the effect of N_2O is unknown. Understanding how S1 to M1 transfer can be affected under pharmacologic perturbations may one day help us introduce somatosensory feedback into BMIs to allow sensorimotor integration and better prosthetic function.

1.4 Assessment of Somatosensory Roots with Non-Invasive Imaging

Somatosensory pathways originate from outside the central nervous system (CNS), and these pathways carry information from the environment to the brain for processing. However, if the neural pathways into the brain are damaged, excruciating pain syndromes can result. An extremely debilitating facial pain syndrome, called trigeminal neuralgia (TN), is thought to be caused by vascular compression of the trigeminal root (Burchiel, 2003). The vascular compression is thought to cause demyelination in the trigeminal root that has been observed in histopathological studies (Love and Coakham, 2001). Fortunately, certain subtypes of this disease, e.g. Burchiel type 1, are well-controlled with surgical treatment, typically microvascular decompression (MVD). Pain-free outcome reaches 76% of patients with type 1 TN at a mean follow-up of 1.7 years (Holste et al., 2020). However, other subtypes of TN such as those with a constant pain component, are known to be less responsive to surgical intervention (Tyler-Kabara

et al., 2002), and surgical intervention is inherently risky (Hanakita and Kondo, 1988). To help identify patients most likely to respond to surgical intervention, clinical scoring algorithms have been proposed (Hardaway et al., 2019).

Recently, abnormalities in magnetic resonance diffusion tensor imaging (MR-DTI) of the trigeminal root and root entry zone have been found in TN patients (Herweh et al., 2007; Leal et al., 2011). MR-DTI measures the magnitude and direction of water diffusion in human tissue and has been used as a non-invasive method to assess microstructural changes in human diseases (Horsfield and Jones, 2002). For MR-DTI in TN, several studies have suggested that this imaging modality may help predict the response of patients to treatment (Hung et al., 2017; Willsey et al., 2019). In particular, radial diffusivity (RD) represents the diffusion of water perpendicular to the direction of maximal diffusion while axial diffusivity is in the direction of maximal diffusion (Alexander et al., 2007). Increases in RD - with constant axial diffusivity – is often related to demyelination (Song et al., 2002). Given the known role of demyelination in the pathophysiology of trigeminal neuralgia (Love and Coakham, 2001), we investigate whether RD helps assess the trigeminal root in patients with TN.

1.5 Thesis Summary

The objective of this thesis is to leverage novel engineering technologies to better understand and treat disorders of sensorimotor pathways. Specifically we use neural interfaces (cortical and thalamic) to (1) improve decoding of motor movements for those with motor paralysis, (2) characterize the role of patterned thalamic stimulation when generating somatosensory percepts, (3) evaluate intact somatosensory to motor cortex pathways using a cortical interface during a

pharmacologic perturbation, and (4) assess structural changes in a sensory root with MR-DTI to better predict the response of patients to surgical intervention.

In Chapter 2, an online feedforward neural network decoder is used to control finger prostheses in real-time and demonstrates substantially improved performance over ReFIT Kalman filter techniques. The decoders enable higher velocity, and thus, more naturalistic motor movements compared to the ReFIT Kalman filter. This work provides a blueprint to leverage artificial networks for the purpose of decoding biological neural networks to help restore naturalistic motor movements in paralyzed patients.

Chapter 3 explores the use of tonic and bursting stimulation patterns of electrical stimulation in human somatosensory thalamus (ventral caudal nucleus; Vc), which is highly amenable to intraoperative study during awake deep brain stimulation surgeries. The percept locations for bursting and tonic patterns are compared during electrical stimulation and provide insight into how stimulation pattern may select for distinct anatomic pathways. This work can help unravel the coupled effect of stimulation waveform/pattern and stimulation site when generating specific sensory modalities.

Using an intracortical interface implanted in primary motor cortex, we evaluate the effect of 70% inhaled N_2O on the somatosensory to motor cortex afferents in Chapter 4. This cortico-cortical connection is hypothesized to be especially important in sensorimotor integration and in learning novel motor tasks. The impact of nitrous oxide on this connection may (1) provide mechanistic insights into the psychedelic, anti-depressive, and analgesic properties of N_2O at subanesthetic doses and (2) help develop a methodology to evaluate the strength of this important cortico-cortical connection for future sensorimotor brain-machine interfaces.

Finally, in Chapter 5, we evaluate a non-invasive algorithm to assess the integrity of the sensory root that carries facial sensation in patients with trigeminal neuralgia. Specifically, MR-DTI is used – along with symptom duration – to predict the pain response to surgical intervention (microvascular decompression). The algorithm developed combining MR-DTI and symptom duration may help select surgical patients with the greatest chance of a pain free outcome.

Chapter 6 discusses the relevance of the thesis work to various sensorimotor pathologies and how the work can be further extended.

Chapter 2. Artificial Neural Networks Decoding Motor Cortex Neurons Improve High-Velocity Motor Movements in Brain Machine Interfaces

A version of this manuscript is in preparation for submission using a brief communication format

2.1 Abstract

Brain-controlled prosthetic fingers often move slower than actual fingers. To achieve higher velocities, we show that a feedforward neural network (NN) can use neural activity from an intracortical array in a non-human primate to control virtual fingers in real-time. The NN outperforms a state-of-the-art decoder (ReFIT Kalman filter) by quickly acquiring targets at higher velocities while stopping precisely on targets. This architecture provides a blueprint for future high-velocity motor decoders to restore realistic movements.

2.2 Main

Brain prostheses offer hope to the very high numbers of Americans (~ 1.7%) with sensorimotor impairments (Armour et al., 2016). To this end, cortical brain-machine interfaces have been demonstrated in patients successfully using robot arms to bring a drink to the mouth (Hochberg et al., 2012) or to stack cups (Collinger et al., 2013). Motor decoding algorithms are required to convert brain signals into position and velocity updates for the prosthetic device. Motor decoding at many centers is based on a technique called ReFIT kalman filter estimation (Gilja et al., 2012; Kao et al., 2016), although other methods with similar performance have been

previously reported (Hochberg et al., 2012; Shanechi et al., 2013). Early neural network decoders, prior to recent advancements in hardware, toolboxes, and training methods, were not found to improve performance over standard linear methods (Wessberg et al., 2000; Carmena et al., 2003). Many advanced techniques employing recurrent neural networks and variational inference techniques show great promise for predicting prosthetic kinematics from brain signals (in offline testing); however, these techniques have not been used in real-time to control prosthetic devices (in online testing), likely because of the computational complexity (Pandarinath et al., 2018; Hosman et al., 2019). Online testing of a recurrent neural network (Sussillo et al., 2012) was demonstrated to control a computer cursor in a non-human primate implanted with motor cortex arrays but has not outperformed RFKF. George et al. demonstrated control of hand and finger movements in human amputees with peripheral nerve interfaces using a convolutional neural network but did not outperform a Kalman filter (George et al., 2018). In this work, we demonstrate, for the first time, online neural network decoding using a feedforward network to control finger prostheses in real-time that substantially outperforms ReFIT Kalman filter techniques. This work therefore may provide a starting point to leverage artificial networks for the purpose of decoding biological neural networks to help restore naturalistic motor movements in paralyzed patients.

One male rhesus macaque was be implanted with Utah arrays (Blackrock Microsystems, Salt Lake City, Utah) in the hand area of primary motor cortex (M1) as shown in Fig. 1a. The macaque was trained to sit in a chair and perform a finger task. Using a hand manipulandum that maps the finger positions to virtual positions, the animal was trained to place one or more virtual fingers on randomly appearing circular targets. During this hand-control mode, the spike-band power was recorded. Spike-band power is the time-averaged power in the 300-1000 Hz

frequency band and provides a high SNR correlate of the dominant single unit spiking rate on any particular channel (Nason et al., in press). After completion of this task, a decoder was trained to map spike-band power to velocity estimates for the index (D2) and middle-ring-small finger group (D3-5) as shown in Fig. 1B. A detailed description for decoding one finger is described by Vaskov et al. (Vaskov et al., 2018), and the first known description of simultaneous control of two-degrees of freedom is described by Nason et al. (Nason et al., 2019). In this work, we compare performance using our novel neural network decoder using learned time features (NN; Fig. 1C) versus the ReFIT Kalman filter (RFKF) developed by Nason et al. (Nason et al., 2019), which we believe is representative of the current state-of-the-art in motor decoding of two-dimensional fingers.

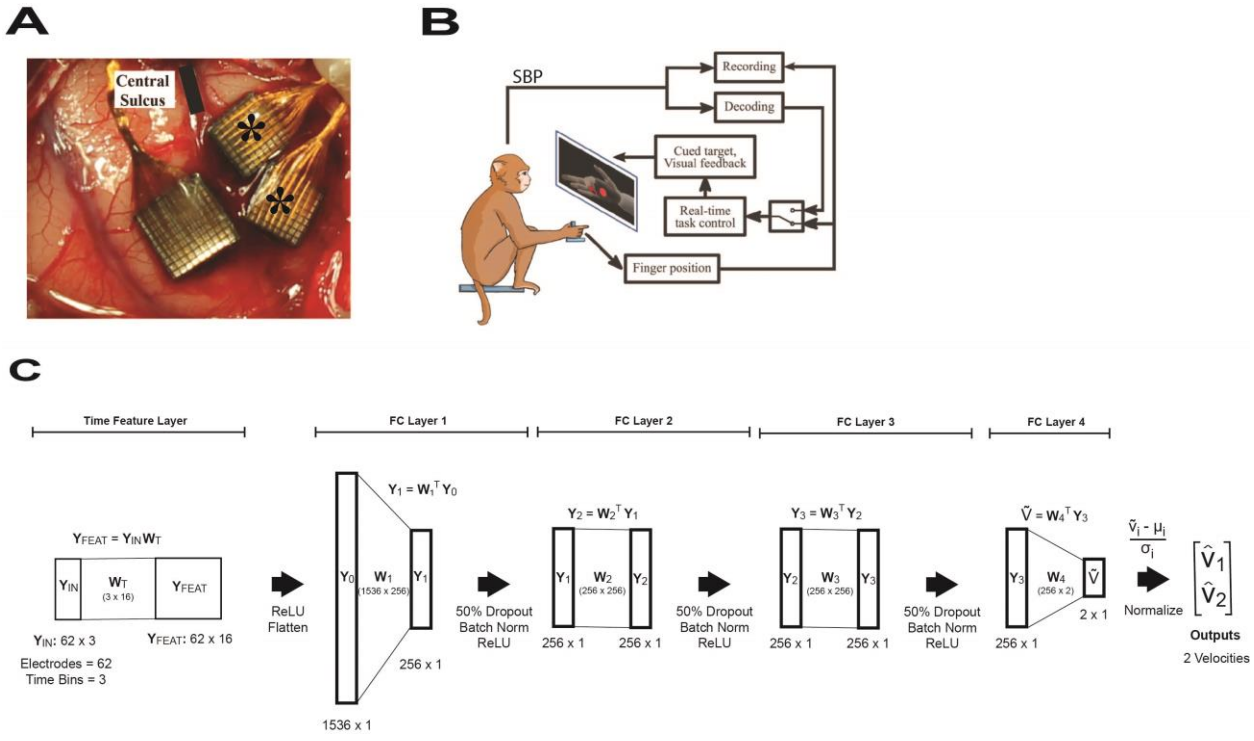

Figure 2-1. Neural Network Velocity Decoder.
(A) Image of Utah array implants. Two split Utah arrays were implanted in primary motor cortex immediately anterior to the central sulcus and denoted with asterisks (*). The array in primary somatosensory cortex was not used in this analysis. (B) Experimental Setup. The NHP is controlling the virtual finger with the hand manipulandum in hand-control mode or using SBP to control the virtual finger in brain control mode. (C) NN architecture. The network consists of

five layers. The input to the network is Y_{IN} that is a 62 x 3 data matrix that corresponds to 62 input electrodes and the 3 previous 50-ms time bins. The time feature layer converts the last three 50-ms time bins for all the electrodes into 16 learned time features for each electrode. The equation representing the operation is given above the graphical description of the layer. The arrow indicates that each element passes through a ReLU function and is then flattened to a 1536x1 array. The remaining four layers are fully-connected layers with an associated weight matrix, denoted by W. The first three layers consist of 256 hidden neurons and process the hidden neuron output first with 50% dropout, then batch normalization, and finally with a ReLU function. The final layer, FC-Layer 4 has two neurons – that are normalized – and then represent final velocity estimates of the two fingers a, $\hat{\boldsymbol{v}}_{\boldsymbol{1}}$ and $\hat{\boldsymbol{v}}_{\boldsymbol{2}}$. SBP = spike-band power. Panel B from (Vaskov et al., 2018) and licensed under CC BY 4.0 (https://creativecommons.org/licenses/by/4.0/) / "spikes" replaced with SBP.

The neural network architecture was designed to reduce computational complexity to allow same day training and online motor decoding. As most online decoders incorporate time history (Hochberg et al., 2012; Collinger et al., 2013), the NN was designed so that an initial layer constructed 16 time features per electrode from the preceding 150 ms of spike-band power (time feature layer in Fig. 1C). These time features were then input to into 4 fully-connected layers (FC Layers 1-4), and the output was a normalized velocity value for each finger. The network parameters were chosen to optimize performance on offline data sets. The predicted velocity from the neural network was normalized to unit variance which was empirically found to decrease the training time. Consequently, the normalized velocity values were scaled with a gain calculated during training so that the average peaks of the estimated and actual velocity were equal (see Materials and Methods for details).

In real-time (online) testing over two consecutive days and 1326 total trials, the NN significantly outperformed the RFKF with 1.66 ± 0.03 bits per second (bps) for the NN and 1.30 ± 0.02 bps for RFKF ($p < 10^{-5}$). The bit rate calculation excluded target hold time, but the mean bit rate calculation included unsuccessful trials (trial bit rate = 0). Unsuccessful trials were sporadic for both decoders and reflective of decreased effort (4 for RFKF, 6 for the NN).

Representative raw finger tracings are depicted in Fig. 2A for the RFKF and in Fig. 2B for the NN. The tracings illustrate the higher target acquisition rate for the NN (31 targets in 50 sec) than the RFKF (20 targets in 50 sec). The NN outperformed RFKF on days where the NN was used first ($p < 10^{-5}$) and on days when the RFKF was used first ($p < 10^{-5}$) as illustrated in Fig. 2C. To better understand why the NN outperforms the RFKF decoder, the relative distance to the target for the average trial was compared for each decoder (in Fig. 2D). As seen in the figure, virtual fingers controlled by the NN close in to the target (dashed gray line) more quickly and sooner than the virtual fingers controlled by RFKF. Excluding mandated target hold time, the mean acquisition time for the NN was 1250 ms and for RFKF was 1530 ms ($p < 10^{-5}$). The NN-controlled virtual finger was more responsive and generally achieved higher velocities than the RFKF-controlled finger (Fig. 2E). The time to peak of the averaged velocity was 350 ms for the NN and 550 ms for RFKF. The peak of the averaged velocity was 0.89 ± 0.03 u/sec for the NN and was 1.6 times greater than 0.56 ± 0.02 u/sec for RFKF ($p < 10^{-5}$) where u denotes arbitrary units such that 1 was full extension and 0 was full flexion.

To characterize the remaining difference between NN control and actual finger movements, the neural network decoder was then compared with the hand-controlled virtual finger in one day of testing with 453 trials in an A-B-A-B sequence of tests beginning with the NN. Controlling virtual finger movements with the native finger outperformed the NN decoder with a bit rate of 2.24 ± 0.11 bps for hand control and 1.91 ± 0.06 bps for NN control ($p = 0.0007$). Better performance with hand control was expected since the virtual fingers track the position of the actual finger movements. Fig. 2G illustrates that the hand-controlled fingers more quickly acquired the target with an acquisition time of 863 ± 35 ms compared to 1049 ± 36 ms for the NN ($p < 10^{-5}$). However, the time to peak of the average velocity was within one 50-ms

bin with the hand control occurring at 350 ms and the peak for the NN at 300 ms. The peak velocity was 2.95 ± 0.23 u/s for hand control and was 2.3 times greater than 1.27 ± 0.07 u/s for the NN decoder ($p < 10^{-5}$).

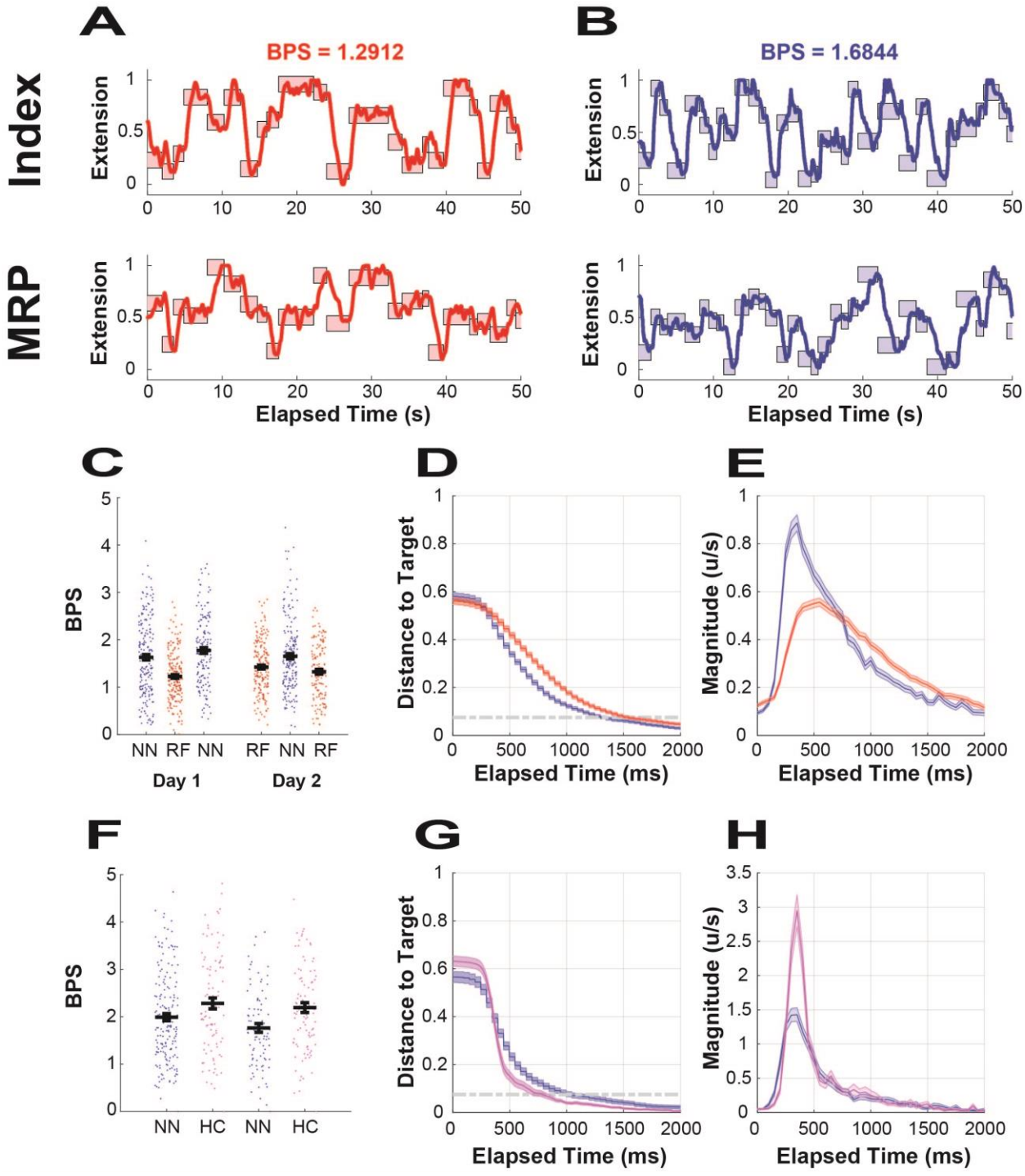

Figure 2-2. NN Decoder Outperforms RFKF during Real-time Tests

(A-B) Decoded Finger Tracings. Raw decoded position using the RFKF (red) and NN (blue) for the index finger (top pane) and middle-ring-pinky (MRP) fingers, which are locked together (bottom pane). The targets are represented as the shaded box. The x-axis denotes the elapsed time, 50 sec, and the y-axis denotes the proportion of finger extension, i.e. 1 is fully extended and 0 is fully flexed. These time windows are representative of the average decoding performance as measured by bit rate. (C) Bit Rate Population Data. For each run, the bit rate is indicated with a dot (blue = NN, red = RFKF). The black bars represent the mean and S.E.M. (D) Virtual Finger Distance to Target. The mean distance versus elapsed trial time (blue = NN; red = RFKF). The y-axis units, u, are the proportion of total range of motion with 1 being full extension and 0 being full flexion. The shaded color is the S.E.M. (E) Virtual Finger Velocity. Mean velocity versus elapsed trial time for the RFKF (red) and NN (blue). (F) Bit Rate population data for the NN (blue) and hand control (magenta). (G) Distance to target for NN (blue) and hand control (magenta). (H) Virtual finger velocity for NN (blue) and hand control (magenta). RF = ReFIT Kalman filter/RFKF; NN = neural network.

The impact on performance of the individual network components was assessed through an offline analysis based on three consecutive days of recorded spike-band power during hand-controlled finger task. Illustrative examples of predicted versus actual 2 DOF finger position (D3-5) are given for NN of increasing complexity: 2 layers, 2 layers with time history, 4 layers, and 4 layers with time history (Fig. 3A). For comparison, these networks were compared with Kalman Filter and ridge regression decoders. Six correlation values between estimated velocity and true velocity (3 days x 2 fingers) were calculated. The mean (± S.E.M.) correlation was 0.44 ± 0.02 for a 2-layer network, 0.64 ± 0.01 for a 2-layer network with time history, 0.61 ± 0.01 for a 4-layer network, and 0.67 ±0.01 for a learned-time-feature layer feeding 4-layer fully-connected layers (as in Fig. 3B). Thus, transitioning from a 2-layer NN to either a 2-layer NN with time history or a 4-layer NN without time history resulted in a substantial increase in performance. Combining both time history and a 4-layer NN (i.e. the NN used in online demonstrations) provided the best offline performance. Exploration of the parameter space in the offline analysis did not suggest obvious performance improvement with additional layers or time features. For comparison, the correlation of ridge regression (without time history) was 0.52 ± 0.02 and the Kalman filter was 0.59 ± 0.01 (Fig. 3C). Using one-way ANOVA analysis, the 4-

layer NN with time history was significantly greater than ridge regression ($p < 10^{-5}$), KF ($p = 0.007$), and 2-layer NN ($p < 10^{-5}$). The difference between the correlation for the 4-layer NN with time history was not statistically different from either the 2-layer NN with time history ($p = 0.67$) or the 4-layer NN ($p = 0.10$).

An ideal motor decoder accurately predicts low or zero velocity of a slow moving or stationary finger as well as high speeds for a fast-moving finger. Given that online tests show that the peak velocity of the RFKF was less than that of the NN decoder, we characterized the relationship between actual and predicted normalized velocities at both high (> 1.33) and low (< 1.33) values using a linear regression analysis – where the velocity values are normalized by the standard deviation of the true velocities. First, when considering low velocities, it is extremely important for a motor decoder to accurately predict velocities near zero when the actual finger is stopping. To quantify this accuracy, the correlation coefficient between the predicted and actual velocity is typically used. At low velocities (< 1.33), the NN decoder is more correlated with actual finger velocities than the RFKF decoder with a correlation coefficient of 0.51 ± 0.01 vs. 0.46 ± 0.01 ($p = 0.001$).

At high velocities, however, the NN was also superior to the RFKF. Accurately achieving high velocities can allow more rapid movements and decrease the time to target, although a high-velocity is not necessary to complete the task. For the Kalman filter at high velocities, there was actually not a statistically significant correlation between predicted and actual velocities ($p = 0.12$, $R = 0.24 \pm 0.04$, slope $= 0.40 \pm 0.04$). However, the predicted high velocities were linearly correlated to the actual velocities for the NN decoder ($p = 0.01$, $R = 0.33 \pm 0.03$, slope $= 0.55 \pm 0.03$). Furthermore, the slope achieved for the NN decoder was significantly greater than that of the Kalman filter ($p = 0.001$), suggesting that the NN decoder was able to match the velocity at

high values. Thus, in the offline analysis, the NN able to better match the high velocities of the actual finger without being less predictive at low velocities, which is important for stopping. These findings are graphically summarized in Fig. 3D, where the relationship between predicted velocity and actual velocity is depicted and scaled to constrain its predicted velocity to be less than 0.5 when the true velocity is near zero. With equivalent stopping power and matching the findings in online tests, the NN achieved 1.6 times greater velocities at 2.11 ± 0.04 than the 1.31 ± 0.02 of the Kalman filter ($p < 10^{-5}$) when the actual velocity was 4.0.

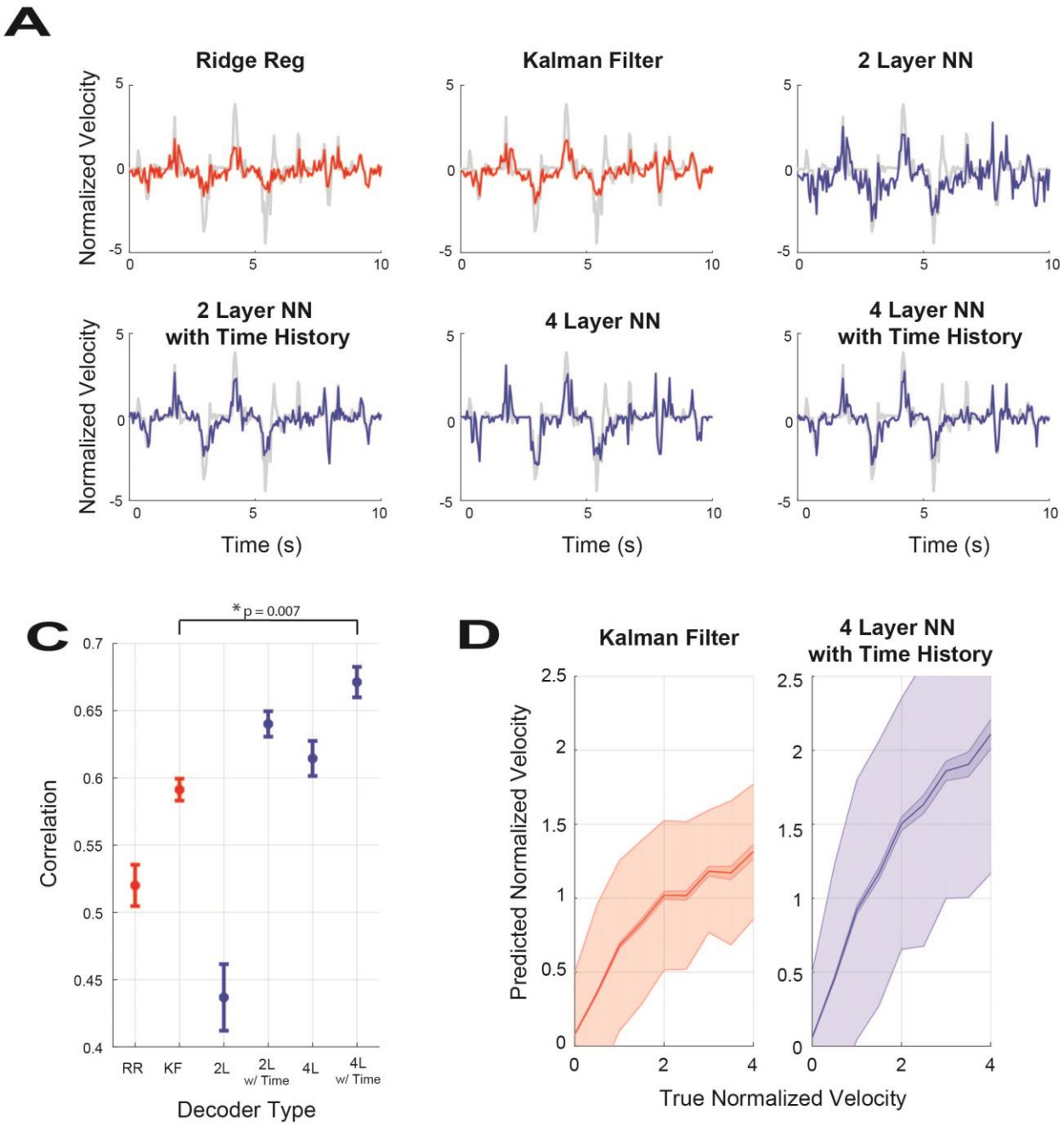

Figure 2-3. NN Better Models High Velocities
(A) Comparisons of actual velocity (grey) and decoded velocity for linear decoders (red) and NN decoders (blue). No units are used for velocity since velocity was normalized by the standard deviation of actual velocities during the entire run. (C) Mean (and S.E.M.) offline correlation between actual and predicted velocity for 2 fingers over 3 consecutive days. The asterisk (*) denotes statistical significance between the KF and 4L w/ Time. (D) True and predicted normalized velocity are illustrated for the Kalman Filter (red/left) and NN (blue/right). Ridge Reg = RR = Ridge Regression; KF = Kalman Filter; NN = neural network; 2L = 2-layer neural network; 2L w/ Time = 2-layer neural network with a preceding time feature layer; 4L = 4-layer neural network; 4L w/ Time = 4-layer neural network with a preceding time feature layer

2.3 Materials and Methods

2.3.1 Implantation Procedure

The protocols herein were approved by the Institutional Animal Care and Use Committee at the University of Michigan. One male rhesus macaque was implanted with Utah arrays (Blackrock Microsystems, Salt Lake City, Utah) in the primary motor cortex (M1). Under general anesthesia and sterile conditions, a craniotomy was made and M1 was exposed using standard neurosurgical techniques. The arcuate sulcus of M1 was visually identified, and the array was placed where this sulcus touches motor cortex, which is a known landmark of hand area. The incision was closed, and routine post-anesthesia care was administered.

2.3.2 Experimental Setup and Finger Task

The macaque was trained to sit in a monkey chair (Crist Instrument, http://www.cristinstrument.com), with his head secured in customized titanium posts (Crist Instrument), while the Utah array was connected to the Cerebus neural signal processor (NSP, Blackrock Microsystems). The arms were secured in acrylic restraints. The hand contralateral to the motor cortex implant was placed in a manipulandum, described by Vaskov et al. (2018), that translates finger position to a number between one (full extension) and zero (full flexion). A computer monitor was in plain sight for the NHP with an enlarged virtual hand. The virtual finger could be controlled in either hand-control mode (i.e. with the manipulandum) or in brain-control mode (i.e. brain signals converted to updates for virtual finger). Brain-control mode is commonly denoted as either real-time, closed-loop, or online. The two-dimensional finger task is identical to the task developed by Nason et al. except performed on random instead of center-out

targets (Nason et al., 2019). The finger task required placing either the virtual index and/or ring finger on the target for 750 ms during training mode and 500 ms during testing mode (testing vs training modes will be explained in a subsequent section). The target size was 15% of the active range of motion. With target acquisition, apple juice was automatically administered through a tube placed in the animal's mouth.

2.3.3 Front-end Processing

The Utah array was connected to the Cerebus neural signal processor (Blackrock Microsystems, Salt Lake City, UT) through a cable. Although there were 96 channels available, only channels where the morphology of threshold crossing was consistent with bipolar spikes in the time domain were included, leaving 62 channels. The Cerebus system communicated data sampled at 30 kHz to the xPC Target environment (Mathworks, Natick, MA) where front-end signal processing was performed. The output data was bandpass filtered in the 250-1000 Hz band. The root-mean-square power was calculated and binned at regular 50 ms time intervals. This binned RMS value is referred to as spike-band power. We have previously shown that this band is highly correlated with and specific to the spiking rate of single units near the recording electrode (Nason et al., in press).

2.3.4 Software Architecture

A separate computer with 2070 super NVIDIA GPUs (NVIDIA, Santa Clara, CA) was connected to the xPC. This computing box was called the e**X**ternal **G**raphic processing unit **PC** (xGPC). The xGPC executed commands in Python (v3.7, https://www.python.org/) using the PyTorch library (v1.4; https://pytorch.org/). Near realtime performance was guaranteed in the

following fashion. The xPC transmitted data to the xGPC with a timestamp, the xGPC calculated updates for the virtual fingers from the inputs and transmitted the data back to the xPC along with the original timestamp. When the xPC received the data packet, the packet was logged with a new timestamp. Real-time performance was guaranteed given that the time stamp received from xGPC (the original timestamp sent by xPC) was within 50 ms of the current xPC timestamp and updates to the virtual fingers occurred every 50 ms.

2.3.5 ReFIT Kalman Filter

The ReFIT kalman filter was implemented for use with fingers as described by Vaskov et al. and Nason et al. (Vaskov et al., 2018; Nason et al., 2019). In summary, it is a two-step process that involves first training a Kalman filter using spike-band power measurements from any 96 channels of the Utah array to predict updates to position and velocity states of the virtual fingers. A detailed description on the Kalman filter implementation is described by Vaskov et al. (Vaskov et al., 2018). Optimal lag is commonly implemented in Kalman filter motor decoders (Wu et al., 2004) to account for the physiologic lag between cortical activity and motor movement (Moran and Schwartz, 1999). Thus an optimal time lag, calculated to be one 50-ms bin, was applied when training and implementing the Kalman filter as detailed in previous work(Irwin et al., 2017; Vaskov et al., 2018). The trained Kalman filter was then used to perform closed-loop motor decoding. To train the RFKF, the velocities predicted in the preceding real-time decoding session were modified by multiplying velocities by -1 when the velocity was oriented in the opposite direction as the target. The Kalman filter was then retrained using these new velocity values as described by Vaskov and colleagues to obtain the ReFIT Kalman filter

(Vaskov et al., 2018). As also detailed in (Vaskov et al., 2018), Kalman gain was implemented with no position uncertainty.

When implementing the Kalman filter for offline analyses, the classic Kalman filter as described by Wu et al. was used (Wu et al., 2004). The Kalman filter used in online decoding described by Vaskov et al. and Irwin et al. imposed physical constraints on the relationship between position and velocity thought to be helpful in real-time decoding (Irwin et al., 2017; Vaskov et al., 2018). These constraints are not imposed on the offline Kalman filter as it may lower the correlation in offline analyses.

2.3.6 Neural Network Velocity Decoder

The neural network velocity decoder was designed from preliminary offline experiments that explored various network architectures. The final network is given in Fig. 1C. The first layer was the time feature layer that constructs time features from 150 ms (three 50-ms bins) from the 62 input electrodes. This layer was implemented in Pytorch, using the *torch.nn.Conv1d* module, i.e. as a one-dimensional convolution with a kernel size of 1 (H=W=1) and 3 input channels (neural network channels, not electrode channels). Each channel corresponded to one 50-ms time bin. Although possible to construct a spatial convolution across electrodes, this was not performed because the spacing between electrodes was distant relative to the size of the neurons being recorded. The output of the time feature layer provided 16 features per electrode and, when flattened, provided 1536 inputs to a series of fully connected layers. Regularization for fully-connected layers 1-3 included 50% dropout and batch normalization. Fully-connected layer 1 converted the 1536 inputs to 256, and the remaining layers had 256 hidden neurons. The sequence of the modules used was *torch.nn.linear*, *torch.nn.Dropout*, *torch.nn.BatchNorm1d*,

and then finally *torch.nn.functional.relu*. The final layer implemented a matrix multiplication with *torch.nn.linear* to convert the 256 inputs to the two velocity estimates. The output of the network was normalized to zero mean and unit variance and roughly twenty times the magnitude of actual velocity peaks. This normalization was discovered to converge more quickly when training the NN then training without the normalization. The output of the neural network was scaled by an unlearned gain factor that equaled the average magnitude peaks of the actual velocity divided by the average magnitude peaks of the predicted velocity. No offset was applied to the final predicted velocity leaving it a zero-mean signal. A diagram of the final neural network is given in Fig. 1C.

Prior to training the neural network, a training data set was collected in hand-control mode for roughly 400 trials with randomly appearing targets. A subsequent 100 trials were also performed and served as a validation set to ensure the network had converged. This validation set was also used to calculate the gain as described above. If there was a non-zero median, this was subtracted as well to approximate a zero-mean signal. The SBP and velocity data was assembled into data structures in Matlab (Mathworks, Natick). No optimal lag was included as the appropriate time history weighting was learned during the training process. The data was randomized in two ways. First, the time data was randomized into batches of 64 time points (and their 2 associated time delays). Second, a triangular distribution of velocities was imposed on the training data spanning the range of -4σ to 4σ where σ was the standard deviation of the actual velocity. A total of 20,000 training samples were randomly chosen to achieve this velocity distribution. In preliminary experiments, this velocity redistribution was observed to improve performance on the finger task when the neural network was trained on a center-out finger task. This redistribution of velocities was also used when training on random finger targets so that the

decoder could easily be generalized to other training paradigms in the future. There was no difference in online neural network decoding between redistributed and non-redistributed velocity when the network was trained on random fingers.

In addition to the neural network used for online testing, several other neural networks were used to understand how individual components of the neural network affected offline performance. The networks included a network of only two layers and no regularization (no batch normalization, dropout, or output normalization). The other networks included regularization and parameters in a similar manner as Fig. 1C. These included a 2-layer fully connected network (256 hidden neurons) with a preceding time feature layer (3 input channels for each electrode and 16 output channels) and 4-layer fully-connected network (256 neurons) with a time feature layer. The offline networks were compared with the classic Kalman filter (without the retraining intention step) and ridge linear regression with a regularization constant of $\lambda = 10^{-3}$.

When training the network for online decoding, the neural network was optimized over 3500 iterations using the Adam optimization algorithm (Kingma and Ba, 2014) with a learning rate of 10^{-4}, weight decay of 10^{-2}, and momentum of 0.9. When generating weights for offline analysis, a learning weight of $2x10^{-5}$. Kaiming initialization was used to initialize the weights of each layer (He et al., 2015), and the bias terms were initialized to zero. The dropout level used was 50% (Srivastava et al., 2014). On each day, a training set (~400 trials) and testing set (~100 trials) were collected, and performance on a testing set was characterized by the correlation of predicted and actual velocity. The number of iterations were determined for each network from the first of three offline testing days and chosen so that the correlation between actual and

estimated velocity (on the testing set) did not significantly change with additional training iterations (changes in correlation with additional iterations on the order of ~0.01).

When searching for the preferred number of layers, hidden neurons, and output time features (Fig. 4A-B), performance was characterized by the average of the maximum of 5 correlations with the testing set over all training iterations. This reduces the variability of the correlation for each combination of layers, hidden neurons, and output time features.

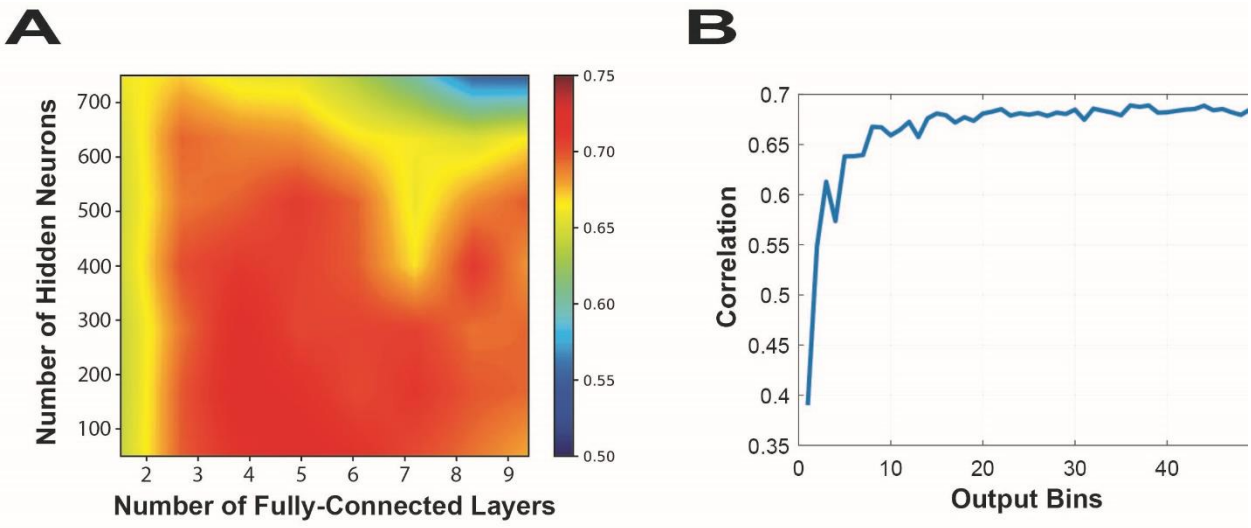

Figure 2-4. Preferred Training Parameters
(A) Heat map illustrating the offline correlation between the number of fully-connect layers versus the number of hidden neurons. The correlation values were calculated as the average of the five-best correlation during the training of the network. The networks used during online testing had 4 layers and 256 neurons. (B) The correlation during offline training as a function of the number of learned time features in the output from the time-history layer of Fig. 1C. The number of output features selected in online testing was 16.

2.3.7 Online Training/Testing Protocol

Targets for the fingers were not allowed to be separated by greater than 50% of the range. During training, the random targets spanned 100% of the finger flexion/extension range, but

during online decoding only 95% of the range was used. The classic Kalman filter was then used on a ~250 trial run from which the ReFIT KF coefficients were calculated.

2.3.8 Performance Assessment

Performance in online mode was characterized with Fitt's law bit rate given below in Eq. (2.3), which accounts for both task difficulty and the time needed for completion. The variable D_k is the position of the k-th virtual finger at the start of the task, T_k is the target position for the k-th virtual finger, S is the target size (equal in both fingers), and t_{acq} is the time to reach the target.

$$Bit\ Rate\ = \frac{log_2\left(1 + \frac{\sqrt{(D_1 - T_1)^2 + (D_2 - T_2)^2} - S/2}{S}\right)}{t_{acq}}$$

Equation 2-1

While bit rate was the primary performance metric, acquisition times were also reported.

All velocities in the offline analyses were normalized by the standard deviation of the true velocity with 1 indicating the equivalent of 1 standard deviation of the actual velocity. The time plots depicting the actual versus predicted velocity were selected from one of the training days to illustrate the results (Fig. 2-3A). The correlation for each decoder was averaged over 2 fingers on 3 days (Fig. 2-3B). The plots of true versus predicted velocity were calculated by binning the magnitude of the actual velocity into bins of size 1.0 at intervals of 0.5 and averaging the magnitude of the predicted velocity in each respective bin. The linear regression analysis utilized the *fitlm.m* subroutine in Matlab to evaluate the correlation between true and predicted velocity at low (<1.33) and high velocity (>1.33).

2.3.9 Statistical Analysis

Comparing the performance metrics between groups was made with a paired t-test. Evaluating the linear relationship between predicted and actual velocity was made with using the Matlab built in function *fitlm.m*.

Chapter 3. Distinct Perceptive Pathways Selected with Tonic and Bursting Patterns of Thalamic Stimulation

A version of this work was submitted for publication.

3.1 Abstract

Background: Novel patterns of electrical stimulation of the brain and spinal cord hold tremendous promise to improve neuromodulation therapies for diverse disorders, including tremor and pain. To date, there are few experimental studies in human subjects to help explain how stimulation patterns impact the clinical response.

Objective/Hypothesis: We propose using novel stimulation patterns during electrical stimulation of somatosensory thalamus in awake deep brain stimulation surgeries and hypothesize that stimulation patterns will influence the sensory percept without moving the electrode.

Methods: In this study of 15 fully awake patients, the threshold of perception as well as perceptual characteristics were compared for tonic (trains of regularly-repeated pulses) and bursting stimulation patterns.

Results: In a majority of subjects, tonic and burst percepts were located in separate, non-overlapping body regions (i.e., face vs. hand) without moving the stimulating electrode ($p < 0.001$). The qualitative features of burst percepts also consistently differed from those of tonic-evoked percepts as burst patterns were less likely to evoke percepts described as tingling ($p=0.013$, Fisher's exact test).

Conclusions: Because somatosensory thalamus is somatotopically organized, percept location can be related to anatomic thalamocortical pathways. Thus, stimulation pattern may provide a

mechanism to select for different thalamocortical pathways. This added control could lead to improvements in neuromodulation - such as improved efficacy and side effect attenuation - and may also improve localization for sensory prostheses.

3.2 Introduction

Novel bursting patterns of electrical stimulation have demonstrated more effective pain relief in spinal cord stimulation and greater motor improvement during deep brain stimulation (DBS) for movement disorders than traditional tonic stimulation patterns (trains with regularly repeated pulses) (Heming et al., 2011; Brocker et al., 2013; Adamchic et al., 2014; Cagnan et al., 2016; Brocker et al., 2017; Deer et al., 2018). DBS for movement disorders applies a tonic pattern with a frequency of 130 to 180 Hz, which has been found to best reduce symptoms for the average patient. Initial studies exploring temporally irregular (non-tonic) patterns failed to outperform tonic designs (Montgomery and Baker, 2000; Montgomery Jr, 2005; Dorval et al., 2010; Birdno et al., 2011; Swan et al., 2016). However, recent work has shown that temporally irregular patterns reduce tremor, bradykinesia, and power consumption as well as avoid thalamic adaptation (Heming et al., 2011; Brocker et al., 2013; Adamchic et al., 2014; Cagnan et al., 2016; Brocker et al., 2017). Methods to generate these patterns include use of models to generate patterns with the optimal trade-off between beneficial features (e.g. low power) and unwanted symptoms (e.g. tremor) (Brocker et al., 2013; Brocker et al., 2017; Grill, 2018). Additionally, others have shown that motor movement can be improved if bursts of pulses are coordinated across spatial macro-contacts (coordinated reset) or bursts are optimally timed to occur at specific time points of a patient's tremor (Heming et al., 2011; Brocker et al., 2013; Adamchic et al., 2014; Brocker et al., 2017). Finally, cycled patterns have been shown to better resist thalamic

adaptation than traditional tonic patterns (Heming et al., 2011). Since previous modeling work suggests that pauses in DBS stimulation may permit brief pathological activity (Birdno et al., 2011; Swan et al., 2016), additional experimental insights are greatly needed to help explain how bursting stimulation improves symptoms.

In this work, we explore tonic and bursting stimulation patterns in human somatosensory thalamus (ventral caudal nucleus; Vc), which is highly amenable to intraoperative study (Tasker et al., 1982; Dostrovsky et al., 1993; Chien et al., 2017). As opposed to the terminal effects of other DBS targets that can be challenging to quantify and measure in an intraoperative setting, the terminal effects of Vc stimulation are sensations, called percepts, that can be easily reported. All tactile information from the face and body converge in this compact structure before being relayed to the cortex, and Vc is somatotopically organized with face and upper-body relay neurons located medially and lower-body relay neurons located laterally, although individual variability can exist (Mountcastle and Henneman, 1952; Schmid et al., 2016; Chien et al., 2017). Thus, percept locations can be related to anatomic pathways via this somatotopy, and neurosurgeons routinely rely on this relationship for intraoperative localization (Starr et al., 2009; Gross and Boulis, 2018). While the percept quality from Vc stimulation has been well-studied (Tasker et al., 1982; Heming et al., 2010; Swan et al., 2017), we aim to compare percept locations during electrical stimulation with bursting and tonic patterns to provide insight into the underlying anatomic pathways and networks involved.

3.3 Materials and Methods

3.3.1 Study design

Our study included 15 consecutive subjects undergoing awake DBS placement in the ventral intermediate nucleus of the thalamus (VIM) for essential tremor during a 17-month period who were able to complete awake intraoperative testing. Three subjects had previously undergone VIM DBS on the contralateral side. Two patients were excluded from analysis due to suboptimal initial lead placement with inability to complete intraoperative experiments. The remaining 15 subjects included 13 males and 2 females, with ages ranging 37-82 years and a mean age of 67 years. The predominance of men is consistent with the known prevalence of essential tremor (Louis and Ferreira, 2010). The study was approved by the Institutional Review Board of the University of Michigan. All participants signed written informed consent.

Twenty-seven anatomical sites, i.e. locations in the brain where macrostimulation was performed, were included if the location was estimated to be in sensory thalamus and subjects were able to feel sensations from thalamic stimulation. No sites were discarded (although one site could not be included because of audio recording failure) and research testing was stopped when intraoperative constraints dictated that we resume the clinical procedure. The subjects were blinded to stimulation patterns.

3.3.2 Stimulation apparatus

Stimulation was performed using an intraoperative neural targeting system, as previously described (Patil and Dodani, 2018), schematically illustrated in Figure 1a. LabVIEW software (National Instruments, Austin, TX) was programmed on a Dell T5500 computer (Dell Inc., Round Rock, TX) and interfaced with a commercial intraoperative electrophysiology system

(Neuro Omega™, Alpha Omega, Nazareth, Israel). Stimulation pattern, stimulation amplitude, and stimulation microelectrodes were selected with the custom LabVIEW software, which was interfaced with the Neuro Omega via the Alpha Omega Software Development Kit. Stimulation was applied through Neuroprobe microelectrodes (STR-009080-10, Alpha Omega), with a macro-contact length of 1 mm, diameter of 0.56 mm, and 250–1250 kΩ impedance at 1 kHz(Marmor et al., 2017).

3.3.3 Stimulation parameters

Stimulation patterns were created offline in MATLAB (MathWorks, Natick, MA) and loaded into the LabVIEW software. The pulse shape for all stimulation patterns were identical (Figure 1b) and consisted of a one period, 400-µs sine wave with a 200-µs positive phase immediately followed by a 200-µs negative phase to maintain charge balance (McIntyre and Grill, 2000). The sinusoidal pulse shape was selected to obviate the need for sharp on/off transitions and to minimize distortion in the frequency domain. Pulse width was selected to remain within 30µC/cm^2 per phase charge density safety limits (McIntyre and Grill, 2000; Cagnan et al., 2016), while recruiting a maximal volume of thalamocortical neurons. The pulse rate for tonic stimulation was 80 Hz that is similar to the 60-Hz stimulation frequency used in many earlier studies to map Vc (Tasker et al., 1972) but increased slightly to avoid 60-Hz noise.

Parameters for bursting stimulation include intraburst pulse rate, burst duration, and burst repetition interval. For consistency, we used an intraburst pulse rate of 80 Hz, equal to that of tonic stimulation. Burst duration and burst repetition intervals were empirically determined in Subject 1. Burst durations of around 62.5 ms and rest duration of 125 ms were perceived by Patient 1 as qualitatively different from the other combinations of burst/rest durations. For the

remaining 14 patients we continued to use this bursting pattern with a burst of 5 pulses repeated every 187.5 ms (Fig. 1b, bottom) given that the percepts were consistently distinct from tonic patterns.

In a subset of 5 patients, low-frequency tonic patterns were created with the same stimulation amplitude and average number of pulses as the bursting patterns above. These patterns were similar to the tonic pattern in Fig. 1b except with a frequency of 27 Hz. In the final patient, a 30-Hz tonic pattern was compared with an 80Hz-bursting pattern of 60 ms duration and repetition interval of 100 ms.

The 80-Hz tonic and bursting patterns were compared at the threshold of perception—the minimum amplitude needed to perceive electrical stimulation. Amplitudes greater than this have been shown to produce a significantly diminished perception of naturalness (Swan et al., 2017). The amplitude used for the low-frequency tonic pattern was equal to the threshold of perception of the bursting pattern so that a charge-matched comparison could be made.

3.3.4 Thalamic localization

Preoperative 3T cranial magnetic resonance imaging (MRI) of all patients was obtained before DBS lead placement and co-registered to MR imaging obtained on the day of surgery after Leksell stereotactic frame (Elekta AB, Stockholm, Sweden) placement. Computed tomography (CT) imaging was substituted for 3 patients with existing DBS systems, which are incompatible with 3T MRI. Images were co-registered using commercial software (Analyze, AnalyzeDirect, Inc., Overland Park, KS) and uploaded into commercial frame-based targeting software (Framelink, Medtronic, Minneapolis, MN).

Atlas-based VIM targeting was performed. The initial ventrocaudal VIM target was assigned as 11.5 mm lateral to the wall of the third ventricle and 5 mm anterior to the posterior commissure in the intercommissural plane. A cranial entry point was selected at the coronal suture, approximately 2.5 cm lateral to midline. The entry point to VIM target defined the "VIM trajectory" (Fig. 1c).

To verify hand localization within VIM, a second "Vc trajectory" was assigned parallel and 2 mm posterior to the VIM trajectory. The point of transition from the VIM to the Vc nucleus along the Vc trajectory was estimated using the Schaltenbrand-Wahren atlas built into the Framelink software (Schaltenbrand and Wahren, 1977). Typically, the last 3 mm of the posterior trajectory localized to Vc (Fig. 1c). For notational purposes, all depths are reported relative to target depth: a depth of 3 mm is 3 mm above target and a depth of -3 mm is 3 mm below target depth (Fig. 1c).

A

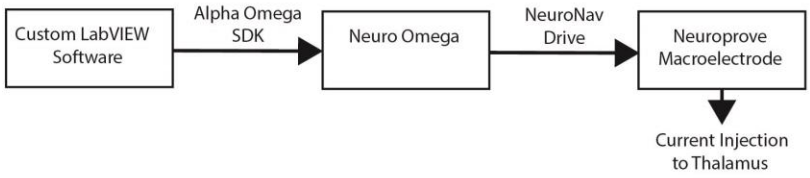

B

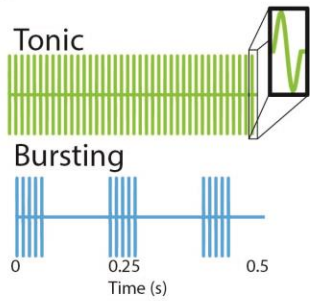

C

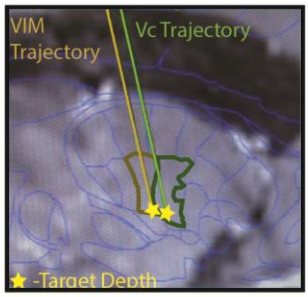

D

Patient Prompts	
Mechanical	Touch, Pressure, Sharp
Movement	Vibration, Movement
Temperature	Warm or Cool
Tingle	Electrical Current, Tickle, Itch, Tingling

Figure 3-1. **System and experimental setup.**
(**a**) Customized LabVIEW software inputs into Neuro Omega that drives macroelectrode to provide electrical stimulation to brain tissue. (**b**) Depiction of 0.5-s segment of tonic (green) and bursting (blue) patterns. All pulses are identical and pictured to scale in the cutout window. (**c**) Preoperative MRI as shown on StealthStation during preoperative planning. The yellow line is the planned ventral intermediate nucleus of the thalamus (VIM) trajectory that ends in the star. The star is the estimated final position of the to-be-implanted permanent deep-brain stimulation lead. The green trajectory represents a parallel trajectory 2 mm posterior to the VIM trajectory that passes through the somatosensory nucleus of the thalamus (Vc). The star at the tip of this trajectory signifies the same depth on this trajectory as the star on the VIM trajectory. (**d**) Table shown to subjects prior to the experiment to provide a list of potential responses. Patients were verbally counselled that they could choose words not on this list.

3.3.5 Testing protocol

During the operative procedure, the stimulating microelectrodes were advanced through VIM and Vc. Patient responses to stimulation and stimulation parameters were recorded simultaneously using a high-definition video camera and a wireless microphone. Patients were blinded to stimulation pattern. Tonic stimulation through the macro-contact on the microelectrode was utilized to verify VIM localization and somatotopy, according to standard operative practices. Sites were excluded from the analysis if no percept was elicited by either tonic or burst stimulation or if the reported tonic percept was non-physiological (e.g. bilateral headache, ipsilateral percepts). One site could not be included in the analysis because of audio recording failure. In total, twenty-seven sites within Vc were analyzed. The number of test sites for each subject was limited by the available time for testing. The subjects were blinded to stimulation patterns.

The first objective in testing a stimulation pattern was to determine the threshold amplitude of perception. To prevent thalamic adaptation, the initial amplitude was set to either 0.1 or 0.2 mA and incrementally increased until a percept was reported. To minimize thalamic adaptation (McIntyre and Grill, 2000), stimulation was limited to either 4 s or the minimum time needed for a subject to report a percept. If the initial stimulation amplitude was perceived,

stimulation was immediately halted and the amplitude was lowered to the threshold of stimulation.

The amplitude at the threshold of perception for tonic and bursting patterns were recorded. Additionally, the charge was recorded at the threshold of perception for tonic and bursting patterns. As the patterns were charge balanced, we assigned the charge per pulse as the area under a half sine wave period multiplied by the threshold of perception. The total charge per second reported as the charge per pulse multiplied by the average number of pulses per second. At each site in the first 6 subjects, subjects were asked if the stimulation was perceived ("Do you feel anything now?"). Patients usually proceeded to describe where the percept was located and the sensory quality. If the subject did not report location and quality, the experimenter would ask for location ("Where do you feel it?") and quality ("What does it feel like?"). During the first few trials, subjects were shown the table in Figure 1d as a list of potential responses, which is a slight modification of the table used to assess sensory quality by Ohara and colleagues (Ohara et al., 2004). When time allowed, and simulation pattern differences produced percepts at different locations or with different qualities, stimulation patterns were either alternated or randomly varied. Stimulation lineups, when varied at a given site, are reported in the Results section.

3.3.6 Statistical analysis

To evaluate the hypothesis that bursting patterns were less likely to "tingle" than tonic counterparts, we used Fisher's exact test to compare the number of non-tingling sites between tonic and burst percepts in the 27 sites of macrostimulation. Statistical significance for the amplitude values between tonic and bursting patterns at the perception threshold was determined with a 2-sided, 2-sample t-test. Statistical significance for the amplitude values between sites

with similar burst vs tonic percepts and different burst vs tonic percepts was also compared with a 2-sided, 2-sample t-test. Statistical significance to compare the depth of stimulation sites was performed with a 2-sided, 2-sample t-test. The relationship between burst/tonic percept locations and whether the final implanted lead required adjustments was evaluated with a fisher's exact test. Statistical significance of stimulation trials comparing the location of low-frequency tonic and bursting percepts evaluated whether low-frequency tonic percepts avoided activation of percepts in the location of high-frequency tonic percepts and activated percepts in the same location of burst percepts. For the evaluation of this statistical significance, a Fisher's exact test was used. A statistical significance level of 0.05 was used.

3.4 Results

Our analysis includes fully awake and unanesthetized patients who underwent stimulation of the somatosensory (Vc) thalamus during DBS surgery for essential tremor. For each patient, stimulation with tonic and bursting patterns were tested within Vc. Testing was performed at a total of 27 sites in 15 patients. The amplitude of stimulation was set to the threshold of perception, which is the lowest amplitude at which subjects reported a percept.

3.4.1 Stimulation pattern controls percept location

While 14/27 sites of stimulation had similar location percepts for both bursting and tonic waveforms, in 13/27 sites (in 8/15 subjects tested), 80 Hz tonic and bursting percepts (in Fig. 1B) were perceived in distinct, non-overlapping locations, specifically hand versus face. Figure 2a graphically illustrates typical results for the first 6 subjects, and a table of results for all subjects is shown in Figure 2b. Tonic percepts arose in the hand/arm in a majority of sites (19/27) as

expected since the hand region of VIM is targeted for DBS. Tonic percepts localized to the face/head in 6 sites, and arose in both hand and face regions at 2 sites. Bursting percepts occurred in the head/face region in 17/27 sites, occurred in the hand/arm in 7 sites and arose in both areas at 3 sites. Even among stimulation sites where tonic and burst percepts were located in close proximity, small differences in location often existed, e.g. cheek versus lip in Subject 2 and $2^{nd}/3^{rd}$ fingers versus thumb in Subject 10.

Percept size and location were assessed through detailed, recorded subject descriptions. Spontaneous patient terminology was clearly non-overlapping. Patients 4, 6 and 10-14 all reported tonic percepts in the hand (e.g., “thumb” or “fingers”), whereas bursting percepts were in the face (e.g., “jaw,” “neck,” “lip,” “side of [the] face,” and “mouth [or] throat”). Tonic percepts were located in the face for Patients 1 and 3 (mouth, tongue, lips or cheek) with bursting percepts in the fingers and arm. Patient 1, with bursting percepts in the fingers, denied any facial component. Patients uniformly denied overlap between tonic and bursting percepts when asked explicitly. Patients 4, 6, 10, 11, and 14 denied bursting percepts located in the hand, where tonic percepts were located. Patients 10 and 14 also denied tonic percepts where bursting percepts arose. Finally, and similar to macrostimulation results from Heming and colleagues (Heming et al., 2010), percepts for each pattern were mostly of “medium” size since they typically covered parts of limbs or multiple fingers, although more focal percepts were also reported.

Percept location as a function of tonic versus bursting stimulation pattern remained stable even when stimulation patterns were repeated or alternated (Fig 2c). Stimulation trials were repeated in all 8 subjects where bursting and tonic percept locations differed, and 31/32 stimulation trials remained stable with hand percepts remaining in the hand and face percepts

remaining in the face. Additionally, in 4 subjects (5 sites), tonic and burst patterns were alternated a total of 15 times, and the location remained stable.

A

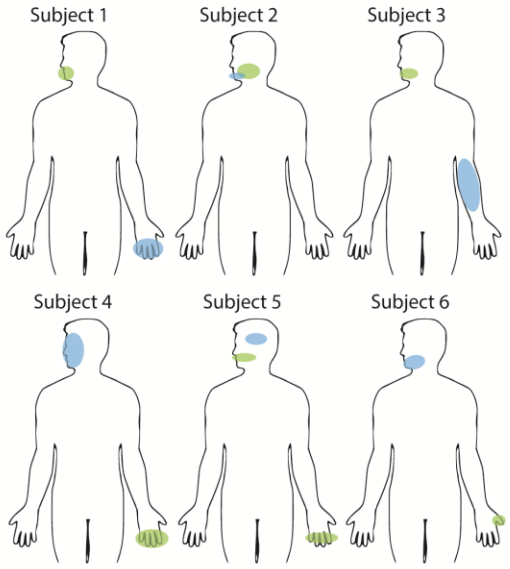

B

Pt.	Depth (mm)	Location		Res. - Imp. Lead (mm)
		Tonic	Bursting	
1	3.0	mouth, tongue, lips	fingers	(0,-2, 0)
2	3.0	cheek	bottom lip	(0,-2, 0)
3	2.5	lip and cheek	lip, cheek	(0,-2, 0)
	2.0	lip	arm	(0,-2, 0)
4	3.6	hand	face	(0,-2, 0)
	2.6	fingers	face	(0,-2, 0)
	1.6	hand	face	(0,-2, 0)
	0.6	fingers	hand	(0,-2, 0)
	-0.4	hand	face	(0,-2, 0)
5	3.0	teeth, hands	middle of head	**(-2,-2, 0)***
	1.5	teeth, hands	face	(0,-2, 0)
	0.0	fingertips	mouth and hand	(0,-2, 0)
6	1.0	thumb	jaw	(0,-2, 0)
	-0.1	thumb	face, head	(0,-2, 0)
7	0.0	mouth	mouth	**(-2, 0, 0)**
8	-0.7	fingers to wrist	palm, wrist	**(-2,-2, 0)**
	-1.7	fingers to wrist	hand	**(-2,-2, 0)**
9	1.0	side of head	jaw	**(+2,-2, 0)****
	0.0	side of face	face	**(+2,-2, 0)****
10	2.0	2nd, 3rd digits but not thumb	thumb	(0,-2, 0)
	0.0	hand	face	(0,-2, 0)
11	2.0	3rd, 4th fingers	face	**(-2,-2, 0)**
12	3.5	fingers	lip	**(+4,-2, 0)**
13	3.0	hand	jaw	**(-2,-2, 0)**
14	-0.2	fingers, wrist	mouth	**(+2,-3, 0)**
	3.0	fingers	hand, face	**(+2,-3, 0)**
15	0.0	arm	hand, arm	**(0,-4, 0)**

C

Trial #	Pattern	Percept Location
1	Tonic 80 Hz	thumb
2	Tonic 80 Hz	thumb
3	Burst	jaw
4	Burst	jaw
5	Tonic 80 Hz	thumb
6	Burst	jaw

Figure 3-2. Stimulation pattern controls percept location.
(**a**) A body map for the first six subjects that represents the disparate percepts between tonic (green) and bursting (blue) stimulation. (**b**) Table shows percept location for tonic and burst stimuli at each site tested. Sites where percept locations are widely disparate are highlighted in yellow. Research minus implanted lead (Res. – Imp. Lead) denotes the position of the research lead subtracted by the final implanted lead position. Without any adjustments to the final lead, the research lead would be 2 mm behind the implanted lead, i.e. (0, -2, 0) mm. Testing sites that differed from this planned relationship are denoted in bold font. A positive value for $\Delta x > 0$ indicates a research lead position lateral to the implanted lead position. The * denotes that the lead surgeon (P.G.P.) asked to move to a more lateral trajectory given the head percepts. The ** denotes that testing was performed on a trajectory 2 mm lateral to the intended trajectory because no percepts occurred at the original trajectory (**c**) Table displays an illustrative example site for subject 6 where stimulations were randomized at a single site and stable difference in the location of tonic and burst percepts.

3.4.2 Percept locations affected by the temporal distribution of pulses

Bursting and 80 Hz tonic patterns have three important differences: the temporal distribution of pulses, the average number of pulses in time, and the amplitude at the threshold of perception. To determine whether percept location differences were caused by the temporal distribution of pulses (and not one of the other differences between bursting and tonic patterns), we created low-frequency (27 or 30 Hz) controls with the same number of pulses and amplitude as the bursting patterns. These patterns differed only in the temporal distribution of pulses. These patterns were compared in 6 sites (in 5 subjects) where bursting produced percepts in the face and 80-Hz-tonic produced percepts in the hand. As illustrated in Fig 3a-b, the percepts (blue data points) were located in the head at all 6 sites. However, low frequency tonic patterns (magenta data points) produced percepts in the hand – like 80-Hz tonic patterns – at 4/6 sites. However, at sites 3 and 6, the percept location was not stable and occasionally generated face percepts like the bursting patterns. This instability led to the proportion of head or face percepts being less than 1. For completeness, Fig. 3c depicts the number of stimulation trials conducted for each stimulation pattern at each site. Across all trials, low-frequency percepts were statistically different ($p < 0.001$; Fisher's exact test) than bursting patterns and produced hand percepts in 12 trials (like 80-Hz tonic), head percepts in 10 trials (like bursting), and percepts in both head and hand in 1 trial (see Fig. 3a-c).

As an illustrative example in Subject 3, bursting and 27-Hz-tonic stimulation patterns were compared at a constant amplitude of 1.2 mA (Fig. 3d-e). The 27-Hz tonic waveform produced hand percepts (similar to the 0.5 mA, 80-Hz tonic percepts), while the bursting stimulation produced percepts in the jaw/neck region. Six trials randomly alternating between

27-Hz tonic and bursting patterns in Fig. 3b demonstrated stable, non-overlapping percepts in all 6 attempts. Thus, the irregular distribution of pulses, independent of amplitude and number of pulses, led to differences in percept location.

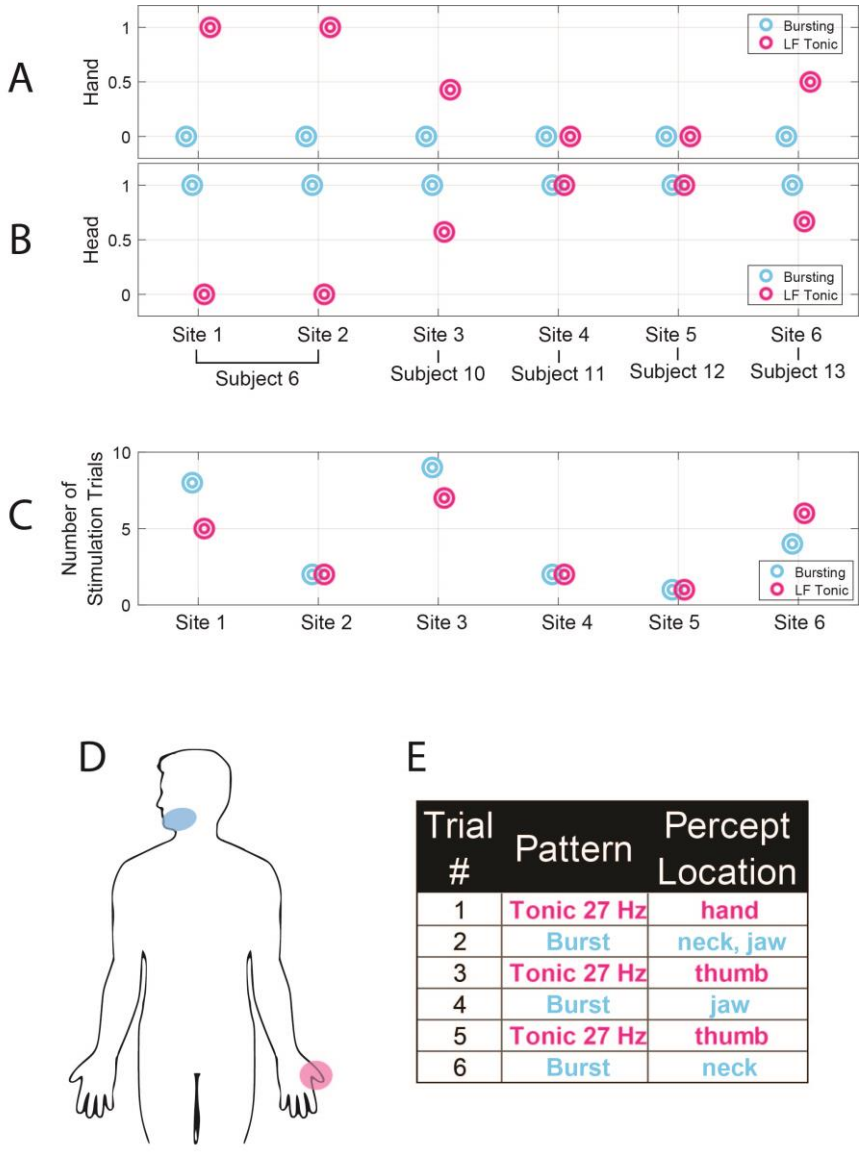

Trial #	Pattern	Percept Location
1	Tonic 27 Hz	hand
2	Burst	neck, jaw
3	Tonic 27 Hz	thumb
4	Burst	jaw
5	Tonic 27 Hz	thumb
6	Burst	neck

Figure 3-3. **Controlled experiment of percept location using tonic and burst stimuli in five subjects.**
Six sites showing the proportion of low-frequency tonic (magenta) and bursting (blue) patterns that generated percepts in the head (**a**) and in the hand (**b**). LF denotes low frequency tonic patterns. (**c**) Number of stimulation trials at each site for low-frequency tonic (magenta) and bursting (blue) patterns. (**d**) A body map for Subject 6 illustrates overlapping and focal percepts for 80-Hz tonic (green) and low-frequency, 27-Hz tonic (magenta) stimuli compared to an anatomically distant bursting percept in the face (blue). (**e**) For the same site as (**d**), Table reports

randomized stimulation trials showing the difference in low-frequency tonic and bursting patterns that are controlled for amplitude and number of spikes.

3.4.3 Differences in amplitude, charge, and site location

The perception threshold was lower for high-frequency tonic patterns compared to bursting patterns at all sites ($p < 0.001$; t-test). The perception threshold was 0.50 ± 0.09 mA for tonic patterns and 1.17 ± 0.11 mA for bursting patterns. In the subset of sites where tonic and burst percepts were nearby, the mean amplitude of tonic patterns, 0.64 ± 0.14 mA, was lower than the mean amplitude of burst patterns, 1.34 ± 0.13 mA ($p < 0.001$; t-test). In the subset of sites where tonic and burst percepts were located in disparate body areas, the mean amplitude of tonic patterns, 0.33 ± 0.07 mA, was lower than the mean amplitude of burst patterns, 0.97 ± 0.18 mA ($p < 0.001$; t-test) as shown in Fig. 4a, left pane.

To understand whether perception thresholds differed between sites with nearby versus disparate tonic and burst percepts, the perception thresholds were compared, see Fig. 3b, middle pane. Combining the amplitude at perception for both stimulation patterns revealed decreased amplitudes at sites with disparate tonic versus burst percepts relative to sites with similarly located percepts ($p = 0.037$; t-test).

The mean charge injected between tonic and bursting patterns, however, was not statistically different at all sites ($p = 0.26$; t-test), sites with similarly located percepts ($p = 0.19$; t-test), or sites with disparately located percepts ($p = 0.995$; t-test). The mean charge injected for the tonic pattern at threshold was 4.7 ± 0.8 μC/s for all sites, 6.0 ± 1.4 μC/s at sites with percepts near burst percepts, and 3.0 ± 0.7 μC/s at sites with percepts disparate from burst percepts. The mean charge injected for the bursting pattern at threshold was 3.7 ± 0.3 μC/s for all sites, $4.2 \pm$

0.4 µC/s at sites with percepts near tonic percepts, and 3.0 ± 0.6 µC/s at sites with percepts disparate from tonic percepts (Fig. 4c, right pane).

Similarly, there were no statistically-significant differences in depth between sites with tonic and burst percepts located nearby and in disparate locations (p = 0.46; t-test). The mean depth when percepts were similarly located was 1.0 ± 0.4 mm. A positive value indicates the distance superficial to target (described in Section 2). The mean depth when percepts were disparate was 1.5 ± 0.5 mm. There were also no statistically significant differences among the number of sites with similarly located versus disparately located percepts that required adjustment of the final lead position (p = 0.45; Fisher's exact test).

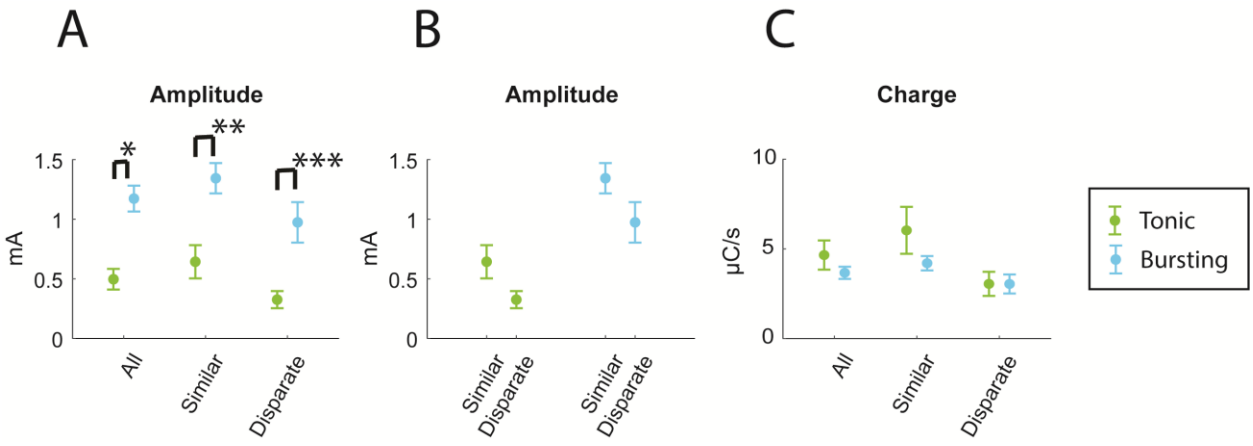

Figure 3-4. Differences in amplitude and charge at the perception threshold. Amplitude differences in (**a**) demonstrate differences in tonic (green) and bursting (blue) amplitudes (in mA) at all sites, at sites where percept locations are similar, and at sites where percept locations are in disparate body regions. The asterisks represent statistical significance. Regrouping the tonic and bursting amplitudes together in (**b**) highlights the differences in similar and disparate sites. In (**c**), the different charge injected at the threshold of perception at all sites, those with similarly located percepts, and those with disparate percepts

3.4.4 Less tingling from bursting stimulation

For completeness, in the first 6 subjects, we asked subjects to describe the quality of percepts. This was not continued in the remaining 9 subjects due to intraoperative time

constraints. Bursting percepts were less often described by subjects as “tingling” than tonic percepts ($p = 0.013$; Fisher’s exact test). At the 8 of 14 sites where percept quality differed, tonic percepts were tingling in all cases, whereas bursting percepts were sometimes non-tingling. In particular, bursting patterns produced non-tingling percepts in 9/14 sites and in 5/6 subjects tested. On the other hand, tonic percepts were tingling in all but one site (see Fig. 5a). Bursting stimulation elicited a variety of non-tingling qualities, including pressure, sharpness, vertigo, and vibration, as depicted in Figure 5b. Of note, in Subject 5, bursting percepts were similar to pressure, but on repeated stimulation the subject reported either pressure or tingling. Figure 5c illustrates an example where bursting and tonic patterns were randomly alternated to give non-tingling bursting percepts and tingling tonic percepts.

A

Pt.	Depth (mm)	Percept Quality	
		Tonic	Bursting
1	3.0	tingling	sharp
2	3.0	pressure	pulsed pressure
3	2.5	tingling	vibration
	2.0	tingling	shaking
4	3.6	tingling	vertigo
	2.6	tingling	vertigo
	1.6	tingling	vertigo
	0.6	tingling	tingling
	-0.4	tingling	vertigo
5	3.0	tingling	electric current
	1.5*	tingling	pressure
	0.0*	pins/needles	electric current
6	1.0	tingling	tingling
	-0.1	electric curent	tingling

*Lead moved 2 mm lateral

B

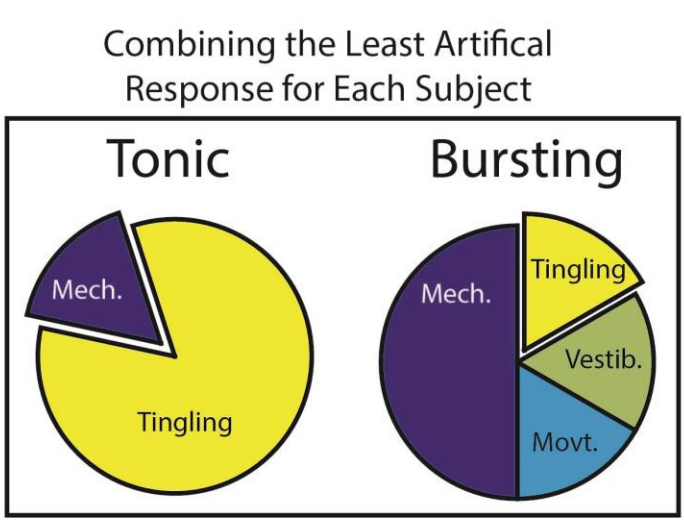

C

Patient 3

Trial #	Pattern	Percept Location
1	burst	vibration
2	tonic	tingling
3	burst	vibration
4	burst	vibration
5	tonic	tingling
6	tonic	tingling

Figure 3-5. **Tonic and burst stimuli affect percept quality.**
(**a**) The table lists percept quality evoked at all of the sites tested. The sites producing sensations of tingling, pins/needles, or electric current are highlighted in red. (**b**) Two pie charts representing the sensation quality for the least artificial percept quality in each subject. Specifically, 1/6 of the pie is assigned to each subject. If a non-tingling percept is produced by electrical stimulation, that subject's slice is assigned to that percept quality; otherwise, the slice is designated as tingling. Mech., Mechanical; Vestib., Vestibular; Movt., Movement. (**c**) Table is an example of percept stability in Subject 3 when switching between stimulation patterns. Artificial percept qualities are highlighted in red.

3.5 Discussion

In this work, we found that bursting and tonic stimulation often activate distinct, non-overlapping perceptive pathways. Even though burst percepts required higher stimulation amplitudes to be perceived, the percept was not located near tonic percepts, and instead generated a percept in a unique, non-overlapping location. Furthermore, bursting patterns evoked percepts in different locations than tonic patterns with the same average pulse rate and same amplitude. Hence, in many sites tested, the temporally irregular distribution of pulses provided control of percept location that was independent of stimulation amplitude or average pulse rate. In addition to the above findings, we also found that: (1) bursting percepts required increased amplitude but similar charge as percepts generated from tonic patterns, (2) the perception threshold was lower at sites with different tonic/burst percept locations than similar locations, and (3) tonic and bursting patterns elicited different perceptual qualities.

3.5.1 Activation of distinct thalamocortical networks through patterned stimulation

A similar phenomenon was reported by Kiss and colleagues in 2/19 sites near Vc using waveforms with different pulse-widths (Kiss et al., 2003). This difference was attributed to differential activation of local cells and axons of passage (Kiss et al., 2003; Grill et al., 2005). Kiss and colleagues state that, in a site presumed to be below Vc and in medial lemniscus, auditory sensations were produced using a 5-ms pulse width and the quality changed to tingling using a 500-µs pulse width. In the second site, hemibody pain at 5-ms pulse width transitioned to hand coolness at 3 ms and hand/leg tingling at 1 ms. Kiss and colleagues (Kiss et al., 2003) proposed that local cells were activated through activation of the soma with high-pulse-width waveforms and not low-pulse-width waveforms. However, because extracellular stimulation of

local cells initiates action potentials at the initial segment or at one of the nodes of Ranvier, this observation is likely due to relative differences in the electrode position with respect to the soma (Miocinovic and Grill, 2004; Grill et al., 2005).

As opposed to varying the pulse width, we varied pulse density using either bursting or low-frequency stimulation patterns. In contrast to the findings of Kiss and colleagues, high-frequency versus bursting percepts were produced in different and non-overlapping anatomical regions in roughly half of sites/subjects. Anatomically-distinct percepts could arise if distinct neural populations were activated with different stimulation patterns. Several groups have shown through computational models that stimulation patterns could potentially select different populations of neurons with neural elements that pass near the electrode (McIntyre and Grill, 2002; Yi and Grill, 2018; Anderson et al., 2019). McIntyre and Grill showed that high-frequency stimulation may more efficiently activate axons of passage (because the pulse arrives at a time of *increased* axonal excitability within a depolarizing afterpotential) and less efficiently activate local cells (because the pulse arrives at a time of *decreased* axonal excitability within a hyperpolarizing afterpotential) (McIntyre and Grill, 2002). Yi and Grill also reported that local cells are less excitable with high-frequency stimulation compared to low frequency stimulation when the soma was closer to the electrode than the axon (Yi and Grill, 2018). Although further studies are needed to establish exact mechanisms, these studies provide insight into how distinct subpopulations of neurons (i.e. “hand” neurons versus “face” neurons) can be selectively activated to produce distinct percepts.

Given that various modalities of somatosensory stimuli evoke bursting in Vc (Lee et al., 2005), burst and tonic percept locations may be mediated differentially encoded in thalamocortical relay cells and interpreted differently by downstream cortical mechanisms

(Iremonger et al., 2006; Luczak et al., 2015; Halassa and Kastner, 2017). Some have hypothesized that naturally occurring thalamic spiking modes, bursting and tonic, select for different thalamocortical pathways (Halassa and Kastner, 2017). Iremoner and colleagues show that electrical stimulation of thalamic afferents of motor cortex neurons at high frequencies does not produce action potentials in motor cortex while low frequency stimulation reliably produces action potentials in cortical neurons (Iremonger et al., 2006). Finally, cortical centers may process sensory information differently when action potentials are quantized in bursts (or packets) as opposed to those repeated at constant time intervals(Luczak et al., 2015).

3.5.2 Anatomical location of stimulation sites

Not all stimulation sites produced pattern-dependent percepts. To gain insight into the location of sites, we did note a small but significant lower current threshold when anatomical areas were disparate. Sites of somatosensory thalamus with relatively lower amplitudes of perception have been found to occur in sites densely populated with neural elements (Tasker et al., 1972; Lenz et al., 1994b; Lenz et al., 1994a). Tasker and colleagues have shown especially low thresholds (0.1-0.5 mA; using 60-Hz, 3-ms pulses) at the medial-ventral base of Vc where medial lemniscus fibers enter (Tasker et al., 1972). Lenz and colleagues (with the same stimulation parameters) showed a lower threshold at sites in Vc where the receptive fields of numerous neurons overlapped suggesting a site densely populated with neural elements (Lenz et al., 1994a). Given that face and hand somatotopic centers of Vc are in close proximity (Lenz et al., 1988), a potentially unifying explanation for the data herein is that sites with disparate hand and face percepts occurs at the border of these centers and in an area densely populated with neural elements such as the base of Vc. Specifically, burst patterns activate local face neurons,

and tonic patterns activate either medial lemniscus fibers traveling to hand neurons or thalamocortical cell axons after leaving hand neurons.

3.5.3 Potential for clinical application

Herein bursting patterns are shown to select for distinct perceptive locations that may correspond to activating different subpopulations of thalamocortical-relay neurons. To this end, bursting patterns and multi-contact hardware designs may be combined so that a single DBS lead activates a high number of different neuron groups (Pollo et al., 2014; Swan et al., 2017). Additionally, since bursting patterns activate different neuronal populations than tonic stimulation, bursting patterns could be more effective than tonic patterns in stimulation of Vc for neuropathic pain (Starr et al., 2009; Gross and Boulis, 2018), although further studies are needed. Finally, selective activation of the desired neuron group may lead to fewer side-effects if unwanted neurons are not activated.

Peripheral nerve stimulation with temporally irregular patterns (pulse-width modulation) was used for a sensory prosthesis by Tan and colleagues to restore naturalistic perception (Tan et al., 2014). Patterned stimulation also demonstrated more tolerable paresthesias in spinal cord stimulation (Tan et al., 2016). In this work, bursting patterns achieved a higher number of non-tingling percepts (9/14) and increased percept variety compared to tonic stimulation that produced artificial paresthesias in all but one site. Even though the bursting percepts from thalamic macrostimulation were not endorsed as naturalistic, more naturalistic percepts may be achieved with similar temporally-irregular designs.

3.6 Conclusions

Temporally patterned stimulation shows tremendous promise in advancing the field of neuromodulation, and tuning patterns of stimulation for specific patients and applications may lead to improvements in chronic pain therapies, intraoperative localization, avoidance of side-effects, and sensory prostheses. However, a paucity of studies exists exploring patterned stimulation in Vc where the terminal effect of stimulation pattern can be readily observed. Herein, we showed that patterned stimulation selects for distinct perceptive networks, and likely distinct thalamocortical networks. This specificity for distinct networks provides insight into the underlying mechanisms of temporally irregular patterns and may allow selective activation of optimal neuronal targets.

Chapter 4. Neural Dynamics in Primate Cortex During Exposure to Subanesthetic Concentrations of Nitrous Oxide

A version of this work is being prepared for submission.

4.1 Abstract

Nitrous oxide (N_2O) is a hypnotic gas with anti-depressant and psychedelic properties at subanesthetic concentrations. Despite longstanding clinical use, there is insufficient understanding of its effect on neural dynamics. We administered subanesthetic (70%), inhaled N_2O and studied dynamic changes of spiking rate, spectral content, and somatosensory information transfer to primary motor cortex (M1) in two male Rhesus macaques implanted with Utah microelectrode arrays in the hand area of M1. In M1, the average, sorted multi-unit spiking rate increased from 8.1 ± 0.99 Hz to 10.6 ± 1.3 Hz in Monkey W ($p < 0.001$) and from 5.6 ± 0.87 Hz to 7.0 ± 1.1 Hz in Monkey N ($p = 0.003$). Power spectral densities showed an increase in beta and gamma band power. To evaluate somatosensory information transfer to M1, fingers were lightly brushed and classified using a naïve Bayes classifier. In both monkeys, the proportion of correctly classified fingers dropped from 0.50 ± 0.06 before N_2O to 0.34 ± 0.03 during N_2O administration ($p = 0.018$), although some fingers continued to be correctly classified ($p = 0.005$). The decrease in correct finger classifications corresponded to decreased modulation depth for the population ($p = 0.005$) and fewer modulated units ($p = 0.046$). However, the increased single unit firing rate was not correlated with its modulation depth ($R^2 < 0.001$, $p = 0.93$). Collectively, these data suggest that representation of somatosensory information in M1 is

degraded during subanesthetic N_2O but this does not appear to be mediated by changes in firing rate.

4.2 Introduction

Nitrous oxide (N_2O) and ketamine are unique anesthetics with anti-depressant (Tadler and Mickey, 2018) and psychedelic (Icaza and Mashour, 2013) effects at subanesthetic concentrations. Unlike canonical general anesthetics, they (1) are thought to act by antagonizing glutamatergic NMDA receptors (Thomson et al., 1985; Jevtovic-Todorovic et al., 1998) rather than through the potentiation of GABAergic transmission, (2) increase cerebral metabolism (Takeshita et al., 1972; Deutsch and Samra, 1990), (3) enhance high-frequency electroencephalographic activity (Rampil et al., 1998; Lee et al., 2013; Akeju et al., 2016), and (4) increase cortical cholinergic tone (Shichino et al., 1998; Pal et al., 2015). There has been a recent focus on how large-scale brain networks are modulated by general anesthetics in terms of functional connectivity, dynamics, and graph-theoretical variables (Cao et al., 2018; Huang et al., 2018; Lee and Mashour, 2018); however, there is a paucity of mesoscopic network data for ketamine and N_2O. Network-level dynamics may provide insights into the unique properties of these drugs.

We previously characterized neural firing rate, cortical oscillations, and information transfer in nonhuman primate cortex during exposure to anesthetic concentrations of ketamine (Schroeder et al., 2016). In the current study, we investigated the effects of N_2O on neuronal spiking rate and high-frequency content of local field potentials in primary motor cortex (M1) of the nonhuman primate brain. Furthermore, previous animal studies suggest that somatosensory afferents from S1 mediate transfer of sensory information to M1 (Andersson, 1995; Farkas et al.,

1999; Mao et al., 2011). Thus, to evaluate the effect of N_2O transfer and representation in the cortex, the somatosensory content in M1 during a finger brushing task was measured.

4.3 Materials and Methods

4.3.1 Surgical procedure

Experimental protocols were approved by the Institutional Animal Care and Use Committee at the University of Michigan. Two male rhesus macaques, Monkey W and Monkey N, were implanted with Utah arrays (Blackrock Microsystems, Salt Lake City, Utah) in primary motor cortex (M1) using methods previously described (Schroeder et al., 2016). Monkey W was implanted with two 96-channel Utah arrays, with one in M1 and one in somatosensory cortex (S1). Monkey N was implanted on the left with two split arrays (total of 96 channels) in M1 and 1 96-channel array in S1. Either before or during a wound revision procedure, the wire bundle from the left-sided implant of Monkey N was damaged and eliminated the signal from 32 of the channels. Because of this damage, Monkey N was eventually re-implanted in the contralateral (right) cortex with two split arrays in M1 and one in S1, shown in Fig. 1A. There were no clinically significant adverse events besides wound revision surgeries for exposed hardware from a receding wound edge during healing.

4.3.2 Experimental setup and N2O administration

Three tests were performed on 3 days, separated by several months, for each nonhuman primate: one for Monkey W, one for the left implant of Monkey N (day 1 of Monkey N), and one

for the right implant of Monkey N (day 2 of Monkey N) . The macaques were trained to sit in a monkey chair (Crist Instrument, http://www.cristinstrument.com), with their head secured in customized titanium posts (Crist Instrument), while their Utah arrays were connected to the Cerebus neural signal processor (NSP, Blackrock Microsystems) and their arms were secured in acrylic restraints. The monkeys were also trained to tolerate finger brushings without agitation. Using a cotton-tip applicator, individual fingers were manually brushed without skin indentation at a 2-Hz rate timed to a metronome. The fingers brushed during a given trial were randomly selected by a computer running xPC Target (Mathworks, Natick, Massachusetts) and displayed on a monitor to prompt the experimenters. Brushings were conducted for 5 s, and the first 2 s were discarded from the analysis given that the experimenters switched fingers during the first 2 s of each trial. Given the desire for only sensory information in motor cortex, trials in which the monkey moved spontaneously were noted and later discarded from the analysis. See Schroeder and colleagues (Schroeder et al., 2016) for further details and illustrations regarding the experimental set-up.

Seventy-percent N_2O was delivered at a continuous rate via sealed face mask secured snuggly around the head with an elastic band. Monkey W was gradually acclimated to the mask over several sessions with rewards. Monkey N tolerated the mask on the first day of training. The face mask was placed 10-20 min prior to N_2O administration to allow the monkey to become comfortable with the face mask system. On day 1 for Monkey W before N_2O administration, classification of finger brushings was compared for room air and 100% oxygen via sealed face mask that did not show significant differences in correct classification of finger brushings. This test was not performed on day 2 for Monkey N.

During N_2O delivery, the monkeys were monitored under direct observation by lab technician, trained graduate student, or physician. During N_2O administration, monkeys remained awake and cooperative; heart rate and respiratory rate were checked every 15 min. Respiratory rate remained adequate (always > 32 breaths per minute) throughout the experiments. After N_2O administration, 100% O_2 was administered for 5 min, and monitoring was continued for an additional 15 min after cessation of supplemental oxygen. The monkeys remained awake and did not lose consciousness, as evidenced by widely open eyes and normal frequency of motor movements and conjugate eye movements. There were no adverse events related to N_2O administration.

4.3.3 Front-end processing—analog to cleaned multi-units

The output from the Utah array was processed in two distinct formats. The first data stream was the raw signal sampled at 30 kHz. This broadband data stream was used for the spectral analysis described below. The second data stream was the time stamp of all recorded spikes for all channels. Spikes were defined using the Cerebus neural signal processor (Blackrock Microsystems, Salt Lake City, UT) when the 250-Hz high-pass filtered signal crossed a threshold of -4.5 times the root-mean-squared (RMS) voltage. The Cerebus system then communicated the detection of a spike to a computer running customized software in the xPC Target environment (MathWorks, Natick, MA). The xPC Target computer logged the timestamp of the received spike in 1 ms time bins. This structure allowed replay of experimental spikes offline as well as trial-by-trial organization that will be discussed in subsequent sections.

In some analyses described below, sorted units were required. Spikes were sorted using Offline Sorter (Plexon, Dallas, TX). Sorted clusters were scored with a number between 1 and 4.

The principle components of threshold crossing events were calculated and displayed in a two-dimensional space. Sorted units with a score of 4 correspond to when the principle components of the cluster do not overlap with other threshold crossing events; 3, clusters with little overlap with other clusters; 2, non-clusters and a morphologic bipolar spike in the time domain, and 1, the remaining threshold crossing events. Sorted units with a score of 1 were excluded, those scored 2 were considered sorted multi-units, and those scored 3 and 4 were considered isolated single units.

Because we wanted to include neural information from the hash unit, all threshold crossing events were used for population-based decoding analysis and for calculating the modulation depth. These unsorted multi-units were reviewed by eye and channel waveforms that were not consistent with a neuronal action potential were removed from the analysis.

Removing data at times of motor movement was a multi-step process. First, during finger brushing trials, times of movement were flagged by experimenters, and this data was not included in the subsequent analysis. Second, using an automated program, any finger brushing trial were removed if 30 or more channels recorded a spike at in the same 1-ms bin, as this high level of activity was not consistent with a motionless monkey. Third, the raw spike tracings during Monkey W recordings were reviewed to ensure that no times of high activity (corresponding to movement) were missed. Since there were not additional times flagged, this step was bypassed in Monkey N.

4.3.4 Data analysis—spike time dynamics

To compare the spiking rate before and during N_2O administration, the neural data for Monkey N was combined for both days (but each monkey's neural data was kept separate). The

pre-N_2O data included the 15-min period prior to N_2O administration, as this corresponded to the times the monkey was secured in the testing chair without significant motor movements. Pre-N_2O multi-units with a spiking rate greater than 2 Hz were included and the spikes in the remaining channels were sorted. The pre-N_2O spiking rate was then determined by averaging across all sorted multi-units. To include only spontaneous activity, only sorted units with firing rate greater than 0.5 Hz were analyzed. To compute the spiking rate during N_2O, we averaged the multi-units during the first 45 min of N_2O (using the same multi-units used in the pre-N_2O time period). A period of 45 min was chosen to keep the time under N_2O the same for each day when computing the spiking rate.

Since times of observed monkey movements were not recorded when finger brushings were not being performed, an automated algorithm was used to flag dense neural activity that likely corresponded to monkey movement. When the number of recorded spikes within a 3 ms time bin exceeded a pre-specified threshold, the surrounding 1-s interval was excluded from the spike rate calculation. This threshold was empirically determined by reviewing raster plots by visual inspection to ensure that these periods of dense neural activity were excluded. The distribution of sorted multi-units was plotted as a histogram. Ten-Hz bins were used for Monkey W and 5 Hz bins were used for Monkey N (because of a lower average spiking rate). To compute the trends in spiking rate versus time, the spiking rate was calculated as a running average over 5 min. Sample raster plots at 15 min after N_2O administration are shown to give a typical example. The multi-units are sorted in order of increasing spiking rate in the pre-N_2O state and these sorted indices are also used to depict the raster plots generated during N_2O administration.

4.3.5 Spectral analysis

Spectrograms were calculated from the broadband signal, sampled at 30 kHz, from the Cerebus neural signal processor. Because removing data from the time series introduces discontinuities in the spectrogram, no time series data was removed (e.g., periods with movement are included in the spectrogram). The signal is first decimated using *decimate.m*, which included a 1000 order FIR low-pass filter. After decimation, the signal is high-pass filtered with a 1000-order FIR filter using *fir1.m*. The power spectrum is then calculated by averaging the power spectrum from all channels with a spiking rate greater than 2 Hz as given in section 2.4. The power spectrum for each channel was calculated using spectrogram.m and time window of 0.5 s, 50% overlap, and the default hamming window. The final spectrogram was smoothed in the time by a 15-sample moving median filter and the amplitude was normalized such that the maximum amplitude was at 0 dB.

After observing changes in the spectrogram during N_2O administration, a period of maximal effect between 10 and 20 min after beginning N_2O was compared to the period 5-15 min before N_2O. The spectra were calculated for each channel using the *pwelch.m* algorithm in MATLAB (MathWorks) using as inputs 1-s time periods and 50% overlap. The data were then averaged across all non-noise channels with spiking rate greater than 2 Hz in each respective time session. For clarity, the spectrum was normalized by the value at 10 Hz in pre-N2O time period for each respective monkey.

4.3.6 Finger classification

Finger brushings were performed while N_2O was administered. The first day of Monkey W and the second day of Monkey N (right-sided implant) were selected for a more detailed

analysis. Day 1 for Monkey N (left-sided implant) could not be used for a finger brushing analysis because too many of these trials were corrupted by recording noise. In both monkeys, finger-brushing sessions were conducted for 10 min with 5-10 min breaks between sessions. In Monkey W, the first finger-brushing session was not included since there was no equivalent period in Monkey N. Also, times after 66 min could not be analyzed because the mask was intermittently unsealed and there were software-related recording errors. The first session of finger brushings for Monkey N on day 2 was excluded from the analysis because most trials were contaminated by movement and the following section was removed as there was no finger brushing session in Monkey W at the equivalent time period.

The three brushing sessions for each monkey were labeled as the **pre-N_2O**, **early**, and **late** sessions. In Monkey W, the **early** session began 23 min after starting N_2O, and the **late** session began at 45 min. In Monkey N, the **early** session began 22 min after N_2O, and the **late** session at 38 min. Differences in timing in each session were attributed to roughly 10-min breaks between sessions for Monkey W and roughly 5-min breaks between sessions for Monkey N.

A naïve Bayes classifier with leave-one-out cross validation was used to classify three distinct finger brushings as previously described (Schroeder et al., 2016) using unsorted multi-units. Again, unsorted multi-units (as opposed to sorted multi-units) were used to retain information in the neural hash unit. The multi-units used to classify finger brushings all had spiking rates greater than 2 Hz. Units were not pre-screened with analysis of variance (ANOVA) to include units with potentially small amounts of information. Specifically, during the pre-N2O state, the differences in spiking rate between brushed fingers were evaluated with one-way ANOVA, and those with a p-value greater than 0.05 were excluded from the analysis.

On both days, 4 fingers were brushed and the results of classifying all fingers were included in the following analyses. Three fingers for which the effect could be clearly illustrated were selected for visualization. In both monkeys, fingers 2, 3, and 5 were selected as this combination of fingers in both monkeys had high numbers of modulated units. Because testing periods required motionless and cooperative behavior from the monkey, no attempt was made to use the exact number of trials each day.

4.3.7 Tuning curves and normalized modulation depth

Modulation depth for each brushing session was calculated. The modulation depth between digits *i* and *j* is given below in Eq. 1, where μ_i denotes the mean firing rate when digit *i* is brushed and σ_i denotes the standard deviation. The normalized modulation depth (MD_N) is given in Eq. 2, where MD_{rand} is the calculated modulation depth when the fingers associated with the brushing trials are randomly permutated and averaged over 1,000 trials within the finger-brushing session being analyzed. Normalization was necessary because the spiking rates differed across finger brushing trials and because a finger-brushing session with fewer trials would be biased toward higher modulation depths (for the same reason that the standard error of the mean decreases with an increasing number of samples).

$$MD_{i,j} = \frac{\left|\mu_i - \mu_j\right|}{\sqrt{{\sigma_i}^2 + {\sigma_j}^2}}$$

Equation 4-1

$$MD_N = \frac{MD_{i,j}}{MD_{rand}}$$

Equation 4-2

Tuning curves were calculated for all discriminated single units (scores of 3 or 4). The mean and standard error of the mean (SEM) for the spiking rate vs. finger brushed are calculated for each of these multi-units.

4.3.8 Experimental design and statistical analysis

The experimental design, including animal descriptions, is detailed in the preceding sections. Statistical analyses were performed on a desktop computer using MATLAB. Unless otherwise described, statistical significance was deemed as $\alpha < 0.05$. A one-tail, binomial test was used to evaluate whether finger-classification sessions during N_2O administration performed better than chance rate. The chance rate was 1/3 when brushing 3 equally likely fingers and 1/4 for four equally likely fingers. The calculation was made using *binocdf.m* in MATLAB. When two finger combinations were examined for statistical significance (Section 3.3.1), a Bonferroni correction was applied to lower the level for statistical significance to 0.025. Otherwise, the level of statistical significance was $\alpha = 0.05$. Fisher's exact test was used to compare categorical random variables. Parameterized statistical tests between two groups were made with a one-sample, two-tailed t-test.

4.4 Results

4.4.1 Increased spiking rate with administration of N_2O

In motor cortex, spiking rate increased after exposure to N_2O. After excluding all channels with a spiking rate less than 2 Hz and then spike sorting, Monkey W had 72 sorted

multi-units, the left implant of Monkey N had 19 sorted multi-units, and the right implant of Monkey N had 24 sorted multi-units. The raw tracings from channel 25 in Monkey W in Fig. 1B illustrated the increase spiking rate of a discriminated single unit 15 min into N_2O administration compared to before N_2O administration. The raster plots in Fig. 1D also illustrate the typical increased spiking rate of the total population after 15 min of N_2O administration.

Previous studies suggest that the maximal effect of N_2O occurs within 15-20 min of onset (Stevens et al., 1983; Schroter et al., 2012), and Fig. 1D shows that the change in baseline spiking rate in motor cortex follows this previously reported trend. There is a rapid increase in spiking rate within the first 15-20 min of N_2O administration. In all cases, the firing rate either peaks or plateaus at around 20-30 min. The pre-N_2O baseline firing rate was 8.1 Hz for Monkey W, 4.7 Hz for the left cortex of Monkey N, and 6.4 Hz for the right cortex of Monkey N. The average sorted multi-unit spiking rate was increased from 8.1 ± 0.99 Hz to 10.6 ± 1.3 Hz in Monkey W ($p < 0.001$; two-tailed t-test) and increased from 5.6 ± 0.87 Hz to 7.0 ± 1.1 Hz in Monkey N ($p = 0.003$; two-tailed t-test). The change in firing rate is shown in Fig. 1A.

Although firing rate generally increased, with a spiking rate increase in 80% of the units analyzed, the effect was not uniform. Fig. 1C shows a histogram of change in firing rate in individual multi-units. As can be seen in Fig. 1C, the histogram is centered right of zero, indicating that, as a group, multi-units showed increased firing rate. In some multi-units, there was a substantial increase in firing rate (>10 Hz), while the majority of multi-units increased by only a few Hz. Of note, the firing rate decreased in only 11 multi-units (15%) in Monkey W and 12 multi-units (28%) in Monkey N with N_2O. There were no observed differences in the waveform morphology in isolated units with increased versus decreased firing rate.

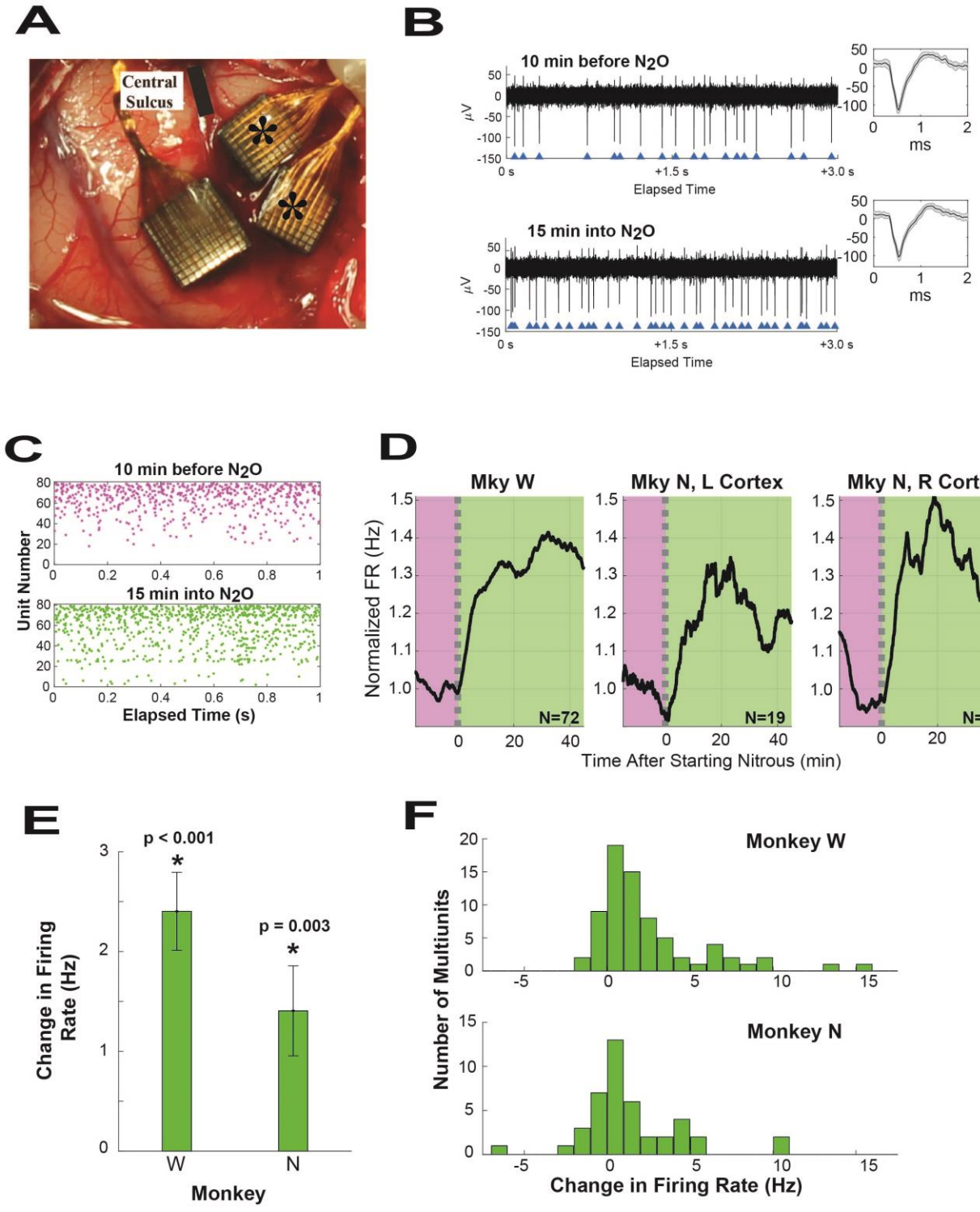

Figure 4-1. Influence of nitrous oxide on spiking rate.
The pre-N_2O states are indicated by the purple background and green indicates continuous N_2O administration. (A) Image of the implanted arrays in primary motor cortex. Central sulcus is indicated with a solid black line and asterisks denote the split motor arrays used in this analysis. The sensory array was not analyzed. (B) The raw data from channel 25 shows discriminated

single units at 10 min prior to N_2O administration (top) and 15 min after beginning continuous N_2O administration (bottom). The raw data depict increased spiking rate for this channel. The blue triangles indicate the time of an action potential. The single-unit insets adjacent to the raw data show the mean (in black) and standard deviation (in gray) for spike waveforms from 15 to 5 min before N_2O (top inset) and 10 to 20 min after N_2O initiation (bottom inset) and indicate waveform stability prior to and during N_2O. The y-axis of the inset is in microvolts (μV). (C) One-s raster of Monkey W plot for 1 min before (pre-N_2O, purple) and 15 min after the start of N_20 administration (green) is given to illustrate representative results. (D) The trend of firing rate (FR) is depicted for each monkey. The spiking rate is normalized by the baseline firing rate before N_2O administration. The pre-N_2O baseline firing rate was 8.1 Hz for Monkey W, 4.7 Hz for the left cortex of Monkey N, and 6.4 Hz for the right cortex of Monkey N. The number of sorted multi-units for each day, N, is indicated with each subplot. The dashed lines indicate when N_2O was initiated. (E) The bar plot depicts the change in spiking rate when combining both days for Monkey W and Monkey N. There is a statistically significant increase in spiking rate for both monkeys, as indicated by the asterisk ($p < 0.001$ for Monkey W and $p = 0.003$ for Monkey N). (D) The histograms depict how the spiking rate of sorted multiunits changes with N_2O administration. For both monkeys, the histogram is shifted to the right, indicating an increase in spiking rate.

4.4.2 N_2O modulation of beta and gamma band frequencies

In both monkeys, N_2O administration increased spectral power at frequencies within 20-45 Hz that included both beta (15 – 30 Hz) and low gamma band (30 – 70 Hz). Spectrograms for Monkey W and Monkey N (right implant) are shown in Figs. 2A and 2B, respectively, to illustrate the time evolution of spectral changes with N_2O. Power in the beta and low-gamma band increases beginning around 5-10 min in both animals. Fig. 2C and 2D depict, respectively, the power spectra for Monkey W and the right implant of Monkey N chosen at the time of maximal effect from the spectrogram, 10 – 20 min after beginning administration. The comparison of the power spectra before and during N_2O also highlights the increase in spectral power between 20 and 45 Hz. Although times with movement are not excluded from the spectrogram and spectrum, the results are consistent with the results of the power spectra when instances of motor movement are excluded.

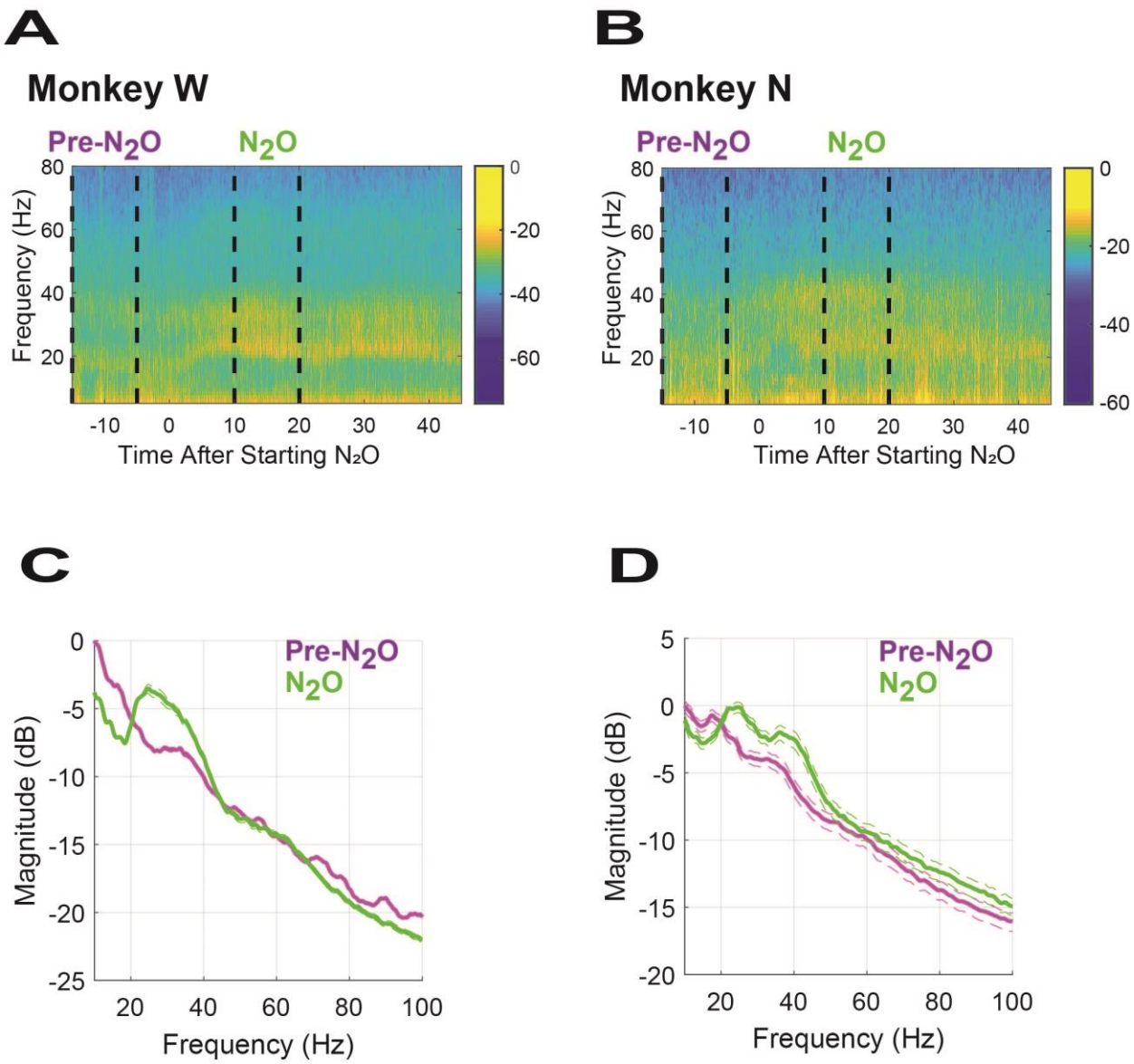

Figure 4-2. Increased high-frequency power during nitrous oxide.
Averaged spectrograms for 55 channels in Monkey W (A) and for 21 channels of the right cortex implant in Monkey N (B). The corresponding averaged power spectrum from 15 to 5 min before N_2O (purple) and 10-20 min into N_2O administration for Monkey W (C) and Monkey N (D). Standard error of the mean is displayed with dashed lines.

4.4.3 N_2O degrades but does not eliminate classification of finger brushings

4.4.3.1 Population analysis

To evaluate information processing associated with spiking and spectral changes, we evaluated the ability to decode sensory information in motor cortex, which is known to represent somatosensory information transferred from S1. Finger brushings were classified using M1 neurons (Fig. 3A). As shown in Fig. 3B, these somatosensory stimuli were classified at three times: **pre-N_2O** (purple), **early** during N_2O (blue) and **late** (red). To prevent introduction of bias, classification was performed on all unsorted multi-units with a firing rate greater than 2 Hz in all finger-brushing sessions. This selection process left 53 units in Monkey W and 19 units in Monkey N. Across trials in Monkey W, there were statistically significant differences in spiking rate: **pre-N_2O**, at 13.41 ± 0.27 Hz and **N_2O** at 19.20 ± 0.27 ($p < 0.001$; t-test). Across all trials in Monkey N, there were also statistically significant differences: **pre-N_2O** at 8.82 ± 0.19 Hz and **N_2O** at 11.35 ± 0.19 ($p < 0.001$; t-test).

In both monkeys and prior to N_2O, brushings of four fingers could be classified better than chance (chance level at 0.25). In Monkey W, the proportion of correct classification was 0.50 ± 0.11 ($p = 0.014$; binomial test, 20 trials). In Monkey N, brushings of four fingers were correctly classified at 0.43 ± 0.067 ($p = 0.003$; 56 trials). To increase the effect for visualization, the confusion plots shown in Fig. 3C illustrate the distribution of correct classification using the same three fingers, D2, D3, D5. For fingers D1, D2, and D3, there were 16 modulated units in Monkey W and 8 in Monkey N (screened with ANOVA test using $\alpha = 0.05$).

To determine whether N_2O impacted the encoding of somatosensory information in M1, the Naïve Bayes classifier trained in the pre-N_2O session was used to classify finger brushings during N_2O administration. For the illustrative fingers (D2, D3, D5), the proportion of correct finger classifications when combining **early** and **late** drops to 0.33 ± 0.06 ($p = 0.54$) in Monkey

W and 0.43 ± 0.06 in Monkey N ($p = 0.05$), illustrated in Fig. 3D. However, the correct classification improves when the Naïve Bayes classifier is trained using trials from the current brushing session under N_2O (using leave-one-out cross validation). For fingers D2, D3, and D5, the percent correct improved to 0.49 ± 0.06 for both Monkey W ($p = 0.005$) and Monkey N ($p = 0.004$), and the confusion matrices are shown in Fig. 3E. For reference, the correct classification using four fingers was 0.38 ± 0.05 for Monkey W ($p = 0.005$) and 0.30 ±0.05 for Monkey N ($p = 0.10$). Combining trials between both monkeys, there was a statistically significant drop in the correct finger classifications from 0.50 ± 0.06 before N_2O to 0.34 ± 0.03 during N_2O ($p = 0.018$). Thus, N_2O administration degrades but does not eliminate the transfer and/or representation of somatosensory content in M1.

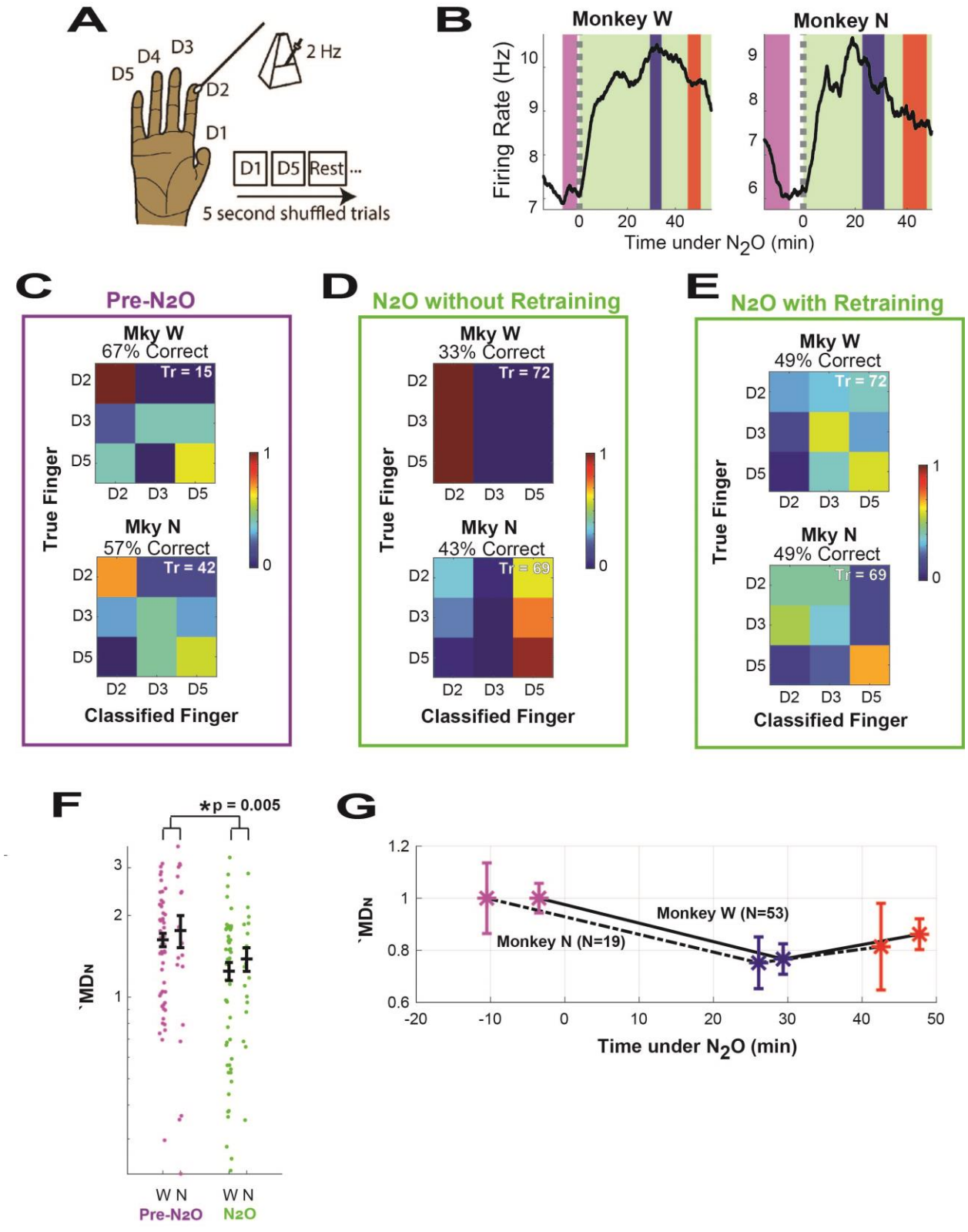

Figure 4-3. Transient degradation of somatosensory information in motor cortex.

(A) Experimental setup consisted of random stimulation of individual fingers at 2-Hz strokes in trials of 5-s duration. (B) Trends of sorted multiunit firing rate for each monkey. The shaded regions highlight the times when fingers were decoded to compare performance in **pre-N_2O** state (purple) and **early** (blue) and **late** (red) N_2O administration. (C) Confusion plots for each monkey illustrate performance of the Naïve Bayes classifier when classifying finger brushings in the **pre-N_2O** state. The vertical axis is the true finger brushed while the horizontal axis is the decoded finger. The percent correct is given above each respective plot. Tr, number of trials classified. The insert to the right of the confusion plots is the legend. (D) Confusion plot during N_2O (combined **early** and **late** brushing sessions) when the classifier is trained using data from the pre-N_2O finger-brushing session. (E) Confusion plot during N_2O (combined **early** and **late** sessions) when training the classifier on the current session (**early** and **late**) using leave-one-out cross validation. (F) Normalized modulation depth (MD_N) for all multi-units in the pre-N_2O (purple) and N_2O (green) brushing sessions. The MD_N of multi-units during N_2O sessions was averaged for both the **early** and **late** sessions. W denotes Monkey W, and N denotes Monkey N. Each filled circle represents one multi-unit. The horizontal bar (in black) and error bars represent the mean and standard error of the mean. The asterisk (*) denotes statistical significance. The y-axis is in log scale to better visualize the data. (G) The mean modulation depths for the **pre-N_2O** (purple), **early** N_2O (blue), and **late** N_2O (red) finger-brushing sessions. The asterisks and error bars indicate the mean and standard error of the mean. The solid line denotes Monkey W and the dashed line denotes Monkey N. Panel A is adapted and reprinted (Schroeder et al., 2016).

4.4.3.2 Multi-unit modulation depth analysis

Although the encoding of somatosensory information is clearly affected by N_2O, the effect on individual multi-units requires separate analysis. The normalized modulation depth (MD_N) of all multi-units is shown in Fig. 3F, where $MD_N < 1$ corresponds to no modulation. In both monkeys, the mean MD_N is greater before than during N_2O ($p = 0.005$). MD_N decreases from 1.63 ± 0.09 to 1.40 ± 0.10 in Monkey W and from 1.76 ± 0.24 to 1.38 ± 0.17 in Monkey N. Despite this drop, combining the number of modulated channels ($MD_N > 2$) across both channels revealed an average of 11 modulated units per N_2O brushing session. However, this is less than the 22 modulated units across both monkeys during the pre- N_2O brushing session ($p = 0.046$). When the well-modulated units ($MD_N > 2$) are removed, the classification of D2, D3, and D5 during N_2O (as shown in Fig. 3E) drops to 0.43 ± 0.06 in Monkey W ($p = 0.054$) and to 0.26 ± 0.05 in Monkey N ($p = 0.92$) and neither was statistically better than chance.

During N_2O, there was no correlation between the modulation depth and the change in firing rate during N_2O ($R^2 < 0.001$, $p = 0.93$) – meaning that units with large increases in firing rate were not more likely to have a low MD_N. As will be illustrated with discriminated single units in the next section, some units lost modulation despite no change in spiking rate and some units maintained modulation despite increased firing rate.

When the **early** and **late** N_2O finger-brushing sessions are separated (Fig. 3G), MD_N does not continue to decrease with continued N_2O administration, despite increasing concentration of N_2O in the brain. The modulation depth, in fact, increases although the increase is not statistically significant ($p = 0.28$).

4.4.3.3 Discriminated single unit examples

To better understand how individual neurons representing somatosensory information are affected by N_2O, we examined the tuning curves of the discriminated single units for each monkey by comparing the **pre-N_2O** with the **early** and **late** epochs. In both monkeys, 12 discriminated units were modulated (ANOVA with $\alpha < 0.05$). Four illustrative examples of the tuning curves for modulated single units are given in Fig. 4A. The curves illustrate the mean firing rate when one of the three fingers (D2, D3, and D5) was brushed. As mentioned above, despite the increased firing rate, these units retained their tuning for finger brushings. In the raw voltage tracings in Fig. 4B, the example for Channel 5 in Monkey N illustrates how brushing D5 continues to evoke a higher firing rate than D3 despite an increased baseline firing rate. Additionally, there were examples where fingers not tuned in the pre-N_2O brushing session became tuned to finger brushings, as in channel 89 in Monkey W.

As described in the preceding section, tuning is lost in many single units during N_2O administration (Fig. 4C). This loss in tuning occurred both in units with increased firing rate (channel 82, Monkey N) and in units with similar firing rates as the pre-N_2O brushing session (channel 96, Monkey W). Raw tracings of channel 82 in Monkey N illustrate how single-unit activity does not clearly differentiate the brushings of finger D3 and D5 during N_2O, although differentiable in the pre-N_2O session. Thus, regardless of changes in firing rate, many units were no longer modulated during N_2O.

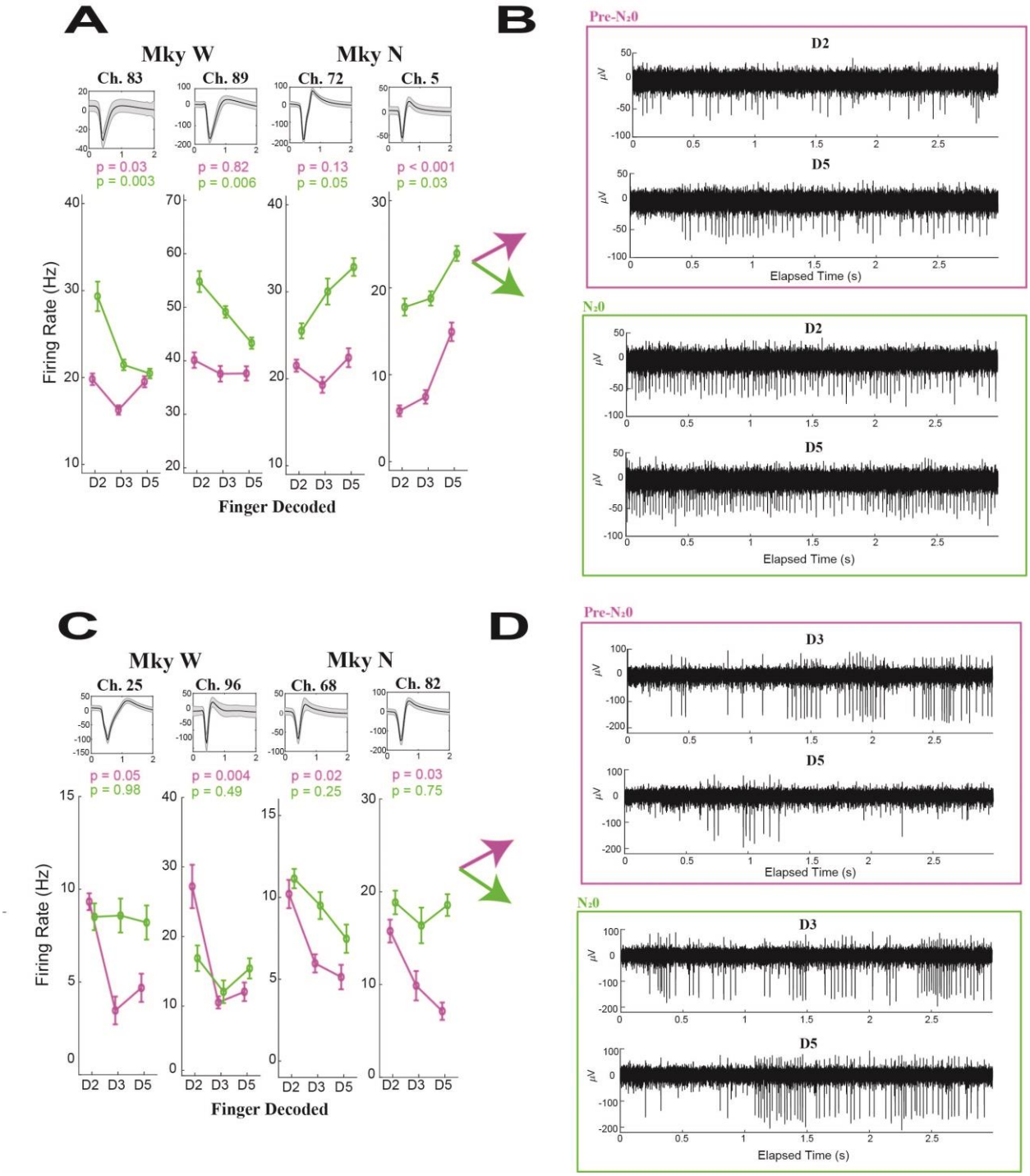

Figure 4-4. **Discriminated single-unit tuning curves.**
(A) Tuning curves for 4 modulated (ANOVA with $\alpha < 0.1$), discriminated single units during N_2O administration. Single units are presented on the left for Monkey W and on the right for Monkey N. Each single unit is labeled with the channel on the array, the average waveform tracing (black line = mean, shaded gray = standard deviation), and the tuning curve. The tuning curve depicts the mean firing rate of the single unit as a function of the finger brushed both in the

pre-N_2O period (purple) and during N_2O (green). The error bars denote the standard error of the mean. The p-values calculated with one-way ANOVA are given for both the pre-N_2O and N2O tuning curves. (B) Raw voltage tracings for the modulated discriminated single unit in channel 5 for Monkey N in the pre-N2O (purple) and N_2O (green) periods. In each pane, the top tracing resulted when the second digit (D2) was brushed and the bottom plot resulted when the fifth digit (D5) was brushed. (C) Four discriminated single units that were originally modulated (ANOVA with $\alpha < 0.1$) in the pre-N_2O period but lost modulation during N_2O administration. (D) Raw voltage tracings illustrating a typical-finger brushing trial for channel 82 in Monkey N.

4.5 Discussion

We have demonstrated, that with continuous inhalation of N_2O: (1) the spiking rate of motor cortex neurons increases, (2) high-frequency power (in beta and low gamma bands) increases, and (3) measurable somatosensory information transferred to the motor cortex persists but is degraded while a smaller number of persistently tuned units remain. The change in somatosensory encoding in M1 is explained by a loss of modulated multi-units and a general decrease in modulation across the population. However, there is not a strong link between the increase in single unit activity and its modulation depth under N_2O suggesting a possible dissociation of representation and changes in firing rate.

4.5.1 Time-frequency dynamics

Only a paucity of data exists concerning the effects of NMDA-receptor antagonists, like N_2O, on mesoscopic neural networks. Recently, canonical agents that potentiate GABA, like propofol and isoflurane, have been shown to decrease spiking rate in cortical mesoscopic networks (Lewis et al., 2012; Ishizawa et al., 2016; Wenzel et al., 2019). Wenzel and colleagues administered isoflurane to achieve various depths of anesthesia and found a depression of spiking activity in somatosensory and visual cortex that is inversely related to anesthetic depth (Wenzel et al., 2019). Lewis and colleagues administered bolus doses of propofol to induce loss

of consciousness and observed decreased spiking activity in temporal lobes (Lewis et al., 2012). Ishizawa and colleagues administered propofol at a continuous rate to induce loss of consciousness and also observed decreased spiking activity in somatosensory and frontal ventral premotor cortices with loss of consciousness (Lewis et al., 2012). NMDA-receptor antagonists are well known to variably modulate neuronal firing rate, depending on neuron type and anatomic location (Patel and Chapin, 1990; Homayoun and Moghaddam, 2007; Wang et al., 2013; Schroeder et al., 2016).

Unlike GABA-potentiating medications, N_2O, an NMDA-receptor antagonist, has previously been observed to increase spiking rate in reticular activating system but decrease spiking rate of somatosensory thalamic relay neurons (Kawamoto et al., 1990). In our study, the spiking rate of motor cortex neurons increased with subanesthetic N_2O. The mechanism for the observed increase in spiking rate is likely due to preferential antagonism of NMDA receptors on inhibitory interneurons, resulting in a disinhibition of pyramidal neurons (Homayoun and Moghaddam, 2007). In contrast to N_2O producing increased spiking rates of M1 neurons, previously reported spiking rate of M1 neurons remained unchanged in nonhuman primates at *anesthetic* doses of ketamine, also an NMDA-receptor antagonist (Schroeder et al., 2016). However, at *subanesthetic* doses of ketamine, Mori et al. previously showed that multi-unit activity increased in the thalamus and reticular activating system of a cat (Mori et al., 1971).

Nitrous oxide has spectral properties unlike typical anesthetics potentiating GABA. With microarray recordings, Ishizawa and colleagues showed gamma and high beta oscillations lasting a few minutes with propofol-induced loss of consciousness, followed by slow frequency delta oscillations (Ishizawa et al., 2016). In particular, after beginning propofol infusion but prior to loss of consciousness (i.e. subanesthetic doses), spectral plots suggest an increase in high beta

(18-25 Hz) in S1 and in low gamma (25-34 Hz) in ventral pre-motor cortex that is similar to our spectral findings with subanesthetic N_2O. Lewis and colleagues likewise found the appearance of slow (< 1 Hz) oscillations in local field potentials after loss of consciousness induced by propofol (Lewis et al., 2012). In spectral analyses of anesthetic doses of ketamine, Lee and colleagues showed a relative increase in gamma band and decrease in beta band power in frontal/parietal EEG data (Lee et al., 2013). Schroeder and colleagues demonstrated the same trends in LFPs of S1 and less obvious trends in M1 (Schroeder et al., 2016). Likewise, Ballesteros et al. found a gradually increase in high beta, low gamma power in ventral premotor cortex, S1, and secondary somatosensory cortex (Ballesteros et al., 2020). Although there are no mesoscopic LFP spectral data with N_2O, previous spectral analyses with EEG data show that N_2O modulates high-frequency power both up and down (Yamamura et al., 1981; Rampil et al., 1998; Foster and Liley, 2011, 2013; Pelentritou et al., 2019). Our finding of increased high-frequency (>20-45 Hz) power in motor cortex is similar to the increased gamma power of Yamamura et al., who reported a peak at 34 Hz with 70% N_2O (Yamamura et al., 1981), and Rampil and colleagues, who reported dual peaks at 40-50 and 70-110 Hz with 50% N_2O (Rampil et al., 1998). The gamma power differences in the literature may be attributed to regional variation or to the lower spatial resolution of EEG leads, as suggested by others (Ray et al., 2008; Eagleman et al., 2018).

4.5.2 N_2O Degrades M1 Somatosensory Representation

Anesthetic agents are diverse in terms of their molecular targets and effect on neuronal activity. Despite these differences, they all share a similar functional property of reversibly suppressing consciousness at anesthetic doses or suppressing cognition at subanesthetic doses.

The mechanism by which GABAergic anesthetics disrupt neural function appears to be clear—they potentiate inhibition and reduce neural activity (Boveroux et al., 2010; Schrouff et al., 2011; Hudetz, 2012). However, it is not clear how non-GABAergic medications affect consciousness or cognition. As discussed above, the NMDA-receptor antagonists, ketamine and N_2O, increase high-frequency oscillations and neural firing rates. It has been suggested that, while GABAergic drugs depress information transfer, non-GABAergic drugs like ketamine and N_2O disinhibit pyramidal neurons leading to dysregulated activity that disrupts information processing (Homayoun and Moghaddam, 2007; Icaza and Mashour, 2013). Our data show that there is decreased somatosensory content that is not simply explained by interference from the increases in firing rate because firing rate changes were not correlated with modulation depth, i.e., neuron tuning. Thus, our data in nonhuman primate cortex do not support the hypothesis of a causal link between increased neural firing patterns and disruptions in information transfer/representation.

4.5.3 Limitations

One limitation of this study is that only motor cortex was studied. However, motor cortex was chosen to emphasize the effects of corticocortical somatosensory pathways, although other somatosensory pathways exist, including thalamocortical, or corticothalamocortical pathways (Petrof et al., 2015; Mo and Sherman, 2019). However, sensory brushings used herein have been previously validated as a model of S1 to M1 information transfer. Furthermore, great care was taken to avoid skin indentation with finger brushings and motor movements were discarded to reduce the contribution of thalamocortical inputs. The delineation of a more detailed effect of N_2O on specific somatosensory afferents requires further study. Finally, a possible confounder to interpreting the drop in accuracy of finger classification would be if an alternate process (e.g.,

agitation, fear) interfered with somatosensory content. However, preliminary control tests did not show significant differences in the number of finger brushings correctly classified with or without the face mask.

4.6 Conclusions

In this study, we investigated the effects of subanesthetic concentrations of N_2O on mesoscopic networks in primary motor cortex of the nonhuman primate. Both spiking rate and high-frequency spectral content of motor cortex neurons increased in response to N_2O. With ongoing N_2O, measurable somatosensory content and number of modulated units in M1 decrease but are not eliminated. The shift to faster dynamics is not clearly associated with the somatosensory representation on a neuronal level and suggest other mechanisms of N_2O that alter perception.

Chapter 5. Classifier Using Pontine Radial Diffusivity and Symptom Duration Accurately Predicts Recurrence of Trigeminal Neuralgia after Microvascular Decompression: A Pilot Study and Algorithm Description

A version of this work was submitted for publication.

5.1 Abstract

OBJECTIVE: To evaluate the utility of pontine-segment diffusion-tensor MRI radial diffusivity (DTI RD), a known biomarker for demyelination and trigeminal neuralgia (TN) subtype, to predict TN recurrence following microvascular decompression (MVD).

METHODS: Pontine-segment trigeminal tract RD was computationally extracted in blinded fashion and normalized to background pontine RD. Following validation against published results, the relationship of normalized RD to symptom duration (D_S) was measured. Both parameters were then introduced into machine-learning classifiers to group patient outcomes as TN remission or recurrence. Performance was evaluated with leave-one-out cross-validation to calculate accuracy, sensitivity, specificity, and receiver operating characteristic curves.

RESULTS: The study population included 22 patients with type 1 TN (TN1), of whom 13 had suitable trigeminal root visualization on DTI. There was a negative correlation of normalized RD to preoperative symptom duration ($p = 0.035$, $R^2 = 0.20$). When pontine-segment RD and D_S were included as input variables, two classifiers predicted pain-free remission versus eventual recurrence with 85% accuracy, 83% sensitivity, and 86% specificity (leave-one-out cross-validation; $p = 0.029$).

CONCLUSIONS: Pontine-segment RD and D_S accurately predict MVD outcomes in TN1. Use of a classifier may allow more accurate risk stratification for neurosurgeons and patients considering MVD as a treatment for TN1. These findings provide further insight into the relationship of pontine microstructure, represented by RD, and the pathophysiology of TN.

5.2 Introduction

Trigeminal neuralgia is a severe facial pain syndrome associated with vascular compression of the trigeminal root at or around the root entry zone (REZ) (Hilton et al., 1994; Love and Coakham, 2001; Devor et al., 2002). In well selected patients with classic trigeminal neuralgia (Type 1, TN1), the severe lancinating pain is readily treated with surgical intervention (Burchiel, 2003; Maarbjerg et al., 2014). Although a variety of interventions exist, the definitive surgical treatment has been microvascular decompression (MVD), which leads to a pain-free outcome in 76% of patients at mean follow-up of 1.7 years (Holste et al., 2020). However, several studies indicate that the pain-free cohort drops to 44-64% after 10 years (Burchiel et al., 1988; Barker et al., 1996; Wang et al., 2017; Hardaway et al., 2019), and operative decompression of the trigeminal root carries significant risk (Hanakita and Kondo, 1988). To stratify patient benefits for MVD, some have proposed preoperative scoring algorithms (Hung et al., 2017; Hardaway et al., 2019). For example, Hardaway and colleagues assign a score from 0-3 using pain type, presence of vascular compression, and compression severity, and find pain-free response rates of 36%, 43%, 56%, and 67% for groups 0, 1, 2, and 3, respectively (Hardaway et al., 2019). In a recent meta-analysis, Holste and colleagues reported that pain-free predictors include disease duration, arterial compression, superior cerebellar artery involvement, and a TN1 classification (Holste et al., 2020).

Recently, diffusion tensor magnetic resonance imaging (DTI) has proven useful in the evaluation of TN patients. DTI studies reveal differences in anatomic microstructure between the affected and unaffected nerve (Herweh et al., 2007; Fujiwara et al., 2011; Leal et al., 2011; Chen et al., 2012; Liu et al., 2013; DeSouza et al., 2014; Lutz et al., 2016; Neetu et al., 2016), and these differences can normalize after successful treatment (Unal et al., 2017; Zhang et al., 2018; Chai et al., 2019; Leal et al., 2019). Hung and colleagues used DTI measurements to stratify patients undergoing Gamma Knife and MVD into responders and non-responders (Hung et al., 2017). In that study, DTI measurements from the pontine segment and trigeminal root informed a linear discriminant analysis classifier to sort TN1 patients into responders and non-responders at a statistically significant level and with 71% accuracy. Furthermore, the DTI measurement of radial diffusivity (RD) has also been shown to differ between trigeminal neuralgia subtypes 1 and 2, which respond differently to MVD (Willsey et al., 2019). RD represents the diffusion of water perpendicular to the direction of maximal diffusion, which is measured by axial diffusivity (Alexander et al., 2007). Increases in RD - with constant axial diffusivity – is often related to demyelination (Song et al., 2002). Given the known role of demyelination in the pathophysiology of trigeminal neuralgia (Love and Coakham, 2001) and previous studies that suggest a link between RD and outcomes (Willsey et al., 2019), we hypothesized that RD may contain prognostic information.

In this report, we investigate using RD in a novel classifying algorithm to predict remission (pain-free outcome) and recurrence in a cohort of 13 TN1 patients undergoing MVD. We developed a computer-assisted approach to locate and to measure pontine-segment trigeminal RD. RD and symptom duration informed machine-learning algorithms to assign each patient into remission or recurrent pain groups. Compared to the earlier study (Hung et al.,

2017), this study not only demonstrates the feasibility of these classifiers in MVD patients but also achieves improved sensitivity and specificity in predicting pain-free response from symptom duration and preoperative RD.

5.3 Materials and Methods

5.3.1 Subject Selection and Classification

The study was approved by the University of Michigan Institutional Review Board (HUM00027829). A total of 29 patients with TN1 without comorbid pain symptoms underwent high-resolution diffusion-tensor MRI (described below). TN1 patients were defined as those where the episodic/lancinating pain occurred more often than constant pain (> 50% episodic pain) (Burchiel, 2003). Five patients were excluded from the study for inadequate visualization of the exiting trigeminal root on imaging, and two patients were excluded for lack of clinical details in the electronic medical record. The remaining 22 patients comprised the TN1 group, which had 15 females. The mean age ± the standard error of the mean (S.E.M.) was 60.1 ± 3.4 years. To evaluate the novel semi-automated technique to calculate pontine-segment RD, the study group included an additional 8 patients with TN2, 6 of whom had adequate trigeminal root visualization on MRI (all female, mean age of 60.1 ± 6.5 years), as well as 15 patients imaged for non-TN conditions to serve as controls (13 females, mean age of 57.5 ± 3.9 years). Control subjects included patients with headaches, fibromyalgia, migraines, rheumatologic disease, and myoclonus of tensor tympani/stapedius.

Of the TN1 group of 22 patients, a total of 13 patients (8 females, mean age of 58 ± 3.5 years) underwent MVD performed by the senior authors (P.G.P. and O.S.). The other 9 patients did not undergo MVD: 3 underwent radiofrequency ablation, 2 underwent glycerol injection, 2

were treated conservatively, 1 pursued treatment at an outside institution, and 1 was lost to follow-up. Patients were labeled as recurrent for any residual or recurrent pain and were labeled as remission only if completely free of pain. To avoid confounding the analysis with subjective pain scores, a strict pain-free requirement is used for those in remission, i.e., Barrow Neurologic Institute pain score of 1. This approach is typical of other studies evaluating the relationship of DTI and treatment outcomes (Hung et al., 2017). In this observational study, routine patient follow-up occurred at 6 weeks and 6 months, and patients were also referred back to the neurosurgery clinic at later time points for evaluation if pain recurred.

5.3.2 Measuring Normalized Pontine Trigeminal Radial Diffusivity

Diffusion tensor MRI imaging was obtained on a 3T system (Achieva Quasar Dual, Philips, Andover, MA) with maximum gradient amplitude = 80 mT/m, rise time = 0.80 ms, and slew rate = 100 T/m/s. DTI protocol included an echo planar single–shot technique, TR = 4956 ms, TE = 62 ms, flip angle = 90°, 16 motion probing gradient orientations, and b = 800 s/mm^2 using 2x image averaging. Two-mm axial slices were obtained with a parallel imaging technique (sensitivity encoding [SENSE]). A 112 x 112 matrix with isotropic voxels was employed to record the measurements.

MRI images were loaded first into Analyze software (AnalyzeDirect Inc., Overland Park, KS), and the axial slice with the best view of the trigeminal root exiting the brainstem was manually selected. This axial slice was then transferred to MATLAB (MathWorks, Natick, MA), as shown in Fig. 1A. A MATLAB subroutine was created to allow the user to place a parameterized line on the dark ridge at the pontine edge, as shown in Fig. 1B. The root entry zone is defined as the portion of the root between where it exits from the brainstem to the distal

point where the central myelination transitions to peripheral myelination.(Peker et al., 2006) Since our analysis was performed only on fibers within the brainstem, we denote this region as the pontine segment. Furthermore, to ensure analysis of pontine segment fibers that exit with the trigeminal root, patients without a well-visualize root exiting the brainstem were excluded. To control for potential patent-to-patient variations in measurement, the peak value of RD along this parameterized line was then selected and normalized by the mean background level of the pons (Fig. 1C). This normalized peak RD value was denoted as P_{RD}, and the remaining analysis was conducted using this value. The protocol described in this section allowed for a semi-automated method for extracting P_{RD} to reduce the variability caused by human measurement.

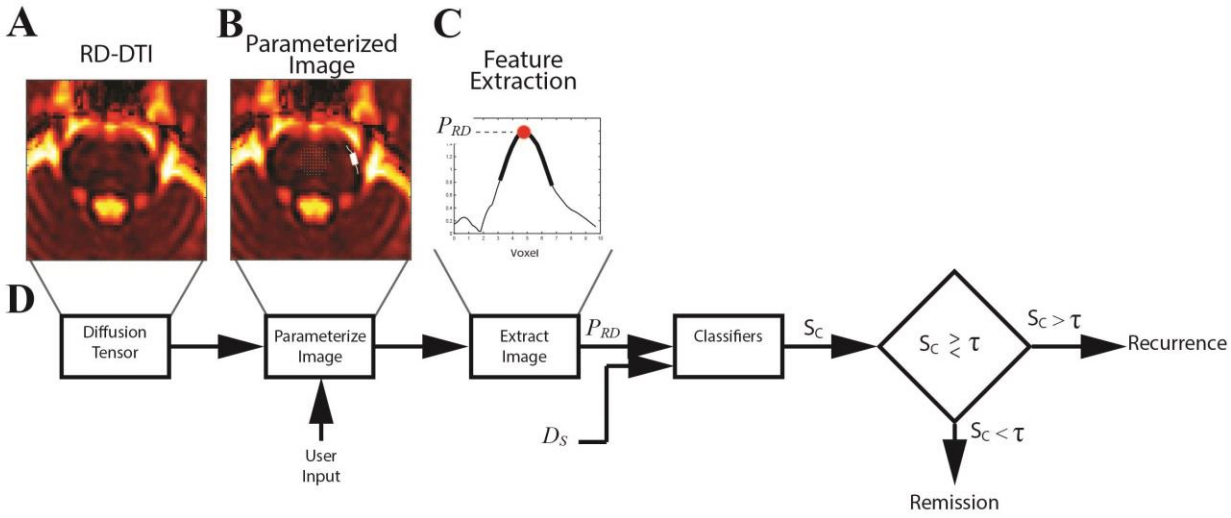

Figure 5-1. Workflow for calculating P_{RD} and predicting response.
(**A**) Raw radial diffusivity image from diffusion tensor imaging (DTI) MRI. (**B**) Raw radial diffusivity MRI depicting how the image was parameterized. The solid white thin line indicates a spline fit curve that estimates the position of the dark ridge at the edge of the pons. The solid white thick line indicates the gap between the dark ridge where the trigeminal fibers likely exit. The fine white dots in the pons indicate the voxels used to calculate the average radial diffusivity in the pons. (**C**) The radial diffusivity normalized by the pontine background level. The normalized peak radial diffusivity value, P_{RD}, is indicated by the red dot. (**D**) The flow chart illustrates the workflow for extracting the value of P_{RD}, using a classifier to convert this to a score, S_C, comparing S_C to a threshold, τ, to make a prediction of either "Remission" or "Recurrence".

5.3.3 Validation of P_{RD} Metric against Previously Published Results

The current method differs from our previously published method, which examined DTI parameters in a small region of interest in the pontine segment of the trigeminal tract.(Willsey et al., 2019) To validate this new method, we compared P_{RD} for the 22 TN1, 6 TN2, and 15 control patients to verify that P_{RD} was elevated in the TN1 group compared to TN2 and control patients, as previously reported.(Willsey et al., 2019) P_{RD} ipsilateral to the pain was also compared with P_{RD} contralateral to the pain to verify that ipsilateral was greater than contralateral P_{RD}. Authors were blinded to diagnosis and sidedness of the trigeminal pain. TN1 patients, TN2 patients, and controls were randomly mixed together prior to P_{RD} determination.

5.3.4 Machine Learning Classification and Cross-Validation

To assess whether preoperative P_{RD} predicts treatment response, two machine learning classifiers were used to group patients as remission or recurrence. Both P_{RD} and the duration of symptoms (D_S) – as P_{RD} was found to be correlated with D_S – were input into each classifier. The objective for the machine-learning classifiers was to create a linear boundary in two-dimensional space (D_S versus P_{RD}) between remission and recurrence groups. We relied on the linear least squares classifier (LLSC) to provide this linear delineation to avoid overfitting our data with more sophisticated machine learning classifiers and so that results generalized to higher numbers of patients. The LLSC can be calculated with a closed-form expression and is equivalent to the linear discriminant analysis classifier (used by Hung and colleagues (Hung et al., 2017)) when there are only two classes with equal numbers of patients (Hastie et al., 2009). The LLSC is

mathematically described by Eq. 5-1 where *w* is calculated according to the minimization in Eq. 5-2.

$$\hat{y}_i = sign(w^T x_i)$$

Equation 5-1

$$\min_w[J(w)] = \min_w \left[\sum_{i=0}^{N} (y_i - w^T x_i)^2\right]$$

Equation 5-2

N is the number of patients, x_i is a *3x1* array $(1, D_s^{(i)}, P_{RD}^{(i)})$, $D_s^{(i)}$ is the symptom duration of the i^{th} patient, $P_{RD}^{(i)}$ is the normalized peak radial diffusivity of the i^{th} patient, and y_i is 1 for remission and -1 for a recurrence. The weights, w, for the LLSC are calculated directly in Python using the function LinearRegression in the sklearn.linear_model toolbox. Detailed discussions of the LLSC are provided in Section 4.2 by Hastie and colleagues (Hastie et al., 2009) or in Section 5.8 by Duda and colleagues (Duda et al., 2000).

To ensure that performance was not entirely dependent on the choice of classifier, a support-vector machine (SVM) was also used to classify patients (Hastie et al., 2009). Similar to the LLSC, SVM was chosen to avoid overfitting the data. Unlike LLSC, SVM attempts to minimize errors at a boundary instead of allowing all the data to influence calculation of the boundary. The width of the border zone is parameterized by a parameter, C, and high C values correspond to narrow border zone widths. Normally, C is determined empirically through cross-validation, but this was not possible because of our limited sample size. We chose the value to be high as we expected the two classes of remission and recurrence to be clustered close together. The SVM weights were calculated in Python using the svm subroutine from sklearn toolkit. Detailed review of the classifiers is described by Hastie and colleagues (Hastie et al., 2009).

The performance of each classifier was evaluated with leave-one-out cross-validation and consisted of (1) removing one patient, (2) generating two classifiers with the remaining 12 patients, and (3) classifying the removed patient into either the remission or recurrent group. This served to control the retrospective nature of the study and approximate prospective results. Sensitivity and specificity with leave-one-out cross-validation were then calculated on this data set. Finally, ROC curves were also generated with leave-one-out cross-validation.

5.3.5 Statistical Analysis

A p-value of 0.05 was used for statistical significance. Statistical significance between TN1, TN2, and control groups was conducted with one-way ANOVA analysis, and homoscedasticity was verified with Bartlett's test. Post-hoc comparisons between groups was conducted with Tukey's honestly significant difference test. Python functions used were: statsmodels.stats.multicomp.tukeyhsd, scipy.stats.f_oneway, and scipy.stats.bartlett. Statistical differences between the ipsilateral and contralateral pontine segment in TN1 patients was evaluated with a paired, two-tailed t-test using scipy.stats.ttest_ind.

Parameterized random variables (symptom duration and patient age) were compared with P_{RD} using a univariate regression analysis to determine a p-value. The P_{RD} values for gender was evaluated with a two-sided, two-sample t-test to determine a p-value. Only one random variable, symptom duration, had a p-value less than 0.1, so a univariate regression analysis was used to evaluate the relationships between P_{RD} and symptom duration. The p-values for linear regression and t-tests were calculated with stats.linregress and stats.ttest_ind from the scipy Python library.

The statistical significance of the classifiers was evaluated with Fisher's exact test using stats.fisher_exact function from the scipy Python library. Post-hoc comparisons between gender,

age, and symptoms duration in remission and recurrence groups were made with either a paired, two-tailed t-test or Fisher's exact test. To assess the relative contributions of the independent variables in the models predictive power, the outcome data were regressed over the independent variables (P_{RD} and symptom duration) using a generalized linear-least squares model. The calculation was performed in python using the *gls* function in the statsmodels.formula.api toolbox.

Receiver-operating characteristic (ROC) curves and area under the curve (AUC) were calculated. The x-axis of the ROC curve illustrates the false positive rate (FPR), which equals 1 minus the specificity. The y-axis of the ROC curve illustrates the true positive rate, which equals the sensitivity. The ROC curves illustrate, for range of operating points, the sensitivity and specificity. ROC curves were calculated in Python programming language (version 3.7.3, Python Software Foundation, http://www.python.org/) using the roc_curve and auc subroutines in the sklearn.metrics toolbox.

5.4 Results

5.4.1 Surgical Outcomes for TN1 Patients

Of 13 TN1 patients undergoing MVD, there were 6 patients in remission (46%) and 7 with recurrent pain (54%). Mean recurrence time of was 1.7 yrs and a maximum recurrence time was 8 yrs. Two patients with recurrent pain were noted to have venous instead of arterial compression at the time of surgery, which may have contributed to a suboptimal response in these two patients. These results are similar to previous reports of long-term success after MVD ranging from 44% to 64% at 10 years using a strict pain-free criterion for success (Burchiel et al., 1988; Barker et al., 1996; Wang et al., 2017). Patient and outcome demographics are given in

Table 1. There were no statistically significant differences in a post-hoc comparison between patients in remission and recurrence groups with respect to gender ($p = 0.27$), age ($p = 0.08$), or symptom duration ($p = 0.23$).

Patient	Group	Sex	Age (yrs)	Pain Distribution	Pain Duration (yrs)	Recurrence Onset (yrs)
1	Remission	F	72	V1/2/3	4	-
2	Remission	F	45	V1	1	-
3	Remission	F	67	V2/3	0.5	-
4	Remission	M	76	V1/2/3	6.5	-
5	Remission	F	66	V2/3	7	-
6	Remission	F	62	V2/3	7.5	-
7	Recurrence	M	37	V1/2	3	0.1
8	Recurrence	F	51	V2/3	2	0.1
9	Recurrence	M	63	V1/2	10	6
10	Recurrence	F	67	V2/3	12.5	4
11	Recurrence	F	49	V2/3	11	0.8
12	Recurrence	M	62	V1	1.5	2
13	Recurrence	M	38	V1/2/3	10	0.1

Table 1. **Outcome demographics**

5.4.2 Updated P_{RD} Calculation Differentiates TN1 from TN2 and Pain-Free Controls

In our previous work, we found differences in RD between TN1 and TN2 patients (Willsey et al., 2019). To ensure that our new method for extracting radial diffusivity still allows differentiation between TN1 and TN2, P_{RD} was compared for 22 TN1 patients, 6 TN2 patients, and 15 controls in order to validate the updated method for calculating P_{RD}. Fig. 2A illustrates the values of P_{RD} for patients with TN1, TN2, and controls. As previously reported, P_{RD} was different between the groups (one-way ANOVA, $p < 0.001$). The post-hoc analysis revealed P_{RD} for TN1 (1.57 ± 0.09) was greater than for TN2 (1.11 ± 0.14, $p = 0.008$) and for controls (1.05 ± 0.06, $p = 0.001$). The ROC curve to differentiate TN1 from controls is given in Fig. 2B, and the AUC is 0.88. To serve as an internal control, P_{RD} was also compared ipsilateral and contralateral to the TN pain. As expected from previous findings, P_{RD} ipsilateral to the pain (1.53 ± 0.09) was greater than contralateral to the pain (1.21 ± 0.08; $p = 0.010$, t-test).

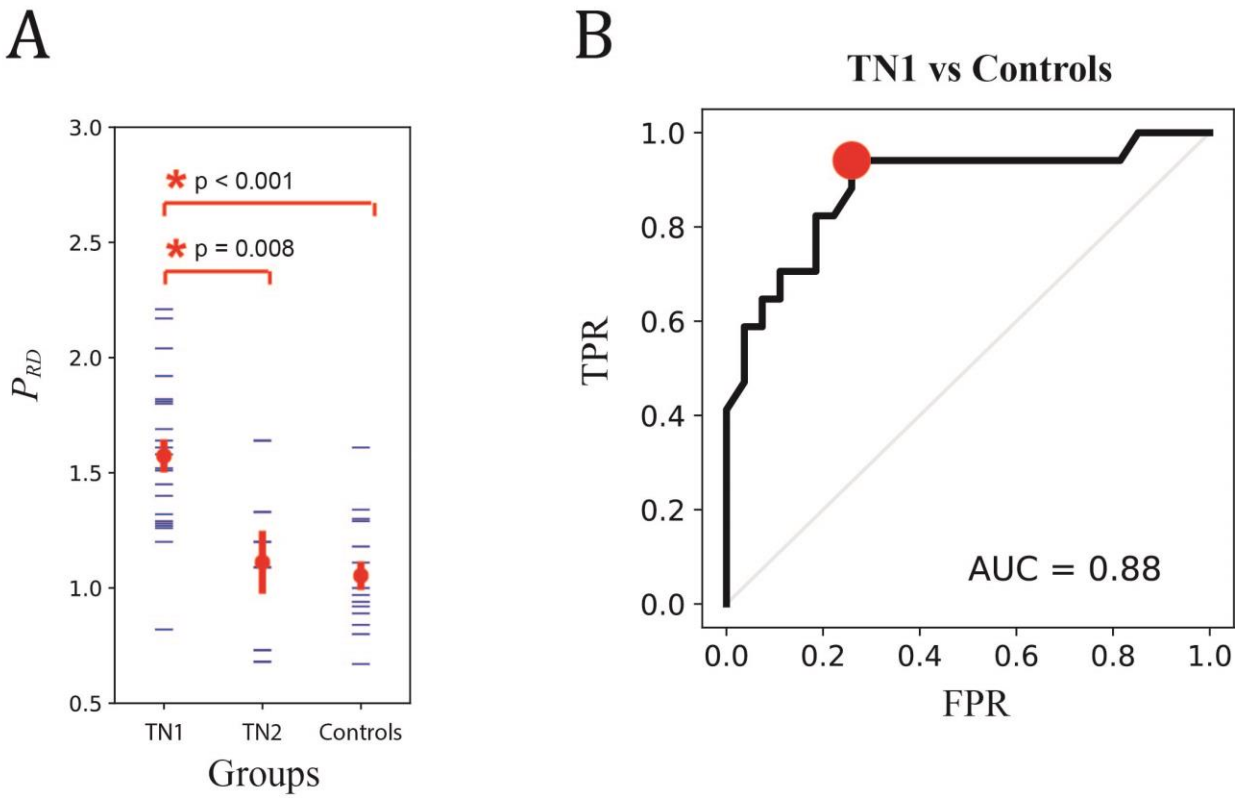

Figure 5-2. Comparing P_{RD} in TN1 to TN2 plus controls.
(**A**) Illustrates the values of P_{RD} for the TN1, TN2, and control groups (n = 22, 6, and 15, respectively). The horizontal blue ticks indicate the value of P_{RD} for an individual patient. The red dot and error bars indicate the mean and standard error of the mean. for the group, respectively. The asterisk denotes statistical significance. P-values are given in the table using two-sample, two-sided t-test. Two control patients had the same value of 0.94 for P_{RD}. (**B**) The receiver operating characteristic curve describing the classification of TN1 versus controls. AUC = area under the curve; FPR = false positive rate (1 – specificity); P_{RD} = peak radial diffusivity; TN1 = type 1 trigeminal neuralgia; TN2 = type 2 trigeminal neuralgia; TPR = true positive rate (sensitivity).

5.4.3 Radial Diffusivity and Symptom Duration Predict Surgical Outcome

Given the relationship between radial diffusivity and demyelination (Song et al., 2002), the effect of symptom duration on P_{RD} was examined to explore the potential role of demyelination in the pontine segment. As shown in Fig. 3, P_{RD} is negatively correlated with symptom duration among our 22 patients with TN1 (p = 0.035). The calculated slope was -0.029/yr and the y-intercept was 1.7. The correlation coefficient, R, was calculated to be -0.45. An R^2 value of 0.20 indicates the linear regression with symptom duration captures only about 20% of the variance in peak P_{RD}. There were no statistically significant associations between age (p = 0.21; R^2 = 0.04) or gender (p = 0.72). Furthermore, P_{RD} of the contralateral side was not correlated with symptom duration (p = 0.22; R^2 = 0.08).

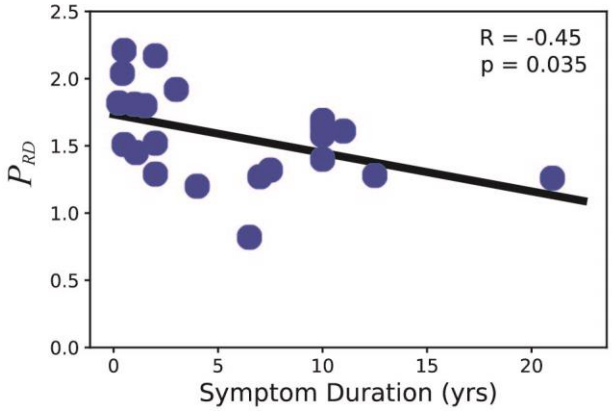

Figure 5-3. P_{RD} correlated with symptom duration.
The blue dots represent the P_{RD} for each of the 22 patients. The black line is the calculated linear regression line. R is the correlation coefficient, and p denotes the p-value for the linear regression.

5.4.4 Radial Diffusivity Predicts Response to Intervention

Since radial diffusivity differs between TN1 and TN2 trigeminal neuralgia subtypes, which are known to respond differently to MVD (Willsey et al., 2019), P_{RD} was hypothesized to predict MVD outcome. To evaluate this hypothesis, both preoperative symptom duration and preoperative P_{RD} (found to depend on symptom duration) were used to predict patient outcome. Both the LLSC and SVM were used to classify patients into remission and recurrence. The boundary between predicted remission and recurrence for each of the two classifier types is overlaid on the patient outcome data and shown in Fig. 4A. As can be seen in the figure, each classifier separates most outcomes correctly into remission and recurrence groups. A complete evaluation, with cross-validation, for each classifier is shown using the ROC curves in Fig. 4B. The AUC is 0.81 for LLSC and 0.71 for SVM. Evaluating each classifier on this data set with leave-one-out cross-validation produces percent correct of 85% for linear regression ($p = 0.029$) and 85% for SVM ($p = 0.029$). Both LLSC and SVM operate with a sensitivity of 83% and a specificity of 86%. The sensitivity/specificity operating point for each classifier is indicated by the color-coded dot in Fig. 4B. In a post-hoc analysis of the complete data, regressing recurrence outcomes over P_{RD} and symptom duration were statistically significant ($p = 0.02$, adjusted $R^2 = 0.44$) and revealed relative equal predictive contribution of P_{RD} ($t = 2.96$) and symptom duration ($t = 2.92$).

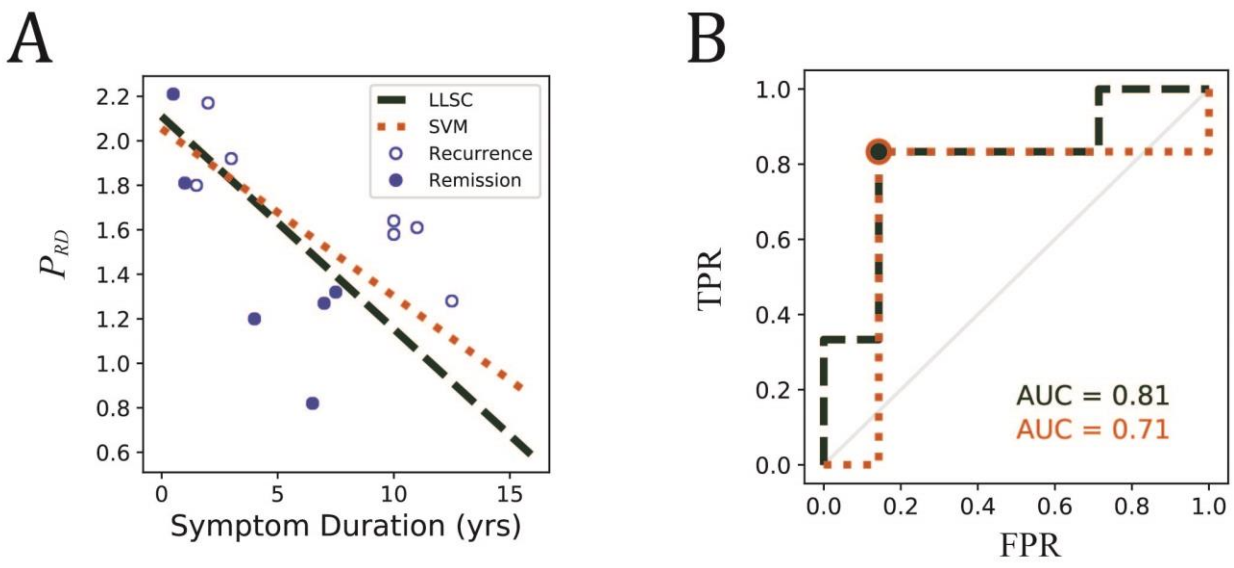

Figure 5-4. P_{RD} and symptom duration predict outcome.
(**A**) The classifiers are shown separating remission and recurrence based on symptom duration and P_{RD}. Linear-least-squares classifier (LLSC) is in dark green and support-vector machine classifier (SVM) is in orange. Open blue dots indicate recurrence, and solid blue dots indicate remission after intervention. (**B**) Receiver operating characteristic curves are given for each classifier in **A**. The area under the curve (AUC) for each classifier is color coded as in **A** and given in the bottom right corner. FPR = false positive rate (1 – specificity); TPR = true positive rate (sensitivity).

5.5 Discussion

Given previous reports of the prognostic value of DTI in trigeminal neuralgia (Hung et al., 2017; Wang et al., 2017; Willsey et al., 2019), the value of radial diffusivity to predict MVD outcome is evaluated in this study. Radial diffusivity may be an especially useful DTI measurement given its relationship to demyelination and the role of demyelination in trigeminal neuralgia. Radial diffusivity was evaluated using a computer-assisted method for locating the pontine segment of the trigeminal tract. We have demonstrated that (1) symptom duration, $D_{S,}$ is negatively correlated with peak radial diffusivity, P_{RD}, and (2) D_S and P_{RD} can be inputs to a machine-learning classifier that correctly predicts long-term response with 85% accuracy and a sensitivity of 83% and specificity of 86%.

5.5.1 DTI Abnormalities in the Pontine Segment of the Trigeminal Tract

While there are multiple DTI studies of the trigeminal root and REZ (Herweh et al., 2007; Leal et al., 2011; Lutz et al., 2011; Liu et al., 2013; DeSouza et al., 2014; Lummel et al., 2014; DeSouza et al., 2015; Lin et al., 2016; Lutz et al., 2016; Neetu et al., 2016), few studies examine DTI parameters in the pontine segment of the trigeminal tract (Chen et al., 2016; Hung et al., 2017; Willsey et al., 2019). The lack of studies likely results from the sophisticated methods needed to differentiate between crossing fibers in the brainstem (Qazi et al., 2009). However, in this and our previous work (Willsey et al., 2019), extracting DTI measurements adjacent to the exiting trigeminal root may select for trigeminal fibers without requiring sophisticated tractography algorithms. In particular, by using this semi-automated method to calculate P_{RD} from the region of the pons adjacent to the exiting root (Fig. 1A-B), the P_{RD} may be specific for fibers originating from the chief sensory nucleus of V (Chen et al., 2016) and may account for the improvement in differentiating between TN1 versus controls in this work compared to our previous work (Willsey et al., 2019).

Studies that have not found correlations between DTI changes in TN for symptom duration did not include DTI measurements of the pontine segment (Fujiwara et al., 2011; Liu et al., 2013). Herein, we find that the increase in radial diffusivity is negatively correlated with symptom duration. Since radial diffusivity is a non-invasive marker of demyelination (Song et al., 2002), the negative correlation may be explained by an initial insult to the trigeminal root, which leads to demyelination that progressively remyelinates with time. Remyelination is known to occur in the REZ (Hilton et al., 1994). Regardless, more studies are needed to understand the time evolution of DTI changes in the pontine segment of the trigeminal tract.

5.5.2 Predicting Response to Intervention with Preoperative DTI Measurements

Two groups have used DTI measurements in TN patients to predict responses to treatment. Tohyama and colleagues showed post-procedure fractional anisotropy, when measured after Gamma-Knife radiosurgery, predicts a long-term (12 mo.) response (Tohyama et al., 2018). Hung and colleagues retrospectively compared preoperative DTI measurements of 14 responders and 17 nonresponders to either MVD or Gamma-Knife radiosurgery (Hung et al., 2017). While no individual DTI measurement alone classified responders and nonresponders better than chance, linear combinations of DTI measurements from both the pontine segment and trigeminal root (determined by linear discriminant analysis) correctly classified responder and nonresponders with 71% accuracy when using leave-one-out cross-validation.

In this study, we used P_{RD} and D_S to inform LLSC and SVM that correctly classified 85% of MVD patients with a sensitivity of 83% and a specificity of 87%. Given that the linear discriminant classifier used by Hung et al. is very similar to our LLSC (equivalent for equal numbers of responders versus non-responders), improvement in accuracy (85% versus 71%) could be attributed to (1) including symptom duration in the classifier, (2) including only MVD patients, and/or (3) the semi-automated algorithm to measure radial diffusivity (Hung et al., 2017). Specifically, the semi-automated algorithm to extract radial diffusivity from pontine segment may only include values most predictive of MVD response.

Previous studies support prognostic information both in symptom duration and radial diffusivity. First, Hung et al. found that the majority of the predictive power was derived from the pontine segment, with radial diffusivity being the most important DTI measurement (Hung et al., 2017). Second, in a recent meta-analysis, preoperative symptom duration was found to

predict response to treatment (Holste et al., 2020). Thus, our success in classification grouping patients into remission and recurrence groups may result from optimal combinations of radial diffusivity and symptom duration.

5.5.3 Limitations

The limitations of this study are the relatively small number of patients treated at our center, the number of patients who could not be analyzed due to inadequate visualization of the pontine segment of the trigeminal tract, and the variable follow-up for patients in this observational study. Regardless, radial diffusivity is a promising biomarker for prediction of surgical outcomes and may assist with surgical decision making. Definite validation is possible through a prospective, multicenter study with defined inclusion and exclusion criteria and follow-up time periods.

5.6 Conclusions

In this study, we present a semi-automated method to extract a single DTI measurement, normalized radial diffusivity, from the pontine segment of the trigeminal tract. A statistically significant negative correlation between radial diffusivity and preoperative symptom duration was found and then used to predict remission and recurrence with 85% accuracy in an MVD-only cohort. Combining this DTI-based decision tool with other clinical decision tools may improve the selection of patients most likely to achieve a pain-free outcome after MVD. Furthermore, the insights gained suggest a role for demyelination of the pontine segment in the disease pathophysiology, since RD with constant axial diffusivity is often considered a non-invasive surrogate for demyelination (Song et al., 2002).

Chapter 6. Discussion

6.1 Conclusions

Sensorimotor pathways are important to everyday functioning and, when dysfunctional, the impact on patient quality of life can be substantial (Tate et al., 2002). The cortical and thalamic interfaces investigated herein may be useful in restoring lost sensorimotor function and help answer important neuroscience questions related to sensorimotor function. Further, novel imaging was shown to assess the structural integrity of sensory roots in a non-invasive manner.

The focus of Chapter 2 was to achieve higher-velocity motor movements with a neural network decoder. In particular, a feedforward neural network decoder was compared with the ReFIT Kalman filter – representative of currently used motor decoders (Gilja et al., 2012; Vaskov et al., 2018). The neural network decoder in both real-time and in offline analyses achieved higher velocities and reached random targets more quickly than the ReFIT Kalman filter.

While these results require validation with additional animals and across other labs, the approach herein may provide a blueprint for further improvements. Neural networks could be recalibrated with intention-based retraining similar to the ReFIT Kalman filter. There also exists potential for network architectures to be further optimized. For example, convolutions could be performed temporally or spatially across electrodes. Furthermore, improved feature engineering input into the network may also improve performance as the only features explored herein were spike-band power in 50-ms bins (Nason et al., in press).

In Chapter 3, we explored patterned stimulation during electrical stimulation of somatosensory thalamus. In doing so, the stimulation pattern was found to select for distinct perceptive pathways that may correspond to distinct anatomical thalamocortical pathways. For a sensory prosthetic, naturalistic percepts may be dependent on both stimulation pattern/waveform and site of stimulation (Ohara et al., 2004; Heming et al., 2010; Swan et al., 2017), and this work may suggest a relationship between the pattern of stimulation and site of activated neurons. In DBS applications, patterned stimulation may steer neuron activation to reduce unwanted symptoms and side effects. These stimulation patterns could be further optimized to generate more "naturalistic" percepts or select more than 2 distinct pathways. While these results apply to macrostimulation, microstimulation could also be explored.

Accessing neural pathways with brain machine interfaces allow study of sensorimotor pathways in new ways previously not possible. Specifically, in Chapter 4, the somatosensory content in motor cortex, likely from somatosensory cortex afferents, was measured during a pharmacological perturbation with nitrous oxide. In response to nitrous oxide, the somatosensory content was degraded, which helps connect the molecular target of this NMDA receptor antagonist to M1 neuron behavior and likely to the S1 to M1 circuit. These basic neuroscience findings may also be helpful in future motor BMIs attempting to incorporate somatosensory feedback (Chien et al., 2017). These results could be extended to include additional medications or additional implant locations or studied in human patients capable of reporting sensory disturbances.

Finally, Chapter 5 describes novel use of magnetic resonance diffusion tensor imaging to predict patient response to surgical intervention for patients with trigeminal neuralgia – thought to be caused by compression of the root providing sensation to the face. These results require

validation with prospective clinical trials, and the classifiers could be expanded to include other important patient variables including gender and age.

6.2 The Future for BMIs

BMIs have progressed rapidly from initial demonstrations in animal studies (Serruya et al., 2002; Taylor et al., 2002), and today there are multiple centers with human clinical trials (Hochberg et al., 2012; Collinger et al., 2013; Aflalo et al., 2015). However, there is still substantial work left to be done before these devices are widely accepted by the general patient population. There currently exists no cost-effective, basic prototype where the daily benefit outweighs the risk and limitations. In analogous terms, Henry Ford's Model T provided an easily manufactured, cost-effective automobile to help consumers through daily life that established a new standard. There is no Model T for BMIs. Not only would such a device benefit patients at-large, it would also help consolidate the field and provide a launching point for additional improvement and investment.

Likely prohibitive limitations include unmet performance and functionality minimums, device durability, and device convenience and safety. Device performance may not need to enhance or even match the functionality of native hands, but performance is a priority to patients and must allow patients to efficiently complete important activities (Blabe et al., 2015). Designing devices around a core group of tasks important to the typical patient will help clarify the needed speed, degrees of freedom, and additional functionality. Furthermore, stable functionality is needed without long re-training periods to fine tune the device. Device durability is needed so that implanted arrays last for many years as current devices are limited by gliosis and scarring that limits the life expectancy of implanted arrays (Bullard et al., 2019). This

process is thought to be irreversible and may exclude that neural tissue from future use. Finally, convenience/safety factors include development of fully implanted devices. Transcutaneous devices risk infection, and patients have strong preferences not to be wired to a machine (Blabe et al., 2015).

Further neuroscience and engineering research are needed to address these fundamental limitations. To name only a few, outstanding neuroscience questions include: Why do motor decoders need to be retrained before each session? And how can we minimize the daily retraining and fine tuning? (Irwin et al., 2017; Vaskov et al., 2018) Engineering advances are needed to further develop wireless technology and low-power devices so that these devices can be fully implantable (Nason et al., in press). Despite the work left to be done, progress will surely continue up to and past the point where neuroprosthetic devices become widely adopted, since providing humans intuitive neural access to the control machines provides tremendous potential to restore lost function.

Bibliography

(n.d.) Spinal Cord Injury: Hope Through Research. In: National Institute of Neurological Disorders and Stroke.
Adamchic I, Hauptmann C, Barnikol UB, Pawelczyk N, Popovych O, Barnikol TT, Silchenko A, Volkmann J, Deuschl G, Meissner WG (2014) Coordinated reset neuromodulation for Parkinson's disease: Proof‐of‐concept study. Movement disorders 29:1679-1684.
Aflalo T, Kellis S, Klaes C, Lee B, Shi Y, Pejsa K, Shanfield K, Hayes-Jackson S, Aisen M, Heck C (2015) Decoding motor imagery from the posterior parietal cortex of a tetraplegic human. Science 348:906-910.
Akeju O, Song AH, Hamilos AE, Pavone KJ, Flores FJ, Brown EN, Purdon PL (2016) Electroencephalogram signatures of ketamine anesthesia-induced unconsciousness. Clinical neurophysiology : official journal of the International Federation of Clinical Neurophysiology 127:2414-2422.
Alexander AL, Lee JE, Lazar M, Field AS (2007) Diffusion tensor imaging of the brain. Neurotherapeutics 4:316-329.
Anderson DN, Duffley G, Vorwerk J, Dorval AD, Butson CR (2019) Anodic stimulation misunderstood: preferential activation of fiber orientations with anodic waveforms in deep brain stimulation. Journal of neural engineering 16:016026.
Anderson KD (2004) Targeting recovery: priorities of the spinal cord-injured population. Journal of neurotrauma 21:1371-1383.
Andersson G (1995) Cortico‐cortical mediation of short‐latency (lemniscal) sensory input to the motor cortex in deeply pentobitone anaesthetized cats. Acta physiologica scandinavica 153:381-392.
Armour BS, Courtney-Long EA, Fox MH, Fredine H, Cahill A (2016) Prevalence and causes of paralysis—United States, 2013. American journal of public health 106:1855-1857.
Ballesteros JJ, Huang P, Patel SR, Eskandar EN, Ishizawa Y (2020) Dynamics of Ketamine-induced Loss and Return of Consciousness across Primate Neocortex. Anesthesiology: The Journal of the American Society of Anesthesiologists 132:750-762.
Barker FG, Jannetta PJ, Bissonette DJ, Larkins MV, Jho HD (1996) The long-term outcome of microvascular decompression for trigeminal neuralgia. N Engl J Med 334:1077-1084.
Birdno MJ, Kuncel AM, Dorval AD, Turner DA, Gross RE, Grill WM (2011) Stimulus features underlying reduced tremor suppression with temporally patterned deep brain stimulation. Journal of neurophysiology 107:364-383.
Blabe CH, Gilja V, Chestek CA, Shenoy KV, Anderson KD, Henderson JM (2015) Assessment of brain–machine interfaces from the perspective of people with paralysis. Journal of neural engineering 12:043002.
Boveroux P, Vanhaudenhuyse A, Bruno M-A, Noirhomme Q, Lauwick S, Luxen A, Degueldre C, Plenevaux A, Schnakers C, Phillips C (2010) Breakdown of within-and between-network resting state functional magnetic resonance imaging connectivity during propofol-induced loss of consciousness. Anesthesiology: The Journal of the American Society of Anesthesiologists 113:1038-1053.

Brochier T, Boudreau M-J, Paré M, Smith AM (1999) The effects of muscimol inactivation of small regions of motor and somatosensory cortex on independent finger movements and force control in the precision grip. Experimental brain research 128:31-40.
Brocker DT, Swan BD, So RQ, Turner DA, Gross RE, Grill WM (2017) Optimized temporal pattern of brain stimulation designed by computational evolution. Science translational medicine 9:eaah3532.
Brocker DT, Swan BD, Turner DA, Gross RE, Tatter SB, Koop MM, Bronte-Stewart H, Grill WM (2013) Improved efficacy of temporally non-regular deep brain stimulation in Parkinson's disease. Experimental neurology 239:60-67.
Bullard AJ, Hutchison BC, Lee J, Chestek CA, Patil PG (2019) Estimating Risk for Future Intracranial, Fully Implanted, Modular Neuroprosthetic Systems: A Systematic Review of Hardware Complications in Clinical Deep Brain Stimulation and Experimental Human Intracortical Arrays. Neuromodulation: Technology at the Neural Interface.
Burchiel K (2003) A new classification for facial pain. Neurosurgery 53:1164-1167.
Burchiel KJ, Clarke H, Haglund M, Loeser JD (1988) Long-term efficacy of microvascular decompression in trigeminal neuralgia. J Neurosurg 69:35-38.
Cagnan H, Pedrosa D, Little S, Pogosyan A, Cheeran B, Aziz T, Green A, Fitzgerald J, Foltynie T, Limousin P (2016) Stimulating at the right time: phase-specific deep brain stimulation. Brain 140:132-145.
Cao W, Zhang F, Yu H, Hu B, Meng Q (2018) Preliminary research of a novel center-driven robot for upper extremity rehabilitation. Technology and health care : official journal of the European Society for Engineering and Medicine 26:409-420.
Carmena JM, Lebedev MA, Crist RE, O'Doherty JE, Santucci DM, Dimitrov DF, Patil PG, Henriquez CS, Nicolelis MA (2003) Learning to control a brain–machine interface for reaching and grasping by primates. PLoS biology 1.
Chai W, You C, Zhang W, Peng W, Tan L, Guan Y, Chen K (2019) Diffusion tensor imaging of microstructural alterations in the trigeminal nerve due to neurovascular contact/compression. Acta Neurochir (Wien) 161:1407-1413.
Chen DQ, DeSouza DD, Hayes DJ, Davis KD, O'Connor P, Hodaie M (2016) Diffusivity signatures characterize trigeminal neuralgia associated with multiple sclerosis. Mult Scler 22:51-63.
Chen J, Guo ZY, Liang QZ, Liao HY, Su WR, Chen CX, Fu SX, Han XJ (2012) Structural abnormalities of trigeminal root with neurovascular compression revealed by high resolution diffusion tensor imaging. Asian Pacific journal of tropical medicine 5:749-752.
Chien JH, Korzeniewska A, Colloca L, Campbell C, Dougherty P, Lenz F (2017) Human Thalamic Somatosensory Nucleus (Ventral Caudal, Vc) as a Locus for Stimulation by INPUTS from Tactile, Noxious and Thermal Sensors on an Active Prosthesis. Sensors (Basel, Switzerland) 17.
Collinger JL, Wodlinger B, Downey JE, Wang W, Tyler-Kabara EC, Weber DJ, McMorland AJ, Velliste M, Boninger ML, Schwartz AB (2013) High-performance neuroprosthetic control by an individual with tetraplegia. The Lancet 381:557-564.
Davis KD, Kiss ZH, Tasker RR, Dostrovsky JO (1996) Thalamic stimulation-evoked sensations in chronic pain patients and in nonpain (movement disorder) patients. J Neurophysiol 75:1026-1037.
Davis KD, Tasker RR, Kiss ZH, Hutchison WD, Dostrovsky JO (1995) Visceral pain evoked by thalamic microstimulation in humans. Neuroreport 6:369-374.

Deer T, Slavin KV, Amirdelfan K, North RB, Burton AW, Yearwood TL, Tavel E, Staats P, Falowski S, Pope J (2018) Success using neuromodulation with BURST (SUNBURST) study: results from a prospective, randomized controlled trial using a novel burst waveform. Neuromodulation: Technology at the Neural Interface 21:56-66.

DeSouza DD, Hodaie M, Davis KD (2014) Abnormal trigeminal nerve microstructure and brain white matter in idiopathic trigeminal neuralgia. Pain 155:37-44.

DeSouza DD, Davis KD, Hodaie M (2015) Reversal of Insular and Microstructural Nerve Abnormalities Following Effective Surgical Treatment for Trigeminal Neuralgia. Pain 156:1112-1123.

Deutsch G, Samra SK (1990) Effects of nitrous oxide on global and regional cortical blood flow. Stroke 21:1293-1298.

Devor M, Govrin-Lippmann R, Rappaport ZH (2002) Mechanism of trigeminal neuralgia: an ultra-structural analysis, of trigeminal root specimens obtained during microvascular decompression surgery. J Neurosurg 96:532-543.

Dorval AD, Kuncel AM, Birdno MJ, Turner DA, Grill WM (2010) Deep brain stimulation alleviates parkinsonian bradykinesia by regularizing pallidal activity. Journal of neurophysiology 104:911-921.

Dostrovsky JO, Davis KD, Lee L, Sher GD, Tasker R (1993) Electrical stimulation-induced effects in the human thalamus. Advances in neurology 63:219-229.

Duda R, Hart P, Stork D (2000) Pattern classification. New Jersey, NY. In: USA: Wiley-Interscience.

Eagleman SL, Drover CM, Drover DR, Ouellette NT, MacIver MB (2018) Remifentanil and nitrous oxide anesthesia produces a unique pattern of EEG activity during loss and recovery of response. Frontiers in human neuroscience 12:173.

Farkas T, Kis Z, Toldi J, Wolff J-R (1999) Activation of the primary motor cortex by somatosensory stimulation in adult rats is mediated mainly by associational connections from the somatosensory cortex. Neuroscience 90:353-361.

Flesher SN, Collinger JL, Foldes ST, Weiss JM, Downey JE, Tyler-Kabara EC, Bensmaia SJ, Schwartz AB, Boninger ML, Gaunt RA (2016) Intracortical microstimulation of human somatosensory cortex. Science translational medicine 8:361ra141-361ra141.

Foster BL, Liley DT (2011) Nitrous oxide paradoxically modulates slow electroencephalogram oscillations: implications for anesthesia monitoring. Anesthesia & Analgesia 113:758-765.

Foster BL, Liley DT (2013) Effects of nitrous oxide sedation on resting electroencephalogram topography. Clinical Neurophysiology 124:417-423.

Fujiwara S, Sasaki M, Wada T, Kudo K, Hirooka R, Ishigaki D, Nishikawa Y, Ono A, Yamaguchi M, Ogasawara K (2011) High‐resolution diffusion tensor imaging for the detection of diffusion abnormalities in the trigeminal nerves of patients with trigeminal neuralgia caused by neurovascular compression. J Neuroimaging 21:e102-e108.

George JA, Brinton MR, Duncan CC, Hutchinson DT, Clark GA (2018) Improved training paradigms and motor-decode algorithms: results from intact individuals and a recent transradial amputee with prior complex regional pain syndrome. In: 2018 40th annual international conference of the IEEE Engineering in Medicine and Biology Society (EMBC), pp 3782-3787: IEEE.

Georgopoulos A, Caminiti R, Kalaska J (1984) Static spatial effects in motor cortex and area 5: quantitative relations in a two-dimensional space. Experimental Brain Research 54:446-454.
Gilja V, Nuyujukian P, Chestek CA, Cunningham JP, Byron MY, Fan JM, Churchland MM, Kaufman MT, Kao JC, Ryu SI (2012) A high-performance neural prosthesis enabled by control algorithm design. Nature neuroscience 15:1752.
Grill WM (2018) Temporal Pattern of Electrical Stimulation is a New Dimension of Therapeutic Innovation. Current Opinion in Biomedical Engineering.
Grill WM, Simmons AM, Cooper SE, Miocinovic S, Montgomery EB, Baker KB, Rezai AR (2005) Temporal excitation properties of paresthesias evoked by thalamic microstimulation. Clinical neurophysiology : official journal of the International Federation of Clinical Neurophysiology 116:1227-1234.
Gross RE, Boulis NM (2018) Neurosurgical Operative Atlas: Functional Neurosurgery: Thieme.
Halassa MM, Kastner S (2017) Thalamic functions in distributed cognitive control. Nature neuroscience 20:1669-1679.
Hanakita J, Kondo A (1988) Serious complications of microvascular decompression operations for trigeminal neuralgia and hemifacial spasm. Neurosurgery 22:248-352.
Hardaway FA, Gustafsson HC, Holste K, Burchiel KJ, Raslan AM (2019) A novel scoring system as a preoperative predictor for pain-free survival after microsurgery for trigeminal neuralgia. Journal of neurosurgery 1:1-8.
Hastie T, Tibshirani R, Friedman J (2009) The elements of statistical learning: data mining, inference, and prediction: Springer Science & Business Media.
He K, Zhang X, Ren S, Sun J (2015) Delving deep into rectifiers: Surpassing human-level performance on imagenet classification. In: Proceedings of the IEEE international conference on computer vision, pp 1026-1034.
Heming E, Sanden A, Kiss ZH (2010) Designing a somatosensory neural prosthesis: percepts evoked by different patterns of thalamic stimulation. J Neural Eng 7:064001.
Heming EA, Choo R, Davies JN, Kiss ZH (2011) Designing a thalamic somatosensory neural prosthesis: Consistency and persistence of percepts evoked by electrical stimulation. IEEE Transactions on Neural Systems and Rehabilitation Engineering 19:477-482.
Herweh C, Kress B, Rasche D, Tronnier V, Tröger J, Sartor K, Stippich C (2007) Loss of anisotropy in trigeminal neuralgia revealed by diffusion tensor imaging. Neurology 68:776-778.
Hilton DA, Love S, Gradidge T, Coakham HB (1994) Pathological findings associated with trigeminal neuralgia caused by vascular compression. Neurosurgery 35:299-303.
Hochberg LR, Bacher D, Jarosiewicz B, Masse NY, Simeral JD, Vogel J, Haddadin S, Liu J, Cash SS, Van Der Smagt P (2012) Reach and grasp by people with tetraplegia using a neurally controlled robotic arm. Nature 485:372-375.
Hoffer ZS, Arantes HB, Roth RL, Alloway KD (2005) Functional circuits mediating sensorimotor integration: quantitative comparisons of projections from rodent barrel cortex to primary motor cortex, neostriatum, superior colliculus, and the pons. Journal of Comparative Neurology 488:82-100.
Holste K, Chan AY, Rolston JD, Englot DJ (2020) Pain outcomes following microvascular decompression for drug-resistant trigeminal neuralgia: a systematic review and meta-analysis. Neurosurgery 86:182-190.

Homayoun H, Moghaddam B (2007) NMDA receptor hypofunction produces opposite effects on prefrontal cortex interneurons and pyramidal neurons. Journal of Neuroscience 27:11496-11500.
Horsfield MA, Jones DK (2002) Applications of diffusion‐weighted and diffusion tensor MRI to white matter diseases–a review. NMR in Biomedicine: An International Journal Devoted to the Development and Application of Magnetic Resonance In Vivo 15:570-577.
Hosman T, Vilela M, Milstein D, Kelemen JN, Brandman DM, Hochberg LR, Simeral JD (2019) BCI decoder performance comparison of an LSTM recurrent neural network and a Kalman filter in retrospective simulation. In: 2019 9th International IEEE/EMBS Conference on Neural Engineering (NER), pp 1066-1071: IEEE.
Huang Z, Liu X, Mashour GA, Hudetz AG (2018) Timescales of Intrinsic BOLD Signal Dynamics and Functional Connectivity in Pharmacologic and Neuropathologic States of Unconsciousness. The Journal of neuroscience : the official journal of the Society for Neuroscience 38:2304-2317.
Hudetz AG (2012) General anesthesia and human brain connectivity. Brain connectivity 2:291-302.
Hung PS-P, Chen DQ, Davis KD, Zhong J, Hodaie M (2017) Predicting pain relief: use of pre-surgical trigeminal nerve diffusion metrics in trigeminal neuralgia. NeuroImage: Clinical 15:710-718.
Icaza EE, Mashour GA (2013) Altered states: psychedelics and anesthetics. Anesthesiology 119:1255-1260.
Iremonger KJ, Anderson TR, Hu B, Kiss ZH (2006) Cellular mechanisms preventing sustained activation of cortex during subcortical high-frequency stimulation. Journal of neurophysiology 96:613-621.
Irwin Z, Schroeder K, Vu P, Bullard A, Tat D, Nu C, Vaskov A, Nason S, Thompson D, Bentley J (2017) Neural control of finger movement via intracortical brain–machine interface. Journal of neural engineering 14:066004.
Ishizawa Y, Ahmed OJ, Patel SR, Gale JT, Sierra-Mercado D, Brown EN, Eskandar EN (2016) Dynamics of propofol-induced loss of consciousness across primate neocortex. Journal of Neuroscience 36:7718-7726.
Jevtovic-Todorovic V, Todorovic SM, Mennerick S, Powell S, Dikranian K, Benshoff N, Zorumski CF, Olney JW (1998) Nitrous oxide (laughing gas) is an NMDA antagonist, neuroprotectant and neurotoxin. Nat Med 4:460-463.
Jin MC, Medress ZA, Azad TD, Doulames VM, Veeravagu A (2019) Stem cell therapies for acute spinal cord injury in humans: A review. Neurosurgical focus 46:E10.
Johnson L, Wander J, Sarma D, Su D, Fetz E, Ojemann J (2013) Direct electrical stimulation of the somatosensory cortex in humans using electrocorticography electrodes: a qualitative and quantitative report. Journal of neural engineering 10:036021.
Jones EG, Peters A (2012) Cerebral cortex: comparative structure and evolution of cerebral cortex: Springer Science & Business Media.
Kalman RE (1960) A new approach to linear filtering and prediction problems.
Kalman RE, Bucy RS (1961) New results in linear filtering and prediction theory.
Kao JC, Nuyujukian P, Ryu SI, Shenoy KV (2016) A high-performance neural prosthesis incorporating discrete state selection with hidden Markov models. IEEE Transactions on Biomedical Engineering 64:935-945.

Kawamoto T, Shingu K, Mori K (1990) Effects of nitrous oxide on the somatosensory evoked response in cats. Journal of anesthesia 4:51-60.
Kim S-P, Simeral JD, Hochberg LR, Donoghue JP, Black MJ (2008) Neural control of computer cursor velocity by decoding motor cortical spiking activity in humans with tetraplegia. Journal of neural engineering 5:455.
Kingma DP, Ba J (2014) Adam: A method for stochastic optimization. arXiv preprint arXiv:14126980.
Kiss ZH, Anderson T, Hansen T, Kirstein D, Suchowersky O, Hu B (2003) Neural substrates of microstimulation-evoked tingling: a chronaxie study in human somatosensory thalamus. The European journal of neuroscience 18:728-732.
Krizhevsky A, Sutskever I, Hinton GE (2012) Imagenet classification with deep convolutional neural networks. In: Advances in neural information processing systems, pp 1097-1105.
Leal PR, Roch JA, Hermier M, Souza MA, Cristino-Filho G, Sindou M (2011) Structural abnormalities of the trigeminal root revealed by diffusion tensor imaging in patients with trigeminal neuralgia caused by neurovascular compression: a prospective, double-blind, controlled study. Pain 152:2357-2364.
Leal PRL, Roch J, Hermier M, Berthezene Y, Sindou M (2019) Diffusion tensor imaging abnormalities of the trigeminal nerve root in patients with classical trigeminal neuralgia: a pre- and postoperative comparative study 4 years after microvascular decompression. Acta Neurochir (Wien) 161:1415-1425.
Lebedev MA, Nicolelis MA (2017) Brain-Machine Interfaces: From Basic Science to Neuroprostheses and Neurorehabilitation. Physiological reviews 97:767-837.
Lee J-I, Ohara S, Dougherty PM, Lenz FA (2005) Pain and temperature encoding in the human thalamic somatic sensory nucleus (ventral caudal): inhibition-related bursting evoked by somatic stimuli. Journal of neurophysiology 94:1676-1687.
Lee U, Mashour GA (2018) Role of Network Science in the Study of Anesthetic State Transitions. Anesthesiology.
Lee U, Ku S, Noh G, Baek S, Choi B, Mashour GA (2013) Disruption of frontal-parietal communication by ketamine, propofol, and sevoflurane. Anesthesiology 118:1264-1275.
Lenz F, Gracely R, Rowland L, Dougherty P, Lee J (2000) Sensations evoked by stimulation with bursts of different numbers of stimuli and frequencies in the region of the human thalamic principal somatosensory nucleus. In: Soc Neurosci Abstr, p 2105.
Lenz FA, Dostrovsky JO, Tasker RR, Yamashiro K, Kwan HC, Murphy JT (1988) Single-unit analysis of the human ventral thalamic nuclear group: somatosensory responses. J Neurophysiol 59:299-316.
Lenz FA, Kwan HC, Martin RL, Tasker RR, Dostrovsky JO, Lenz YE (1994a) Single unit analysis of the human ventral thalamic nuclear group. Tremor-related activity in functionally identified cells. Brain 117 (Pt 3):531-543.
Lenz FA, Kwan HC, Martin R, Tasker R, Richardson RT, Dostrovsky JO (1994b) Characteristics of somatotopic organization and spontaneous neuronal activity in the region of the thalamic principal sensory nucleus in patients with spinal cord transection. J Neurophysiol 72:1570-1587.
Lenz FA, Seike M, Richardson RT, Lin YC, Baker FH, Khoja I, Jaeger CJ, Gracely RH (1993) Thermal and pain sensations evoked by microstimulation in the area of human ventrocaudal nucleus. J Neurophysiol 70:200-212.

Lewis LD, Weiner VS, Mukamel EA, Donoghue JA, Eskandar EN, Madsen JR, Anderson WS, Hochberg LR, Cash SS, Brown EN (2012) Rapid fragmentation of neuronal networks at the onset of propofol-induced unconsciousness. Proceedings of the National Academy of Sciences 109:E3377-E3386.
Lin W, Zhu WP, Chen YL, Han GC, Rong Y, Zhou YR, Zhang QW (2016) Large-diameter compression arteries as a possible facilitating factor for trigeminal neuralgia: analysis of axial and radial diffusivity. Acta Neurochir (Wien) 158:521-526.
Liu Y, Li J, Butzkueven H, Duan Y, Zhang M, Shu N, Li Y, Zhang Y, Li K (2013) Microstructural abnormalities in the trigeminal nerves of patients with trigeminal neuralgia revealed by multiple diffusion metrics. European journal of radiology 82:783-786.
Louis ED, Ferreira JJ (2010) How common is the most common adult movement disorder? Update on the worldwide prevalence of essential tremor. Movement Disorders 25:534-541.
Love S, Coakham HB (2001) Trigeminal neuralgia: pathology and pathogenesis. Brain 124:2347-2360.
Luczak A, McNaughton BL, Harris KD (2015) Packet-based communication in the cortex. Nature Reviews Neuroscience 16:745.
Lummel N, Mehrkens J, Linn J, Buchholz G, Stahl R, Bochmann K, Brückmann H, Lutz J (2014) Diffusion tensor imaging of the trigeminal nerve in patients with trigeminal neuralgia due to multiple sclerosis. Neuroradiology:1-9.
Lutz J, Thon N, Stahl R, Lummel N, Tonn JC, Linn J, Mehrkens JH (2016) Microstructural alterations in trigeminal neuralgia determined by diffusion tensor imaging are independent of symptom duration, severity, and type of neurovascular conflict. J Neurosurg 124:823-830.
Lutz J, Linn J, Mehrkens JH, Thon N, Stahl R, Seelos K, Bruckmann H, Holtmannspotter M (2011) Trigeminal neuralgia due to neurovascular compression: high-spatial-resolution diffusion-tensor imaging reveals microstructural neural changes. Radiology 258:524-530.
Ma VY, Chan L, Carruthers KJ (2014) Incidence, prevalence, costs, and impact on disability of common conditions requiring rehabilitation in the United States: stroke, spinal cord injury, traumatic brain injury, multiple sclerosis, osteoarthritis, rheumatoid arthritis, limb loss, and back pain. Archives of physical medicine and rehabilitation 95:986-995. e981.
Maarbjerg S, Gozalov A, Olesen J, Bendtsen L (2014) Concomitant persistent pain in classical trigeminal neuralgia–evidence for different subtypes. Headache: The Journal of Head and Face Pain 54:1173-1183.
Mao T, Kusefoglu D, Hooks BM, Huber D, Petreanu L, Svoboda K (2011) Long-range neuronal circuits underlying the interaction between sensory and motor cortex. Neuron 72:111-123.
Marmor O, Valsky D, Joshua M, Bick AS, Arkadir D, Tamir I, Bergman H, Israel Z, Eitan R (2017) Local vs. volume conductance activity of field potentials in the human subthalamic nucleus. Journal of neurophysiology 117:2140-2151.
McIntyre CC, Grill WM (1999) Excitation of central nervous system neurons by nonuniform electric fields. Biophysical journal 76:878-888.
McIntyre CC, Grill WM (2000) Selective microstimulation of central nervous system neurons. Annals of biomedical engineering 28:219-233.

McIntyre CC, Grill WM (2002) Extracellular stimulation of central neurons: influence of stimulus waveform and frequency on neuronal output. Journal of neurophysiology 88:1592-1604.
Miocinovic S, Grill WM (2004) Sensitivity of temporal excitation properties to the neuronal element activated by extracellular stimulation. Journal of neuroscience methods 132:91-99.
Mo C, Sherman SM (2019) A sensorimotor pathway via higher-order thalamus. Journal of Neuroscience 39:692-704.
Montgomery JE, Baker KB (2000) Mechanisms of deep brain stimulation and future technical developments. Neurological research 22:259-266.
Montgomery Jr EB (2005) Effect of subthalamic nucleus stimulation patterns on motor performance in Parkinson's disease. Parkinsonism & related disorders 11:167-171.
Moran DW, Schwartz AB (1999) Motor cortical representation of speed and direction during reaching. Journal of neurophysiology 82:2676-2692.
Mori K, Kawamata M, Mitani H, Yamazaki Y, Fujita M (1971) A neurophysiologic study of ketamine anesthesia in the cat. Anesthesiology 35:373-382.
Moritz CT, Perlmutter SI, Fetz EE (2008) Direct control of paralysed muscles by cortical neurons. Nature 456:639-642.
Mountcastle VB, Henneman E (1952) The representation of tactile sensibility in the thalamus of the monkey. Journal of Comparative Neurology 97:409-439.
Nason SR, Vaskov AK, Mender M, Willsey MS, Patil PG, Chestek CA (2019) Optimizing Decoding Performance and Power Consumption for Fine Two Finger Control in Closed Loop Implantable Brain Machine Interfaces. In: SNF. Chicago.
Nason SR, Vaskov AK, Willsey MS, Welle EJ, H. A, Vu PP, Bullard AJ, Nu CS, Jang T, Blaauw D, Patil PG, Chestek CA (in press) Low-power 'spiking band' feature has sensitivity and specificity toward single units and improves motor decode performance. Nature Biomedical Engineering.
Neetu S, Sunil K, Ashish A, Jayantee K, Usha Kant M (2016) Microstructural abnormalities of the trigeminal nerve by diffusion-tensor imaging in trigeminal neuralgia without neurovascular compression. Neuroradiol J 29:13-18.
Nordhausen CT, Maynard EM, Normann RA (1996) Single unit recording capabilities of a 100 microelectrode array. Brain research 726:129-140.
Ohara S, Weiss N, Lenz FA (2004) Microstimulation in the region of the human thalamic principal somatic sensory nucleus evokes sensations like those of mechanical stimulation and movement. J Neurophysiol 91:736-745.
Pal D, Hambrecht-Wiedbusch VS, Silverstein BH, Mashour GA (2015) Electroencephalographic coherence and cortical acetylcholine during ketamine-induced unconsciousness. BJA: British Journal of Anaesthesia 114:979-989.
Pandarinath C, O'Shea DJ, Collins J, Jozefowicz R, Stavisky SD, Kao JC, Trautmann EM, Kaufman MT, Ryu SI, Hochberg LR (2018) Inferring single-trial neural population dynamics using sequential auto-encoders. Nature methods 15:805-815.
Parkhouse J, Henrie JR, Duncan GM, Rome HP (1960) Nitrous oxide analgesia in relation to mental performance. The Journal of pharmacology and experimental therapeutics.
Patel IM, Chapin JK (1990) Ketamine effects on somatosensory cortical single neurons and on behavior in rats. Anesthesia and analgesia 70:635-644.

Patil PG, Dodani S (2018) Advanced intraoperative neural targeting system and method. In: Google Patents.
Pavlides C, Miyashita E, Asanuma H (1993) Projection from the sensory to the motor cortex is important in learning motor skills in the monkey. Journal of neurophysiology 70:733-741.
Peker S, Kurtkaya Ö, Üzün I, Pamir MN (2006) Microanatomy of the central myelin-peripheral myelin transition zone of the trigeminal nerve. Neurosurgery 59:354-359.
Pelentritou A, Kuhlmann L, Cormack J, Mcguigan S, Woods W, Muthukumaraswamy S, Liley D (2019) In search of Universal Cortical Power Changes Linked to NMDA-Antagonist based Anesthetic Induced Reductions in Consciousness. bioRxiv:572636.
Penfield W (1960) A surgeon's chance encounters with mechanisms related to consciousness. Journal of the Royal College of Surgeons of Edinburgh 5:173-190.
Petrof I, Viaene AN, Sherman SM (2015) Properties of the primary somatosensory cortex projection to the primary motor cortex in the mouse. Journal of neurophysiology 113:2400-2407.
Plonsey R, Barr RC (2007) Bioelectricity: a quantitative approach: Springer Science & Business Media.
Pollo C, Kaelin-Lang A, Oertel MF, Stieglitz L, Taub E, Fuhr P, Lozano AM, Raabe A, Schüpbach M (2014) Directional deep brain stimulation: an intraoperative double-blind pilot study. Brain 137:2015-2026.
Qazi AA, Radmanesh A, O'donnell L, Kindlmann G, Peled S, Whalen S, Westin C-F, Golby AJ (2009) Resolving crossings in the corticospinal tract by two-tensor streamline tractography: method and clinical assessment using fMRI. Neuroimage 47:T98-T106.
Rampil IJ, Kim JS, Lenhardt R, Negishi C, Sessler DI (1998) Bispectral EEG index during nitrous oxide administration. Anesthesiology 89:671-677.
Ray S, Crone NE, Niebur E, Franaszczuk PJ, Hsiao SS (2008) Neural correlates of high-gamma oscillations (60–200 Hz) in macaque local field potentials and their potential implications in electrocorticography. Journal of Neuroscience 28:11526-11536.
Schaltenbrand G, Wahren W (1977) Atlas for Stereotaxy of the Human Brain: Thieme.
Schmid A-C, Chien J-H, Greenspan JD, Garonzik I, Weiss N, Ohara S, Lenz FA (2016) Neuronal responses to tactile stimuli and tactile sensations evoked by microstimulation in the human thalamic principal somatic sensory nucleus (ventral caudal). Journal of neurophysiology 115:2421-2433.
Schroeder KE, Irwin ZT, Gaidica M, Nicole Bentley J, Patil PG, Mashour GA, Chestek CA (2016) Disruption of corticocortical information transfer during ketamine anesthesia in the primate brain. Neuroimage 134:459-465.
Schroter MS, Spoormaker VI, Schorer A, Wohlschlager A, Czisch M, Kochs EF, Zimmer C, Hemmer B, Schneider G, Jordan D, Ilg R (2012) Spatiotemporal reconfiguration of large-scale brain functional networks during propofol-induced loss of consciousness. The Journal of neuroscience : the official journal of the Society for Neuroscience 32:12832-12840.
Schrouff J, Perlbarg V, Boly M, Marrelec G, Boveroux P, Vanhaudenhuyse A, Bruno M-A, Laureys S, Phillips C, Pélégrini-Issac M (2011) Brain functional integration decreases during propofol-induced loss of consciousness. NeuroImage 57:198-205.
Schwartz AB, Cui XT, Weber DJ, Moran DW (2006) Brain-controlled interfaces: movement restoration with neural prosthetics. Neuron 52:205-220.

Schwemmer MA, Skomrock ND, Sederberg PB, Ting JE, Sharma G, Bockbrader MA, Friedenberg DA (2018) Meeting brain–computer interface user performance expectations using a deep neural network decoding framework. Nature medicine 24:1669-1676.
Serruya MD, Hatsopoulos NG, Paninski L, Fellows MR, Donoghue JP (2002) Instant neural control of a movement signal. Nature 416:141-142.
Shanechi MM, Williams ZM, Wornell GW, Hu RC, Powers M, Brown EN (2013) A real-time brain-machine interface combining motor target and trajectory intent using an optimal feedback control design. PloS one 8.
Shichino T, Murakawa M, Adachi T, Arai T, Miyazaki Y, Mori K (1998) Effects of inhalation anaesthetics on the release of acetylcholine in the rat cerebral cortex in vivo. British journal of anaesthesia 80:365-370.
Song S-K, Sun S-W, Ramsbottom MJ, Chang C, Russell J, Cross AH (2002) Dysmyelination revealed through MRI as increased radial (but unchanged axial) diffusion of water. Neuroimage 17:1429-1436.
Srivastava N, Hinton G, Krizhevsky A, Sutskever I, Salakhutdinov R (2014) Dropout: a simple way to prevent neural networks from overfitting. The journal of machine learning research 15:1929-1958.
Starr PA, Barbaro NM, Larson PS (2009) Neurosurgical operative atlas: functional neurosurgery: Thieme.
Stevens J, Oshima E, Mori K (1983) Effects of nitrous oxide on the epileptogenic property of enflurane in cats. BJA: British Journal of Anaesthesia 55:145-154.
Sussillo D, Nuyujukian P, Fan JM, Kao JC, Stavisky SD, Ryu S, Shenoy K (2012) A recurrent neural network for closed-loop intracortical brain–machine interface decoders. Journal of neural engineering 9:026027.
Swan BD, Gasperson LB, Krucoff MO, Grill WM, Turner DA (2017) Sensory percepts induced by microwire array and DBS microstimulation in human sensory thalamus. Brain Stimulation.
Swan BD, Brocker DT, Hilliard JD, Tatter SB, Gross RE, Turner DA, Grill WM (2016) Short pauses in thalamic deep brain stimulation promote tremor and neuronal bursting. Clinical Neurophysiology 127:1551-1559.
Swerling P (1959) First-order error propagation in a stagewise smoothing procedure for satellite observations.
Szostak KM, Grand L, Constandinou TG (2017) Neural interfaces for intracortical recording: Requirements, fabrication methods, and characteristics. Frontiers in Neuroscience 11:665.
Tadler SC, Mickey BJ (2018) Emerging evidence for antidepressant actions of anesthetic agents. Current Opinion in Anesthesiology 31:439-445.
Takeshita H, Okuda Y, Sari A (1972) The effects of ketamine on cerebral circulation and metabolism in man. Anesthesiology 36:69-75.
Tan D, Tyler D, Sweet J, Miller J (2016) Intensity modulation: a novel approach to percept control in spinal cord stimulation. Neuromodulation: Technology at the Neural Interface 19:254-259.
Tan DW, Schiefer MA, Keith MW, Anderson JR, Tyler J, Tyler DJ (2014) A neural interface provides long-term stable natural touch perception. Sci Transl Med 6:257ra138.
Tasker RR, Organ LW, Hawrylyshyn PA (1982) The thalamus and midbrain of man: a physiological atlas using electrical stimulation: Charles C. Thomas Publisher.

Tasker RR, Richardson P, Rewcastle B, Emmers R (1972) Anatomical correlation of detailed sensory mapping of the human thalamus. Confin Neurol 34:184-196.
Tate DG, Kalpakjian CZ, Forchheimer MB (2002) Quality of life issues in individuals with spinal cord injury. Archives of Physical Medicine and Rehabilitation 83:S18-S25.
Taylor DM, Tillery SIH, Schwartz AB (2002) Direct cortical control of 3D neuroprosthetic devices. Science 296:1829-1832.
Thomson AM, West DC, Lodge D (1985) An N-methylaspartate receptor-mediated synapse in rat cerebral cortex: a site of action of ketamine? Nature 313:479-481.
Tohyama S, Hung PS, Zhong J, Hodaie M (2018) Early postsurgical diffusivity metrics for prognostication of long-term pain relief after Gamma Knife radiosurgery for trigeminal neuralgia. J Neurosurg 131:539-548.
Tyler-Kabara EC, Kassam AB, Horowitz MH, Urgo L, Hadjipanayis C, Levy EI, Chang Y-F (2002) Predictors of outcome in surgically managed patients with typical and atypical trigeminal neuralgia: comparison of results following microvascular decompression. Journal of neurosurgery 96:527-531.
Unal TC, Unal OF, Barlas O, Hepgul K, Ali A, Aydoseli A, Aras Y, Sabanci PA, Sencer A, Izgi N (2017) Factors determining the outcome in trigeminal neuralgia treated with percutaneous balloon compression. World Neurosurg 107:69-74.
Vaskov AK, Irwin ZT, Nason SR, Vu PP, Nu CS, Bullard AJ, Hill M, North N, Patil PG, Chestek CA (2018) Cortical decoding of individual finger group motions using refit kalman filter. Frontiers in neuroscience 12:751.
Vu PP, Vaskov AK, Irwin ZT, Henning PT, Lueders DR, Laidlaw AT, Davis AJ, Nu CS, Gates DH, Gillespie RB (2020) A regenerative peripheral nerve interface allows real-time control of an artificial hand in upper limb amputees. Science Translational Medicine 12.
Wang DD, Raygor KP, Cage TA, Ward MM, Westcott S, Barbaro NM, Chang EF (2017) Prospective comparison of long-term pain relief rates after first-time microvascular decompression and stereotactic radiosurgery for trigeminal neuralgia. J Neurosurg 128:68-77.
Wang M, Yang Y, Wang C-J, Gamo NJ, Jin LE, Mazer JA, Morrison JH, Wang X-J, Arnsten AF (2013) NMDA receptors subserve persistent neuronal firing during working memory in dorsolateral prefrontal cortex. Neuron 77:736-749.
Wendelken S, Page DM, Davis T, Wark HA, Kluger DT, Duncan C, Warren DJ, Hutchinson DT, Clark GA (2017) Restoration of motor control and proprioceptive and cutaneous sensation in humans with prior upper-limb amputation via multiple Utah Slanted Electrode Arrays (USEAs) implanted in residual peripheral arm nerves. Journal of neuroengineering and rehabilitation 14:121.
Wenzel M, Han S, Smith EH, Hoel E, Greger B, House PA, Yuste R (2019) Reduced Repertoire of Cortical Microstates and Neuronal Ensembles in Medically Induced Loss of Consciousness. Cell systems 8:467-474. e464.
Wessberg J, Stambaugh CR, Kralik JD, Beck PD, Laubach M, Chapin JK, Kim J, Biggs SJ, Srinivasan MA, Nicolelis MA (2000) Real-time prediction of hand trajectory by ensembles of cortical neurons in primates. Nature 408:361-365.
Willsey MS, Collins KL, Conrad EC, Chubb HA, Patil PG (2019) Diffusion tensor imaging reveals microstructural differences between subtypes of trigeminal neuralgia. J Neurosurg:1-7. doi: 10.3171/2019.3174.JNS19299.

Wu W, Black MJ, Mumford D, Gao Y, Bienenstock E, Donoghue JP (2004) Modeling and decoding motor cortical activity using a switching Kalman filter. IEEE transactions on biomedical engineering 51:933-942.
Yamamura T, Fukuda M, Takeya H, Goto Y, Furukawa K (1981) Fast oscillatory EEG activity induced by analgesic concentrations of nitrous oxide in man. Anesthesia and analgesia 60:283-288.
Yi G, Grill WM (2018) Frequency-dependent antidromic activation in thalamocortical relay neurons: effects of synaptic inputs. Journal of neural engineering 15:056001.
Zhang Y, Mao Z, Cui Z, Ling Z, Pan L, Liu X, Zhang J, Yu X (2018) Diffusion tensor imaging of axonal and myelin changes in classical trigeminal neuralgia. World Neurosurg 112:e597-e607.